

ABSTRACT

Electric Vehicle Powertrain Design with Battery Swapping and Vehicle to Grid Implementation.

Feyijimi Adegbohun, Ph.D

Co-chairperson: Annette Von Jouanne, Ph.D

Co-chairperson: Kwang Y. Lee, Ph.D

Described in this work are methodologies for the design and development of electric vehicle (EV) powertrains through modeling, simulation and validation on a real-world systems, with detailed analysis of results. A system for swapping, storing and managing EV batteries, including a Deep Neural Network (DNN) based state of health estimation model is developed and analyzed. The system is designed to enable advanced interface with the electric grid and address challenges in the adoption of EVs which include : Cost, range anxiety, charging time and charging infrastructure, battery state of health, and impacts of vehicle to grid (V2G) operations. The EV battery swapping system (BSS) consists of the EV powertrain equipped with swapping capability, modular swappable battery packs, battery storage apparatus, bidirectional charging system, battery and charge management system, and battery swapping equipment. This system provides a cost-effective way of adopting electrification, reducing strain on the electricity grid during peak periods and extending the life of EV batteries.

Electric Vehicle Powertrain Design with Battery Swapping and Vehicle to Grid
Implementation

by

Feyijimi R. Adegbohun, B.S., M.S.E.C.E.

A Dissertation

Approved by the Department of Electrical and Computer Engineering

Kwang Y. Lee, Ph.D., Chairperson

Submitted to the Graduate Faculty of
Baylor University in Partial Fulfillment of the
Requirements for the Degree
of
Doctor of Philosophy

Approved by the Dissertation Committee

Annette von Jouanne, Ph.D., Co-Chairperson

Kwang Y. Lee, Ph.D., Co-Chairperson

Emmanuel Agamloh, Ph.D.

Alex Yokochi, Ph.D.

Accepted by the Graduate School
May 2021

J. Larry Lyon, Ph.D., Dean

Copyright © 2021 by Feyijimi Adegbohun

All rights reserved

TABLE OF CONTENTS

LIST OF FIGURES	vi
LIST OF TABLES	xi
ACKNOWLEDGMENTS	xii
DEDICATION	xiii
CHAPTER ONE	1
<i>Background and Literature Review</i>	<i>1</i>
1.1. Motivation.....	1
1.2. Background.....	6
1.3. Research Contributions.....	12
CHAPTER TWO	13
<i>Electric Vehicle Powertrain Design</i>	<i>13</i>
2.1. Introduction.....	13
2.2. Dynamics of Vehicle Motion.....	19
2.3. Electric Vehicle Powertrain Sizing.....	22
2.4. Electric Vehicle Modeling and Simulation.....	29
2.5. Electric Vehicle Chassis Dynamometer Testing.....	43
2.6. Electric Vehicle Model Simulation Results and Analysis	47
2.7. Battery Swappable Electric Vehicle Powertrain Prototype Design.....	56
CHAPTER THREE	69
<i>Battery Management System and Health Estimation</i>	<i>69</i>
3.1. Introduction.....	69
3.2. Background.....	70
3.3. Lithium-Ion Battery Chemistry.....	71
3.3.1. Lithium-Ion Battery Aging	73
3.3.2. Lithium-ion Cell Aging - Qualitative analysis.....	74
3.3.3. Lithium Ion Negative Electrode Aging.....	74
3.3.4. Lithium Ion Positive Electrode Aging.....	77
3.4. Equivalent Circuit Model and Parameter Estimation	79
3.5. Battery Management System	86
3.6. Battery State of Health Estimation	94
CHAPTER FOUR.....	110
<i>Modular Connected Battery Pack, Battery Swapping Station and Vehicle to Grid</i>	<i>110</i>
4.1. Battery Cooling Systems.....	113

4.2. Onboard Bidirectional Charger.....	116
4.3. Swappable Electric Vehicle Chassis.....	118
4.4. Battery Swapping Network and V2G System	119
4.5. Electrical Design of BSS and V2G Implementation.....	121
4.6. Battery Sharing Network Charge Management System	124
CHAPTER FIVE	126
<i>Conclusion and Future Work</i>	126
APPENDIX A.....	131
<i>A Deep Neural Network Model in Jupyter Notebook</i>	131
BIBLIOGRAPHY	148

LIST OF FIGURES

Figure 2.1. Chevrolet Bolt, Single Speed Direct Drive Unit	14
Figure 2.2. Tesla Model S Dual Motor, AWD Drive Unit	15
Figure 2.3. Porsche Taycan Rear Drive Unit with Two-speed Transmission	15
Figure 2.4. Ragone plot of battery chemistries	17
Figure 2.5. EV architectural diagram.....	18
Figure 2.6. Free body diagram of forces acting on an EV	20
Figure 2.7. Speed and forces in the tire-road contact patch area	21
Figure 2.8. Torque speed envelope of an electric motor.....	23
Figure 2.9. Porsche Taycan Powertrain Architecture.....	25
Figure 2.10. Porsche Taycan AWD dual motor, two-speed shifting strategy	26
Figure 2.11. BorgWarner 250 hp electric motor torque-speed envelope.....	27
Figure 2.12. BorgWarner 250 hp electric motor torque-speed envelope.....	27
Figure 2.13. MCT Drive Cycle	33
Figure 2.14. Simulink Equation Based EV Model [54].....	34
Figure 2.15. Vehicle Body Glider Model	35
Figure 2.16. Vehicle Glider Model Subsystem	36
Figure 2.17. Energy and Power Analysis of Glider Model Subsystem	36
Figure 2.18. Driver Control System Block.....	37
Figure 2.19. Braking System Block.....	38
Figure 2.20. Motor loss model.....	38

Figure 2.21. Electric Motor Model with motor loss model calculations	39
Figure 2.22. Battery Model with Internal Resistance	41
Figure 2.23. Battery Model with SOC and Power Loss Calculations	41
Figure 2.24. Driveline loss model and calculations	42
Figure 2.25. Road and dynamometer test vehicle speed and difference.....	44
Figure 2.26. Road and dyno test vehicle power (left axis) and energy (right axis)	45
Figure 2.27. MCT drive cycle vehicle speed on chassis dyno.....	45
Figure 2.28. MCT drive cycle vehicle power(left axis) and energy (right axis) on chassis dyno	46
Figure 2.29. WOT Test (a) Motor torque envelope (b) Vehicle speed.....	46
Figure 2.30. Modeled vehicle speed over time compared to dyno speed	48
Figure 2.31. Modeled battery State of Charge (SOC) over time	49
Figure 2.32. Battery energy over time	50
Figure 2.33. Vehicle distance covered over time.....	50
Figure 2.34. Motor power over speed.....	52
Figure 2.35. Motor torque over speed (a) Simulation (b) Dyno Test	53
Figure 2.36. Motor torque over time plot	53
Figure 2.37. Vehicle tractive energy over time.....	54
Figure 2.38. Motor energy losses over time	55
Figure 2.39. Driveline energy losses over time.	55
Figure 2.40. Battery Swappable Electric Vehicle Powertrain Chassis Prototype.....	57
Figure 2.41. MATLAB/Simulink Model of Electric Vehicle Dynamics.....	58
Figure 2.42. Isometric and Top view of vehicle powertrain mechanical design	60
Figure 2.43. Cross section of vehicle powertrain mechanical design.....	61

Figure 2.44. Electric drivetrain tripod mount locations	61
Figure 2.45. Battery Pack Assembly.....	63
Figure 2.46. Battery Pack Collection Frame Detail	64
Figure 2.47. Battery Pack Collection Frame Top View.....	64
Figure 2.48. Battery Pack Latch Assembly	65
Figure 2.49. UQM motor system block diagram	67
Figure 2.50. Thunderstruck motors VCU system block diagram	67
Figure 2.51. E-Tahoe thermal management system design	68
Figure 3.1. Lithium-Ion cell cross section with LiCoO_2 Cathode and Li_2C Anode	72
Figure 3.2. SEI layer formulation between anode and electrolyte material.....	76
Figure 3.3. Li-cobalt oxide structure.....	78
Figure 3.4. Equivalent Circuit Model of a Li-ion Battery	79
Figure 3.5. Illustration of equivalent circuit elements representation of cell voltage	80
Figure 3.6. MATLAB parameter estimation simulated results compared to experimental data	82
Figure 3.7. MATLAB/Simscape cell model with thermal port	84
Figure 3.8. MATLAB/Simscape cell model parameters	84
Figure 3.9. Model of lithium ion cell with thermal insulation and measurements	85
Figure 3.10. Measurements of Voltage, Current, SOC and Temperature.....	85
Figure 3.11. Battery Module with 6 cell strings and measurement sensors	87
Figure 3.12. Battery passive balancing circuit.....	88
Figure 3.13. Battery precharge protection circuit	89
Figure 3.14. Battery Management System.....	91

Figure 3.15. Battery voltages and currents for driving and charging cycles	92
Figure 3.16. Battery cell temperatures and BMS states for driving and charging cycles.....	93
Figure 3.17. BMS Balance command	94
Figure 3.18. Tesla Model S/X Battery Capacity Retention over distance traveled	95
Figure 3.19. Battery Charging in CCCV	96
Figure 3.20. A123 Cell voltage over charge and discharge cycles.....	98
Figure 3.21. A123 Cell Current over charge and discharge cycles	98
Figure 3.22. A123 Cell Charge capacity over charge cycles.....	99
Figure 3.23. A123 Cell Charge capacity over charge cycle indices	100
Figure 3.24. A123 Cell Current over charge cycle in CV region	100
Figure 3.25. A123 Cell Voltage over charge cycle in CV region.....	101
Figure 3.26. A123 Cell Current gradients in CV region over charge cycle indices	101
Figure 3.27. A123 Cell Charge time for CV region over charge cycle indices.....	102
Figure 3.28. A123 Cell CV charge current gradient against capacity	102
Figure 3.29. Panasonic NCM cell battery spec sheet.....	103
Figure 3.30. CAD 3D Model of flooded cell enclosure.....	104
Figure 3.31. Battery aging cyler experimental setup	104
Figure 3.32. Panasonic Cell Voltage over time for charge and discharge cyles.....	105
Figure 3.33. Panasonic Cell Current over time for charge and discharge cyles	106
Figure 3.34. Panasonic cell current over time for CV region	106
Figure 3.35. Panasonic cell capacity over time for CV region	107
Figure 2.36. Panasonic cell current gradients against cycle indices	107
Figure 3.37. Deep Neural Network Model prediction of SOH.....	109

Figure 4.1. Novel Electric Vehicle Architecture with Custom Battery Pack and Universal Battery Pack Slot.....	111
Figure 4.2. Universal Battery Pack Design.....	111
Figure 4.3. CAD Model of UBP.....	112
Figure 4.4. Fabrication of UBP.....	112
Figure 4.5. Two UBPs embedded inside of a battery collection frame	113
Figure 4.7. Heating and cooling unit subsystem detail.....	114
Figure 4.8. Closed loop Cooled Battery Pack.....	115
Figure 4.9. Onboard Bidirectional Charger Block Diagram.....	117
Figure 4.10. Vehicle Body styles and classes for swappable chassis	118
Figure 4.11. Swappable Electric vehicle chassis	119
Figure 4.12. Conceptual design of a Battery Swapping Station	120
Figure 4.13. Mobile Battery Swapping Station Components	121
Figure 4.14. Electrical Design of BSS	122
Figure 4.15. Battery Swapping Station with local renewable energy generation and bidirectional charger.....	124
Figure 4.16. Battery Sharing Network (BSN) communication interface between Battery Sharing Station (BSS) and Smartgrid	125
Figure 4.17. Architectural diagram of CMS	126

LIST OF TABLES

Table 2.1. Vehicle Specification for Chevrolet Bolt.....	31
Table 2.2. Glider Model Parameters	35
Table 2.3. Motor Model Parameters	39
Table 2.4. Battery Model Parameters	41
Table 2.5. Drivetrain cooling requirements	68
Table 3.1. Summary of aging at negative electrode.....	77
Table 3.2. Summary of aging at positive electrode	78
Table 3.3. ECM of Li-ion cell parameter estimation in MATLAB	83
Table 3.4. Description of DNN data and statistics.....	108

ACKNOWLEDGMENTS

I would like to thank my advisor and mentor Dr. Kwang Y. Lee for encouraging me to pursue a Ph.D. after completion of my master's at Baylor University under his superb supervision. His mentorship and teachings laid the foundation for my readiness to completing the Ph.D. program.

I would equally like to thank Dr. Von Jouanne for taking me on as one of her graduate students in her very first year at Baylor University and being the spark that ignited the passion I have for electric vehicle research today.

I would like to thank my committee members Dr. Yokochi and Dr. Agamloh for not just simply being members of my committee but guiding me every step of the way through my research and helping answer questions I had with enthusiasm and delight, no matter how mundane or difficult the questions were.

I would like to thank my Rockstar lab mate Ben Phillips for being an invaluable asset to me throughout my experimental validation process, helping me set up experiments and troubleshoot various issues when I could not be in the lab physically. I would also like to thank every single member of my research group that has been instrumental to my work in some shape or form.

Finally, and most importantly, I would like to thank the Almighty God for giving me the patience, perseverance, and fortitude to complete this work.

DEDICATION

To my amazing wife Taylor, my mother Oluwatofunmi, and my soon to be baby girl,
Mila.

CHAPTER ONE

Background and Literature Review

1.1.Motivation

According to the U.S. Environmental Protection Agency (EPA), the transportation industry is the largest emitters of pollutant gases in the United States with 28% of greenhouse gases coming from this sector. Pollutant gas emissions from electricity and heat production is close to the second at 27% and has also increased to concerning levels as population and urbanization have increased [1]. The sustainability and environmental concerns of the pollutant gas emissions produced by these economic sectors have led to the research and development of renewable energy generation sources such as solar and wind for electricity production and the increased adoption of EV as an alternative to internal combustion engines (ICE) in the transportation sector. These alternative forms of energy generation and transportation have come with their own challenges, however.

Production of renewable energy through solar and wind can be described as a “feast or famine,” as the production is heavily dependent on the availability of wind or solar irradiation from the sun during the day. For example, as a cloud passes over solar collectors, power output from the affected collectors could suddenly drop, and once the cloud passes, the output could return to normal levels [2]. In practice, the variability of these sources of energy often leads to either a surplus of production and a need for curtailment or the lack of production required to fulfill base load. For instance, solar irradiance and the resulting power output can change as much as 80% within a matter of

seconds [2]. To address these issues, renewable energy resources like solar and wind are often installed with local energy storage, like batteries, to store surplus energy generation and fulfill base load demand when generation is not up to par or is unavailable [2, 3]. These hybrid installations result in a significant increase in the installation costs of the renewable energy generation plant as battery energy storage resources are still expensive by current standards [4].

Electrified mobility comes with its own challenges that need to be addressed challenges which include [5] :

- Cost
- Range anxiety
- Charging infrastructure
- Battery degradation

Modern EVs rely on a battery pack as the energy storage medium needed for propulsion power. These battery packs, like the energy storage medium used in hybrid renewable energy generation plants previously described, make up one to two thirds the cost of the vehicle and are expensive by current standards [5]. Current energy storage for the applications described thus far rely on Li-ion based battery chemistries due to their higher energy density, long cycle life and higher power density properties. The cost of producing Li-ion batteries is relatively expensive due to the low availability of raw materials needed, geo-political and ethical concerns in the mining and supply chain of the raw materials, the current costs of investments for research and development, tooling and expertise, and logistics needed to produce the batteries at scale. Reports discussed in [5] imply a cell cost of approximately \$150 per kWh at the end of 2016, and an additional

cost of roughly \$70 - \$100 per kWh to convert cells into battery packs that go into the vehicle. This puts the cost of the battery pack alone at \$13,000 for a 60kWh EV with an approximate 238-mile range such as a Chevrolet bolt which retails for around \$37,495 before incentives, tax rebates and subsidies are deducted [5]. These cost constraints are a barrier to the increasing adoption rate of electrified transportation despite its efficiency and simplicity benefits, as the cost of an EV is significantly higher compared to its ICE counterpart.

Secondly, despite the energy density benefits of Li-ion based batteries (265Wh/kg) compared to other types of batteries, it still pales in comparison to the energy density of gasoline and diesel, which are up to 40 times more energy dense than Li-ion batteries. Although an EV has an efficiency rating that could be 10 times or more than that of gasoline/diesel (Ex. Bugatti Veyron sports car has an efficiency of 11 MPG while a Tesla Model S sports sedan has an efficiency of 117 MPGe), the limitations of weight and volume of battery packs on-board the vehicle lead to a limited amount of drivable range on-board the vehicle and thus range anxiety for drivers of EV's with longer range requirements [6]. In addition, the required amount of time needed to conventionally charge a depleted battery pack could vary between 1 to 12 hours depending on charge type, power or charging speed, battery chemistry, battery size, and vehicle environment. Compared to filling up a vehicle at a gas station for 5 to 10 mins, these charging requirements further highlight the reason for range anxiety [7].

Global EV sales to date are currently under 10 million vehicles; however, due to government policies, incentives, and rising interest amongst major automakers, global EV sales are expected to grow up to 125 million vehicles by 2030 [8]. The future of

transportation is also largely expected to become electric and autonomous, and shared with autonomous electric (AV) cars, vans, trucks and heavy-duty vehicles delivering people, goods and services all across the globe with minimal down time requirements and high duty cycles. The levels of EV penetration predicted by market analysts imply that the majority of new vehicles sold in the near future will be electric. This in turn, means a significant shift in the fuel source distribution for transportation industry from fossil-based sources to electric. This shift requires reinforcement of electric energy infrastructure and generation as there is currently enough generation capacity in the US to absorb a few million new EVs [9]. The evolution of the transportation sector also presents an opportunity to develop sustainable solutions to the planning of utility grid reinforcements and optimal planning and deployment of the downstream charging infrastructure that are future proof.

Charging infrastructure refers to equipment and network systems that replenish the depleted reserves of energy in EVs. There are three common methods of EV charging: conductive charging (AC and DC); inductive charging (static and dynamic); and battery swapping technologies [7]. The large-scale penetration of EVs will impact the reliability and safety of the electricity grid due to the randomness and uncertainty of EV users' charging behavior in the spatial and temporal domain [10]. The decision of where and when a user is likely to charge or discharge in vehicle to grid (V2G) applications becomes increasingly difficult to predict [11]. From the distribution grid operator perspective, these decisions are dictated by a number of direct and indirect factors including: battery characteristics, power supply, EV size, geographical location, quantity/scale of EVs [12], downstream charging infrastructure, policies, incentives and

subsidies, traffic conditions, charging price, operational model, environmental impact and many more factors [13].

The challenge of modeling the charging and discharging of EVs is due to the temporal and spatial complexity of mobile EVs and the temporal complexity of EVs charging at home, office buildings, industries and so on. The future of mobility being largely expected to be autonomous and shared, adds further complexity to the charging infrastructure modeling and predictability challenge. The possibility of EVs to push power back into the grid from their onboard battery also adds further complexity to the system. Inaccurate forecasting of EV charging/discharging load, can lead to unforeseen load peaks or troughs that could be detrimental to the grid. Therefore, some form of flexibility or buffer is needed at the charging station that can accommodate for the complexities in the prediction of EV charging/discharging load such as local energy storage or generation at, or near, the EV charging station or charging location.

Battery degradation is another challenge that electrified transportation faces as it is described as one of the top concerns of EV prospective buyers [7]. Due to the inherent nature of Li-ion battery chemistries, degradation of the battery components over time is inevitable. Moreover, this degradation can be accelerated by several different factors [14]. Li-ion batteries have a very finite operating temperature range which, when exceeded, could cause temporary or permanent damage to the cells and could lead to accelerated degradation when operated at the extremes of the temperature range. Also, Li-ion batteries have a strict power density curve which dictates the charge/discharge rate and, hence, the charging power and charging speed. Direct Current Fast Charging (DCFC), for example, is a means of increasing the charging speed of Li-ion batteries and

reducing charging wait times; but repeated use of DCFC to charge Li-ion can lead to accelerated degradation of the cells [15, 16]. The configuration of Li-ion cells to form a battery pack (parallel or series connections or a combination of both [17]), operating temperature, charge/discharge cycling, depth of discharge, overcharging, charge/discharge rate, and calendar aging, all degrade Li-ion cells [18].

Aside from capacity loss (reduced attainable range) and increased internal resistance (slower charging and discharging speeds), degradation and improper monitoring and control of Li-ion battery packs could be a safety concern as well. A Li-ion cell could experience a phenomenon known as thermal runaway, which could be destructive and sometimes explosive if cells are operated or stored at elevated temperatures for too long or when cells are improperly vented [18]. The high costs of batteries as well as the safety concerns make battery degradation an imminent issue needing to be addressed. However, thermal runaway and other battery degradation mechanisms could be avoided or mitigated through advanced cell monitoring, control of charging and discharge and estimation of cell states and parameters using a battery management system (BMS) [19].

1.2. Background

Considering the challenges that exist in the shift towards renewable energy and the adoption of electrification, such as variability of wind and solar, energy storage cost, charging load modeling, charging infrastructure and battery degradation, this work presents a host of research questions, hypotheses, experiments and results as well as innovations, analysis, designs and inventions that are aimed at addressing the challenges

that have been highlighted thus far. These include methodologies for design and validation of EVs, introduction of novel concepts such as modular connected battery packs, battery sharing networks and charge management systems, battery swapping implementation enabled with V2G technologies, methods of modeling Li-ion cells, methods of balancing, monitoring, estimation and optimization of Li-ion modules and pack states and parameters.

Methodologies for designing, testing, simulating, and validating EV powertrains are described in Chapter Two of this work. Software simulation models developed in MATLAB/Simulink are validated by real-world vehicle test data from an EV chassis dynamometer with detailed analysis of the model correlation. In addition, a novel EV powertrain with battery swapping capability is designed and implemented. The configuration allows for a single motor to provide power to either the rear wheels or all four wheels on the EV through a mechanical transfer case and front and rear differentials. The configuration also allows for selection of two different gears through a gear selector on the transfer case allowing for higher efficiency and performance.

Further depicted in Chapter Two, a battery collection frame which serves as a structural member of the vehicle chassis and consists of a fifth wheel latch assembly that can be adjusted on a rack assembly to accept modular battery packs of different sizes, dimensions, and configurations. The battery collection frame may be welded or bolted to the ladder frame chassis of the vehicle. The latch assembly contains multiple components similar to a standard fifth wheel latch assembly used in on-road heavy duty trucks. Two or more fifth wheel latches are placed on the battery collection frame and adjusted via the racks to align a battery pack's mating kingpin to the latch slots and adhere the battery

pack to the electrical and optional coolant connections on-board the vehicle chassis. The fifth wheel can also be adjusted through the rack assembly to accommodate different battery pack dimensions and sizes. The latches can be released either manually by a user or automatically through a hydraulic or electrical actuator during swapping.

Chapter Three introduces the basic principles of EV battery modeling. This chapter further details the methods of battery parameterization and validation of equivalent circuit models, the degradation mechanisms of Li-ion cells and the cause and effects that occur within different components of a Li-ion cell.

An intelligent wireless battery management system (BMS) is designed and simulated that is capable of monitoring cells within a battery pack, active balancing individual cells across the battery pack, protecting the battery pack from various fail mode conditions such as overcurrent protection, over/under voltage conditions, over/under temperature conditions, measurement and estimation of states and parameters such as state of charge, state of power, state of health, internal resistance, usable capacity, operating temperature, and estimated duty cycle. Chapter Three describes the architectural design of the BMS embedded with communication of telematics of the battery pack to the vehicle on-board controller, battery swapping station or cloud connected charge management system. The BMS system is capable of actively balancing the cells on-board the vehicle during charging or shortly after charging through a balancing circuit that measures the voltage across each individual cell and slowly bleeds off overcharged cells into cells that are undercharged or released into a bleeding resistor as heat. The BMS also includes an on-board computer and wireless module used for

estimation and control of the BMS functions, and for sharing of information from the BMS to the various systems mentioned above.

Finally, an enhanced data-based deep neural network model for determination of battery state of health using a single charge/discharge curve in real time applications is also presented in Chapter Three. This model is based on the transition between constant voltage and constant current regions of charging. The algorithm can be implemented on the on-board BMS of the battery pack or in the cloud connected Charge Management System (CMS). The deep neural network model can also continuously be tuned for better accuracy, precision and speed while being updated in the on-board BMS as needed.

In Chapter Four, the structural and packaging design of a modular battery pack intended for mobile and stationary applications is described which consists of high voltage connections, an intelligent wireless on-board BMS, geographic position sensor, an on-board cooling system, a DC/DC converter, and an on-board wide-band gap bidirectional AC/DC charger. The modular battery pack is optimized for battery swapping in EV applications as well as Vehicle to Grid/Stationary applications for providing ancillary services to the grid as described in [20] – [26]. The physical enclosure of the battery pack is designed with the intent to mate with the battery collection frame detailed in Chapter Two. The flexibility of the battery pack designs and the modularity of EV powertrain also makes them uniquely suited for military applications, achieving most of the requirements while also mitigating some of the challenges aforementioned [27].

Another variation of the modular battery pack consists of a closed-loop cooling system. Instead of having external inlet/outlet, this battery pack variation will contain all the components for cooling within the battery pack itself. The closed-loop cooling system

in one specific design consists of an electric fan, an electric pump, a chiller plate, a radiator, a heater coil, an electric AC compressor, and hoses, all within the battery pack itself. The electric components in the pack are powered through the DC/DC converter that is on-board the battery pack, eliminating the need for an external power source.

In another design iteration, the cooling system features an air-cooled heat sink that is pressed onto one or more sides of the battery pack, separated by a heat exchange material such as aluminum, which will also form part of the structure of the battery pack. This novel design allows for ease of battery swapping and opens up the opportunity for use in stationary applications as the battery pack can easily be connected to the vehicle chassis with fewer connections and does not require complicated liquid coolant connections during battery swapping. This design also allows for the battery pack to function as an independent power source when used in stationary applications or charged off-board the vehicle at a battery swapping station.

Chapter Four also depicts the design of a swappable EV chassis. The swappable chassis allows for a variety of vehicle body platforms to be combined with the same EV chassis. The swappable chassis features the electric powertrain, battery collection frame and modular battery pack described in this work. It also incorporates a steering rack motor that can be controlled wirelessly through a steering wheel sensor, a wireless embedded controller for controlling the electric motor and braking system through wireless signals from the throttle and brake pedal on-board the interchangeable vehicle body. Finally, the described swappable EV chassis allows for wireless selection of drive modes and gears from a wireless gear selector on-board an interchangeable vehicle body. The swappable EV chassis design is geared towards commercial transportation and future

autonomous shared transportation, allowing for the EV powertrain to become agnostic to the vehicle body and improving vehicle utilization for various applications.

Chapter Four also describes a grid-interfaced battery sharing network consisting of battery swapping stations that share information amongst each other, a cloud connected management system and the distribution grid. A benefit of the battery sharing network is its ability to provide a means by which EVs can share the battery, the most valuable resource, amongst each other, through the optimization of different duty cycles of vehicles within the network. This in turn reduces the overall cost of the EVs, maximizing the unit utilization of the scarce battery resource. The charge management system optimizes charging and discharging schedules of battery assets across the network, allowing for batteries to be charged off-board the vehicle at much slower rates, based on electricity demand and price signals [21], and then be swapped into a vehicle quickly [23], reducing the need for DCFC and avoiding its degradation effects on the battery while unused batteries can provide ancillary services to the grid. The battery swapping network is designed in such a way that the charging load is much more predictable, as the battery packs are scheduled ahead of time, and it can take advantage of the “feast or famine” nature of renewable energy generation with an aggregation of battery swapping stations, providing temporary energy storage buffers to store energy when there is surplus and returning some of that energy back into the grid when demand exceeds generation [28], thereby reducing the cost and overall emissions of the energy grid [29]. The design of the battery swapping infrastructure and battery packs also provides an added benefit for the second-life use of the batteries as they can be easily converted to permanent stationary energy storage. The battery swapping stations within

the battery sharing network are connected and communicate through Internet of Things (IoT) to optimize the charging costs of the battery packs, maximize utilization of the battery packs, and reduce wait times for battery swapping or vehicle chassis swapping through scheduling and forecasting of swap demand, grid energy demand and price, and optimal routing of mobile battery swapping stations.

In addition, a mobile EV battery swapping station is briefly described in Chapter Four which consists of a battery/vehicle chassis storage rack, rails/rollers for moving battery packs within the battery storage unit, a thermal management system for storing battery packs at optimal temperature, a mechanism for removal and addition of battery packs either manually or automatically, a monitoring apparatus for communicating with battery packs, battery chargers and the charge management system communication interface. Finally, Chapter Five presents the conclusion of the dissertation and highlights future research opportunities.

1.3. Research Contributions

The contributions of this research work include the development of a highly scalable and robust simulation, prototyping and analytics framework for EV research and development. The framework includes vehicle/battery modeling and simulation, battery management system development and controls, battery state health estimation through the use of deep learning models, and battery aging mechanism analysis. Other contributions include novel concepts such as, Modular Swappable Battery Pack design, Modular EV Chassis design, Battery Swapping Stations/Networks, and Grid-Interfaced Charge Management Systems.

CHAPTER TWO

Electric Vehicle Powertrain Design

2.1. Introduction

The design methodology of EV powertrains occurs in different phases, starting from the gathering of general requirements, such as initial acceleration, rated and maximum vehicle velocity, maximum gradeability, minimum vehicle range, maximum charging power and maximum speed. Following the gathering of vehicle general requirements, a series of vehicle models are developed and simulated within a design of experiments (DOE) context to attain these requirements. These models can be steady-state, quasi-steady state or dynamic. The simulations could occur on the system level, sub-system level or component level depending on the stage of development. The main components of the powertrain include the traction motor and inverter, the transmission, and the traction battery. EVs are unique in the sense that the powertrain topologies can vary significantly for any given requirement. For example, a single electric motor as seen in the Chevrolet Bolt [30], dual motors as implemented in performance versions of the Tesla Model S [31], or even quad motors could be used at each wheel for traction motor/torque requirements.

A variety of motor topologies such as induction motor, permanent magnet and switched reluctance motors can also be used [32]. A unique advantage of electric motors is that it provides flexibility of the orientation of the motor mounts within the vehicle such as the motor being mounted parallel, axially, or radially to the vehicle chassis. The

choice of gearshift such as single or multispeed transmissions also depends on vehicle requirements and electric motor choice and configuration. A single speed transmission can be used with the choice of an optimal gear ratio that allows for the vehicle to reach its maximum speed while still attaining reasonable torque at low speeds as implemented in the Chevy Bolt [30] described in Figure 2.1. Multiple motors at each axle with different gear ratios can be used in combination to allow for a faster acceleration at lower speeds, while switching to a single motor with smaller gear ratio at higher speeds to attain much a higher maximum velocity, as implemented in the Tesla Model S [31], described in Figure 2.2. A multispeed transmission can also be implemented [33], as seen in the Porsche Taycan described in Figure 2.3.



Figure 2.1. Chevrolet Bolt, Single Speed Direct Drive Unit [31].

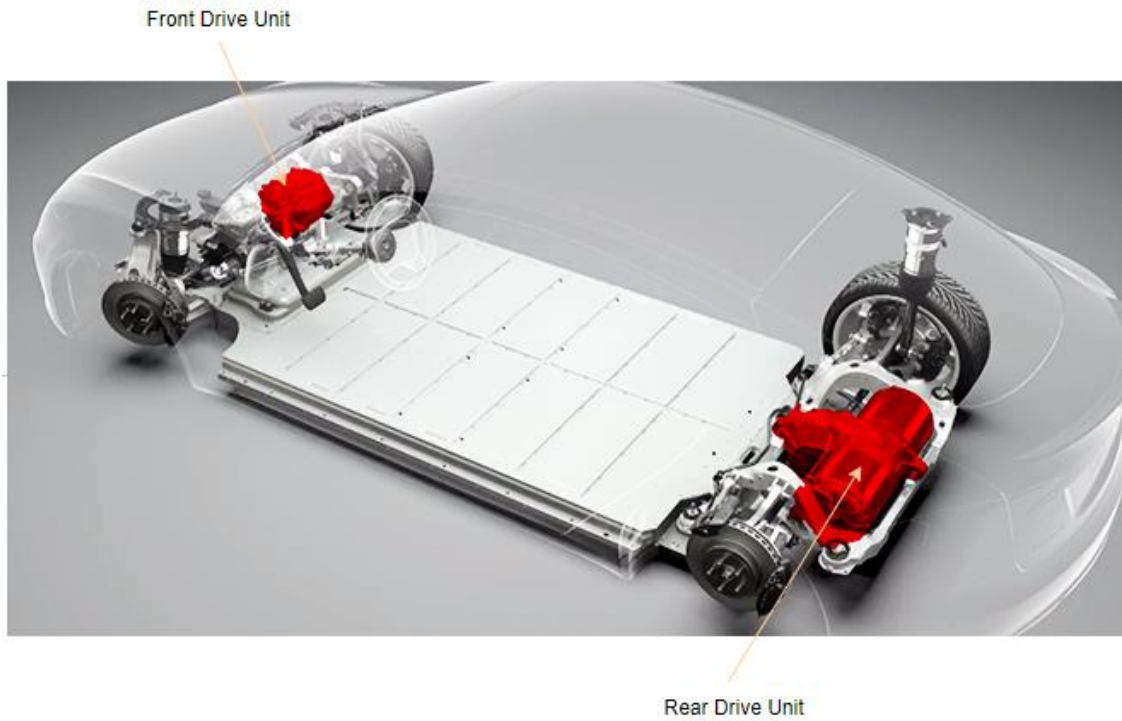


Figure 2.2. Tesla Model S Dual Motor, AWD Drive Unit [59].

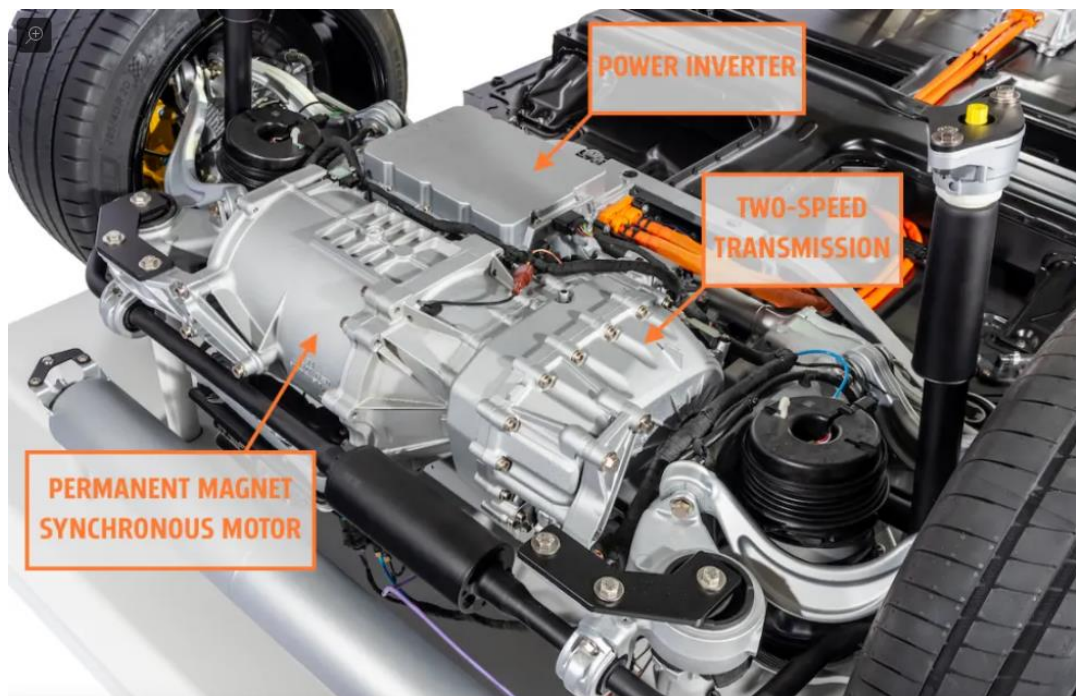


Figure 2.3. Porsche Taycan Rear Drive Unit with Two-speed Transmission [34].

The energy source of an EV (EV) is typically electrochemical and portable, usually in the form of a battery pack. Several types and chemistries of batteries exist. However, the most common type in modern EVs is the Li-ion battery. Li-ion batteries are further divided into several different types of chemistries. Most Li-ion batteries comprise of a Carbon or Lithium Titanate ($\text{Li}_4\text{Ti}_5\text{O}_{12}$) negative electrode, a mixture of lithium salts and organic solvents as electrolyte and a variety of positive electrode material, such as Lithium Cobalt Oxide, Lithium Nickel Oxide, Lithium Manganese Oxide, Lithium Nickel Manganese Cobalt Oxide and many more forms of lithium metals [6]. The dominance of Li-ion batteries in EV applications is due to its high energy and power density compared to other chemistries.

The choice of positive electrode is further driven by specific properties of each chemistry, such as energy density, power density, columbic efficiency, stability and sensitivity to temperature [35]. Each chemistry and molecular structure pose different benefits and drawbacks, including energy density, power density, safety, cost and longevity or life [35]. The choice of battery chemistry or technology is specific to the EV application. Figure 2.4 is referred to as a Ragone plot. It provides a graphical comparison of several battery chemistries based on their specific energy density, which is an indication of energy storage per unit mass, and volumetric energy density, energy storage per unit volume. From the plot, it is obvious that Li-based chemistries favor both characteristics. However, due to inherent limitations in materials, cell architectures, safety and temperature management packaging, commercially available Li-ion batteries are limited to specific energy densities of around 250Wh/kg [36].

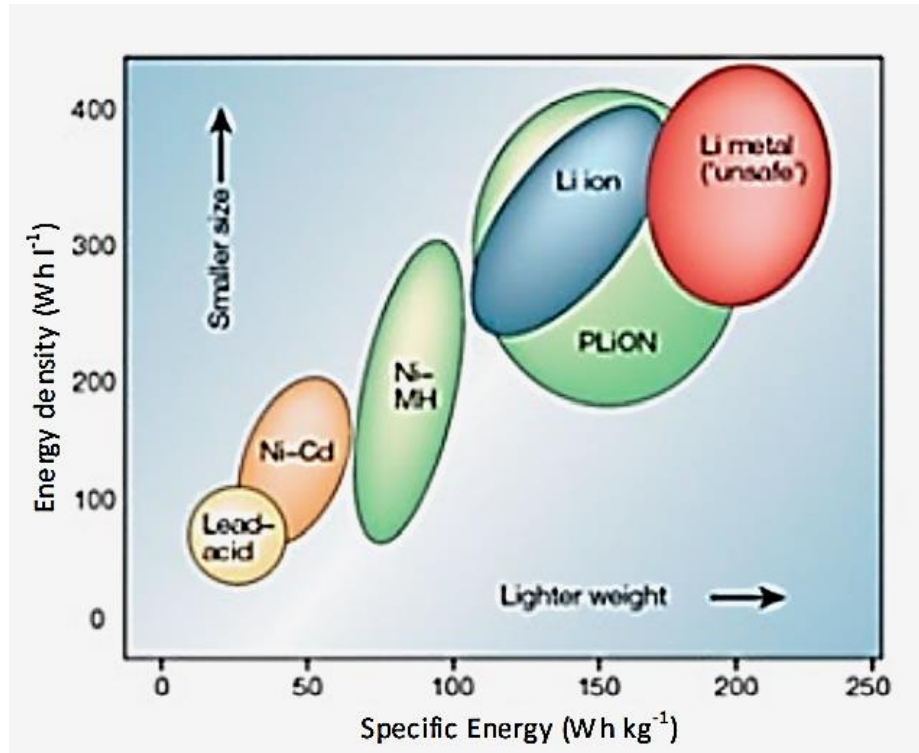


Figure 2.4. Ragone plot of battery chemistries [6].

Another critical component of EVs is an electrical controller commonly referred to as the Battery Management System (BMS). The BMS monitors and controls the battery charging/discharging to maintain balance in the cells and keep the cells within operating temperature range. Another equally important group of components in an EV are the power processing units, also commonly referred to as the power electronic converters. Figure 2.5 is a diagram highlighting the overall system architecture of an EV.

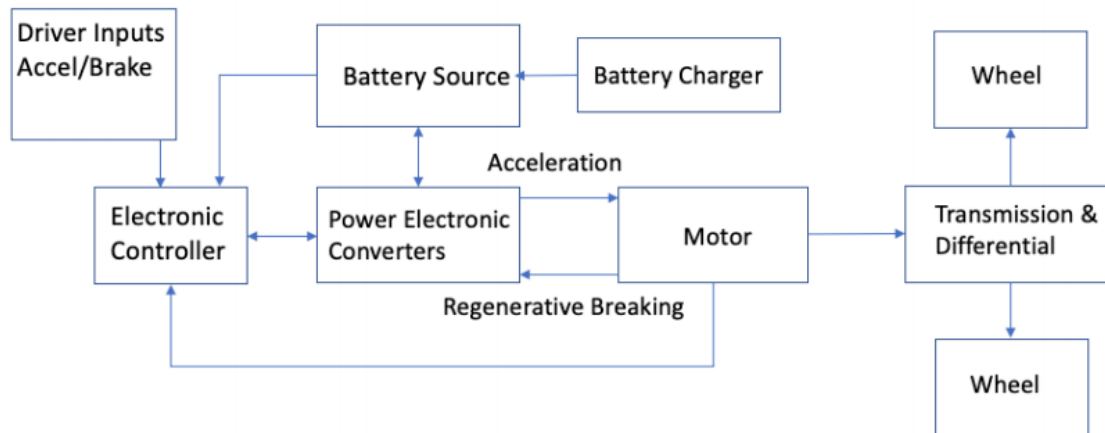


Figure 2.5. EV architectural diagram.

Due to the number of choices for components available in the design phase of an EV, a design of experiments (DOE) is typically carried out to validate the vehicle component configurations that meet certain design requirements. During the DOE phase, several vehicle configurations are modeled, simulated, and documented at various levels of complexity – system level, sub-system level and component level. After adequate modeling and simulations have been implemented and analyzed and validated to meet the proposed vehicle requirements, sometimes involving some Hardware-In-Loop simulations, a vehicle validation prototype is then built and driven through various safety, efficiency and performance testing phases [37] in order to validate the simulated results. This chapter presents a detailed methodology for modeling, simulation, and validation of an EV based on given vehicle requirements. Furthermore, the development, implementation, and validation of a novel EV powertrain architecture prototype is described.

2.2. Dynamics of Vehicle Motion

For equation-based modeling, the dynamics of vehicle motion must be formulated and then implemented in the form of subsystems, blocks and signals within Simulink. This section summarizes the equations that govern vehicle motion needed for modeling implementation. Newton's second law states that the acceleration of an object is proportional to the net force exerted on it. In other words, an object accelerates when the net force exerted on it is nonzero. Similarly, a vehicle moves due to the force of the propulsion unit (the powertrain) overcoming the gravitational force of the vehicle exerted on the roadway, the air resistance and the tire rolling resistance. The acceleration and speed at which the vehicle moves are dependent on the power delivered to the wheel by the powertrain, the curb mass of the vehicle (including all of the components and passengers on-board), the condition of the roadway and the aerodynamics of the vehicle on the roadway. When a vehicle is accelerating, the vehicle is subject to the forces described below.

$$k_m m \frac{dv_{xT}}{dt} = F_{TR} - F_{RL} \quad (2.1)$$

where F_{TR} is the tractive force provided by the electric machine, F_{RL} is the road load force, m is the vehicle mass, v_{xT} is the velocity in the tangential direction of the roadway, k_m is a rotational inertia coefficient that accounts for a vehicle's onboard rotating mass, and the term $k_m m \frac{dv_{xT}}{dt}$ is the net force acting on the vehicle that propels the vehicle forward. The road load force acting on the vehicle consists of a gravitational

force F_{gxT} , the rolling resistance of the tires F_{roll} , as well as an aerodynamic drag force

F_{AD} :

$$F_{RL} = F_{gxT} + F_{roll} + F_{AD} \quad (2.2)$$

$$F_{gxT} = m \cdot g \cdot \sin \beta \quad (2.3)$$

$$F_{roll} = m \cdot g \cdot \cos \beta (C_o + C_1 v_{xT}^2) \quad \text{for } v_{xT} > 0 \quad (2.4)$$

$$F_{AD} = \frac{1}{2} \rho C_D A_F (v_{xT} + v_0)^2 \quad \text{for } v_{xT} > 0 \quad (2.5)$$

where β is the grade angle, g is the gravitational constant, C_o and C_1 are coefficients of rolling resistance, ρ is the air density, C_D is the aerodynamic drag coefficient, A_F is the equivalent frontal area of the vehicle, and v_0 is the head wind velocity. The second order relationship between aerodynamic drag and speed is described in Equation 2.5. A free-body diagram showing the forces acting on an EV represented by the black dot is shown in Figure 2.6 [37].

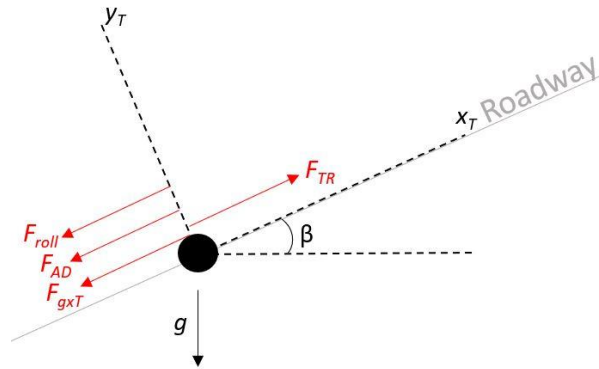


Figure 2.6. Free body diagram of forces acting on an EV [37].

The tire-road interaction of the vehicle and the traction properties of the tire-road interface are fundamental to the dynamics of a vehicle. The traction torque from the

propulsion system is converted into a traction force through the interaction between the pneumatic tire and the road surface at the tire-road interface [53] illustrated in Figure 2.7. The speed of tire and the longitudinal speed of the vehicle vary in magnitude and direction and are a function of the forces acting on the tire, including the vertical load force that the vehicle body exerts on the wheel, F_z , and the longitudinal forces exerted on the tire at the tire-road interface, F_x . The rolling speed of the tire is related to the tire angular velocity ω and wheel radius r_w and is given by

$$v_{tire} = r_w \omega \quad (2.6)$$



Figure 2.7. Speed and forces in the tire-road contact patch area [39].

The ratio of the longitudinal velocities of the vehicle v_x and the tire v_{tire} , is defined as the wheel slip s given by

$$s = 1 - \frac{v_x}{v_{tire}} \quad (2.7)$$

During braking, the slip of the vehicle is given by

$$s = 1 - \frac{v_{tire}}{v_x} \quad (2.8)$$

2.3. Electric Vehicle Powertrain Sizing

Powertrain sizing refers to the calculations needed to aid in the mathematical modeling and simulation of EV powertrains. The process begins with the determination of certain design specifications which include initial acceleration, rated velocity on a given slope, maximum % grade, maximum steady-state velocity and maximum range [38]. The two main components that govern the highlighted design specifications are the electric motor and battery pack. Sizing of the electric motor involves finding the power rating of the motor and the operating speed range of the motor.

Electric motor rated performance is governed by a graph commonly referred to as the torque/speed envelope. Figure 2.8 is an example of a typical torque speed envelope of an electric motor.

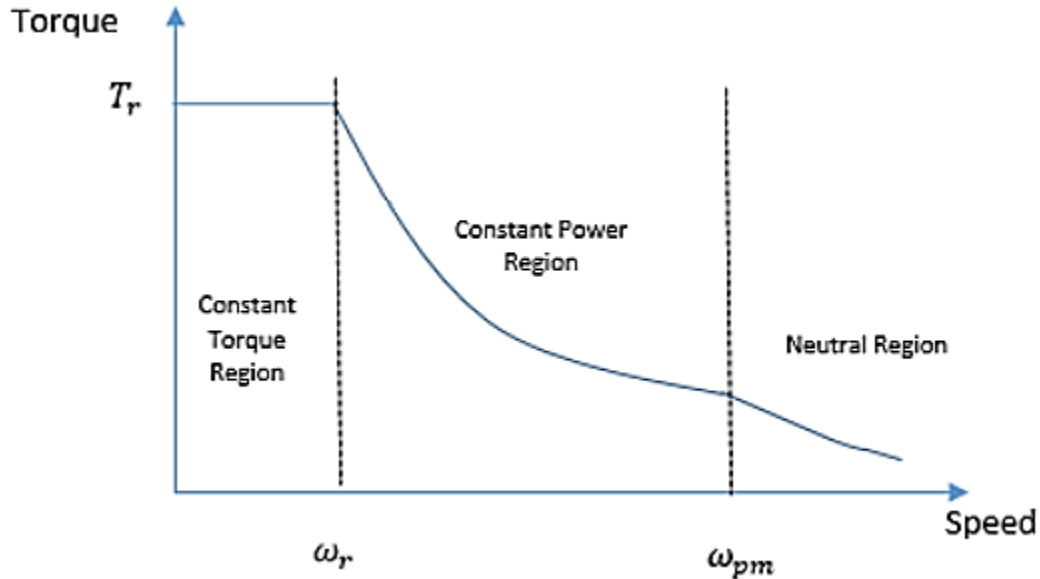


Figure 2.8. Torque speed envelope of an electric motor [38].

There are three main distinguishable segments of the torque speed envelope: constant torque region, constant power region and natural mode region. Within the constant torque region, the motor delivers the maximum rated torque until the base speed, ω_r , is reached. The motor rated speed is an indicative of the speed at which the motor can deliver the rated torque at rated power. Beyond the rated speed, the motor operates in the constant power region where torque steadily falls off at a rate that is inversely proportional to the speed of the EV. Electric motors can attain higher speeds beyond the rated speed due to a field weakening phenomenon that occurs within the constant power region. In the third, natural mode region, the motor torque falls more rapidly, as it falls at a rate inversely proportional to the square of the speed. In most cases, the EV motor is designed to operate mainly within the constant torque and constant power region; however in some cases, the reduced power characteristics of the natural region could be useful for efficiency and range [38].

To eliminate the need for multiple gears, the control of the transition between constant torque and constant power regions of electric motor, and thus speed control, could be achieved solely from a power electronic motor drive component. However, the speed range of the electric motor's constant power region is important to the sizing of gear components. The size of the electric motor depends largely on the maximum torque requirement of the motor. Increasing maximum torque delivered in the constant torque region is a function of the motor's physical size. The motor is designed for high-speed operation for a given rated power and then matched to the speed of the wheels through gears to minimize the size and weight of the electric motor. Therefore, there are tradeoffs between component size, maximum torque, motor constant power speed range, rated speed (speed at which the motor delivers maximum torque at maximum power), gear ratios and motor efficiency. These tradeoffs can be addressed through implementation of multiple gears and motors when power requirements are prioritized over efficiency, as seen in the Porsche Taycan propulsion system design [34] and through advanced gearshift control algorithms [33]. The Taycan consists of two electric motors transversely mounted to produce an all-wheel drive system. The motor in the rear, described in Figure 2.3, is the more powerful motor, with 449 horsepower and 406 lb-ft of torque coupled to a two-speed gearbox with roughly 16:1 first gear ratio and second gear ratio of 8:05:1. The motor in the front is a single-speed drive module with roughly 255 horsepower and 325 lb-ft of torque and a final gear ratio of 8:05:1, the same as the second gear on the rear motor. The physical description of the front and rear motors of the Taycan is described in Figure 2.9. The Taycan's motors are both rated for a maximum speed of 16,000 RPM. As shown in Figure 2.10, during the initial launch, the rear motor

in the 1st gear produces a wheel torque at a ratio of 16:1, and the front motor produces max torque to the wheel at a gear multiplication of roughly 8:05:1 reaching a combined wheel torque of almost 12,000 Nm. At around 100 km/h or roughly 62 mph, the rear motor first gear starts to run out of steam and upshifts to the second gear, essentially increasing the constant power speed range of the motor. In this design, the second gear is prioritized for range and efficiency while the first gear is prioritized for performance. In some use cases where range and efficiency are desired over performance, the rear transmission can be decoupled to reduce losses, allowing the vehicle can run completely in front-wheel drive.

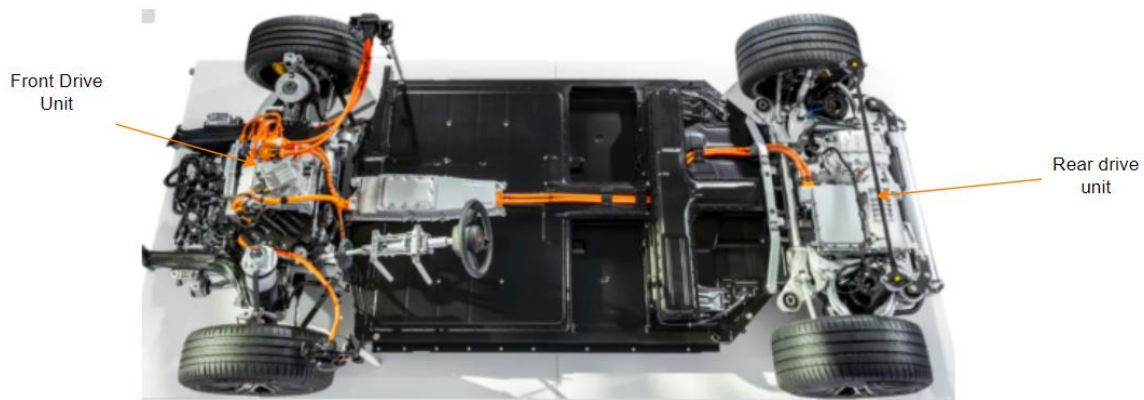


Figure 2.9. Porsche Taycan Powertrain Architecture [34].

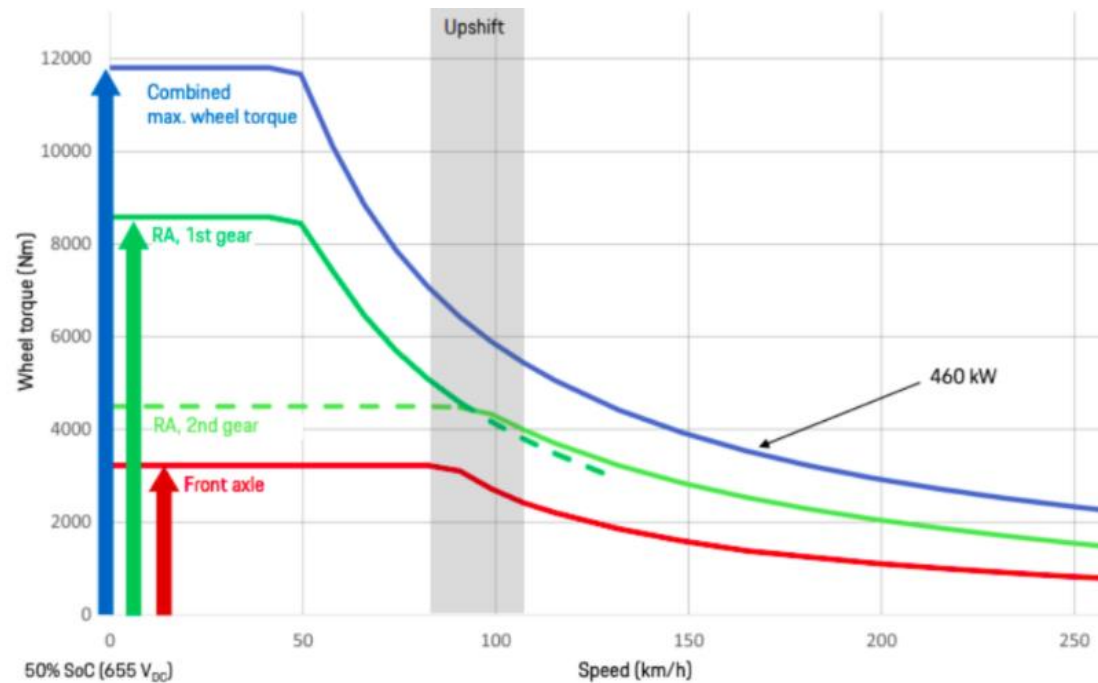


Figure 2.10. Porsche Taycan AWD dual motor, two-speed shifting strategy [34].

The width of the constant torque region or rather the base speed rating of a motor and consequentially the peak power rating of a motor is directly proportion to the input voltage to the motor. Figures 2.11 and 2.12 are torque speed curves and power speed curves of a BorgWarner 250 hp electric motor. It can be observed from the plots, that the DC bus voltage from the battery pack changes the torque speed envelope characteristics of the motor. Therefore, it is important to make the right trade-offs in power and energy specifications that allow for desired maximum power ratings of the electric motor when determining the component sizing of the battery pack.

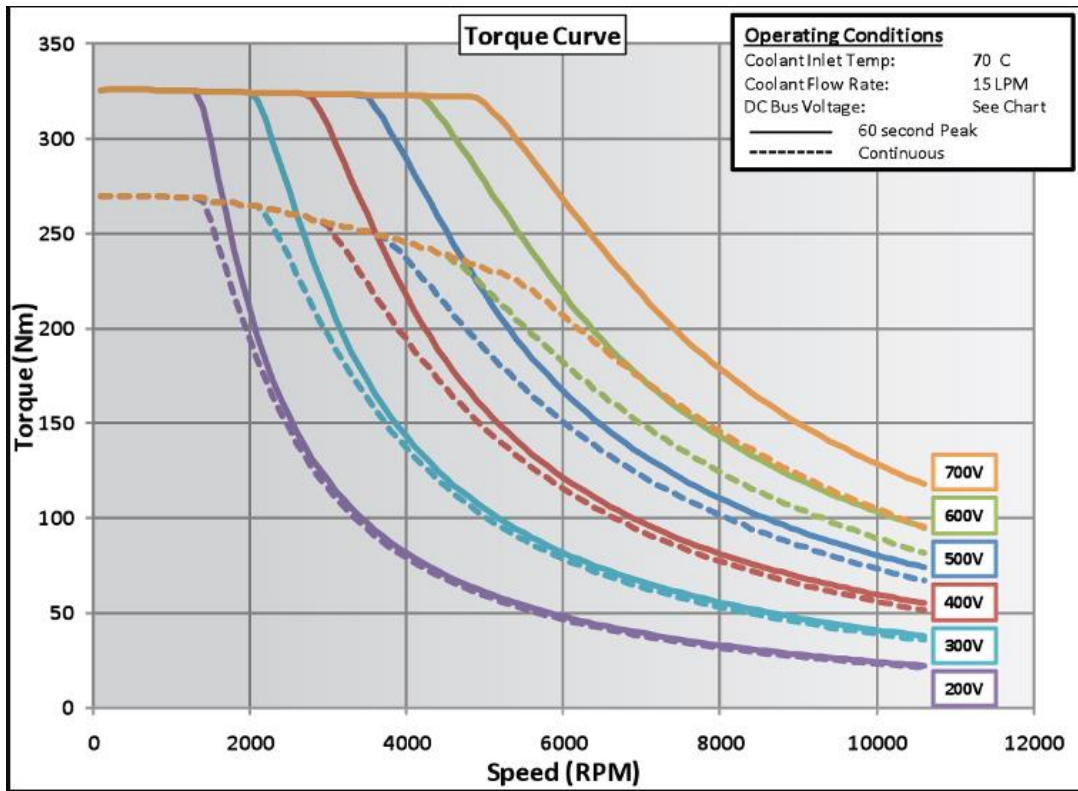


Figure 2.11. BorgWarner 250 hp electric motor torque-speed envelope [40].

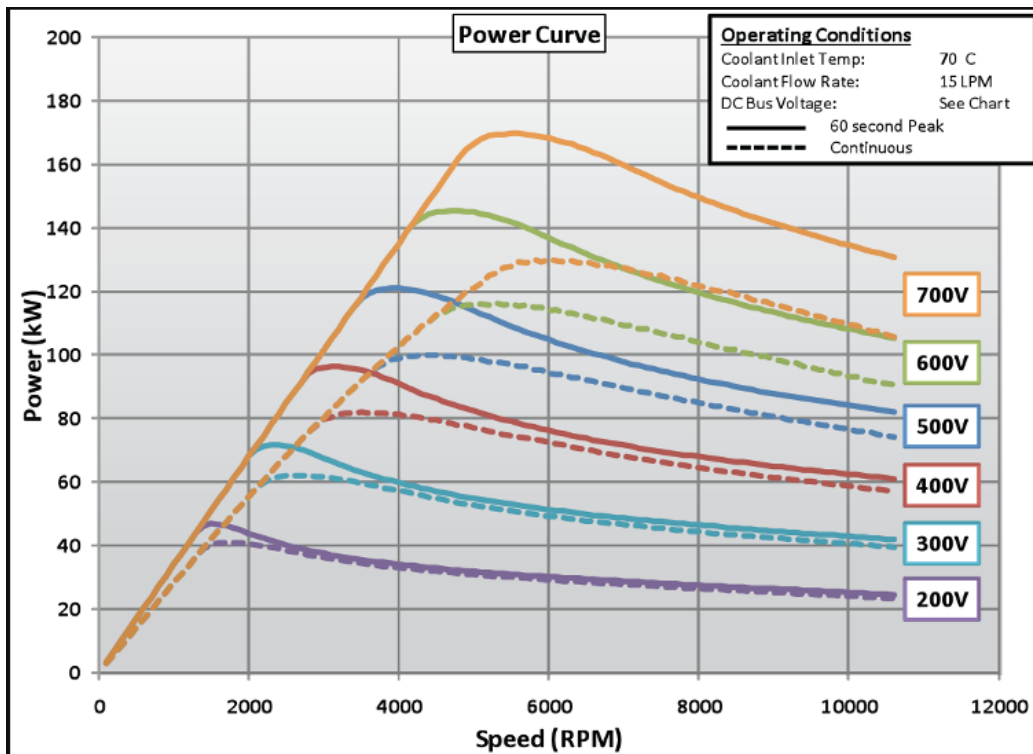


Figure 2.12. BorgWarner 250 hp electric motor torque-speed envelope [40].

2.3.1. Initial Acceleration and Rated Velocity

Initial acceleration is specified as time t_f it takes for the vehicle speed to reach rated speed v_f , where $v_f = \omega_{fwh}$ (*rated wheel speed*) * r_{wh} (*radius of the wheel*), the vehicle rated speed. For any given initial acceleration specification, the design problem is trying to find the minimum tractive force F_{TR} needed to overcome the road load forces F_{RL} which are based on some initial educated guesses and assumptions for rolling resistance, aerodynamic drag and so on. The equation below, for acceleration, can be used to determine the minimum tractive force needed to accelerate the vehicle to the rated velocity from 0 for a given vehicle mass [38].

$$a = \frac{dv}{dt} = \frac{F_{TR} - F_{RL}}{m} \quad (2.9)$$

2.3.2. Maximum Velocity

The specified maximum velocity indicates the maximum attainable steady-state velocity of the vehicle under inspection. The tractive power, $P_{TR,max}$, needed to attain and maintain the maximum velocity, v_{max} , during the constant power region is given by

$$P_{TR,max} = mgv_{max} \sin \beta + (mgC_1 + \frac{1}{2} \rho C_D A_F)v_{max}^3 + mgv_{max} C_0 \quad (2.10)$$

2.3.3. Maximum Gradeability

The maximum gradeability is defined as the maximum percentage grade incline that the EV can accelerate to the rated speed. The max grade is defined by the tractive force, as seen in Equation 2.11, and is typically determined alongside the initial acceleration tractive force requirement [53].

$$\text{Max. \% grade} = \frac{100F_{TR}}{\sqrt{(mg)^2 - F_{TR}^2}} \quad (2.11)$$

2.4. Electric Vehicle Modeling and Simulation

Understanding the operation of the EV under a variety of driving and environmental conditions is critical to optimizing vehicle performance, vehicle health and vehicle safety. Some of the conditions that could affect vehicle performance include temperature, road conditions, road grade/elevation, aggressive/conservative driving, etc. To estimate these metrics and make the critical design and control decisions needed during vehicle design and vehicle validation, the EV powertrain must be modeled accurately and simulated and analyzed in a scalable fashion. Furthermore, these models must be flexible and robust enough to be tuned based on the real-world data to provide improved vehicle serviceability once the vehicle is in the field. Vehicle modeling occurs in different forms, such as mathematical models, steady-state models, multi-physics domain physical modeling, and dynamics and transient modeling. Vehicle modeling can also occur at different levels of fidelity and precision, such as system level modeling, component modeling or sub-system level modeling. The selection of the model type and modeling tools is indicative of the kinds of questions that the model is expected to answer or the forms of analysis we intend to perform on the modeling result. However, the reliance on simulation-based platforms alone for the validation of vehicle models is insufficient, and the development and testing of vehicle prototypes for public road testing could be unsafe, impractical and sometimes very costly. Therefore a balance between simulation and some level of real-world testing in a scalable fashion is necessary in the development of high performance EV powertrains.

MATLAB/Simulink software is a tool capable of modeling complete EV powertrains of different levels of fidelity and detail. This software features a variety of shipped sample models and has been used in literature for simulation of purely electric and hybrid EVs of different configurations and types [41, 44]. In this section, we describe the modeling and simulation steps for EVs by defining some vehicle specifications and then developing an equation-based model of a full Battery EV in MATLAB/Simulink software.

2.4.1. MATLAB/Simulink

Simulink is a quasi-standard for control system design in academia and industry [39]. It is the baseline tool that supports many add-ons which can be used in vehicle modelling, such as SimPowerSystems and SimDrivelink [44], Advisor [43], Simscape, Powertrain Blockset, etc. Simulink supports an equation-based modeling approach, data-driven modeling approach, as well as a physical modeling approach for vehicle modeling. Simulink also supports code generation for hardware testing and deployment, testing and analysis framework for test case management and report generation. This work employs an equation-based model developed by MATLAB/Simulink as a base vehicle model. The model was then significantly modified to meet the vehicle specifications of the high performance EV which was benchmarked on a chassis dynamometer. The modeling goal is to test for the efficiency and performance of the EV as the results of the model are validated by real-world tests on the target EV platform.

2.4.2. Vehicle Specification

The EV powertrain modeling and simulation begins with the determination of key design specifications as detailed in Table 2.1, which is adapted from the spec sheet of a

Chevrolet Bolt pure EV. This specific vehicle has been selected intentionally as the results of the simulation can be compared to real world vehicle tests later in the chapter.

Table 2.1. Vehicle Specification for Chevrolet Bolt

Initial Acceleration (0 – 60mph)	7.5 secs
Curb weight	1616.15 kg
Motor power	200hp/150kW
Motor torque	266 lb.ft/360Nm
Final Drive ratio	7.05:1
Energy efficiency	300 Wh/mile
Battery Capacity	53kWh
Top speed	93mph
Aerodynamic Drag coefficient	0.308

For equation-based modeling, the dynamics of vehicle motion as described in the vehicle dynamics section, are formulated and then implemented in the form of subsystems, blocks and signals within Simulink. The vehicle model is then initialized with the modelling parameters described in Table 2.1, and simulated through what is known as a “drive cycle”. The derivation of the modeling parameters typically occurs through some initial tests on the target hardware such as no load tests of the motor on an electric motor dyno, cycle tests on the battery pack with battery cyclers or this data can be retrieved directly from the manufacturer spec sheet. Following the drive cycle simulation, the target vehicle platform is prototyped and the same drive cycles and conditions can be validated on the real-world vehicle platform with an EV chassis dynamometer.

2.4.3. Drive Cycles

The EPA sets standards for determining vehicle efficiency and capabilities, such as EV range. These tests are carried out in controlled environments and have, historically, relied on Single Cycle Test (SCT) methodology for determination of range and

efficiency. To better characterize the effects of temperature and accessory loads on range for battery EVs and to reduce lab test burden, a new test procedure, known as the Multi-Cycle Test (MCT), was introduced. The MCT testing procedure reduces the testing time of EVs by over 75%, from over 18 hours to just over 4 hours. The degree of fidelity and accuracy of the tests are described in [45]. To test the efficiency of the EV modeled in this section with a specified maximum torque of 360 Nm, a form of MCT test was used. This test included a combination of the aggressive US06 drive cycle and the Highway Fuel Economy Test (HWFET). The US06 cycle represents an 8-mile (12.8 km) route with average speed of 48.4 mph (77.9 km/h), maximum speed 80.3 mph (129.2 km/h) and duration of 596 seconds. The HWFET cycle lasts a duration of 765 seconds, with a total distance of 10.26 miles (16.45 km) and average speed of 48.3 mph (77.7 kph). The total time and distance for the MCT test (Drive Cycles 1-3 as shown in Figure 13) is ~22 min and 18.26 miles long (29.3 km), respectively.

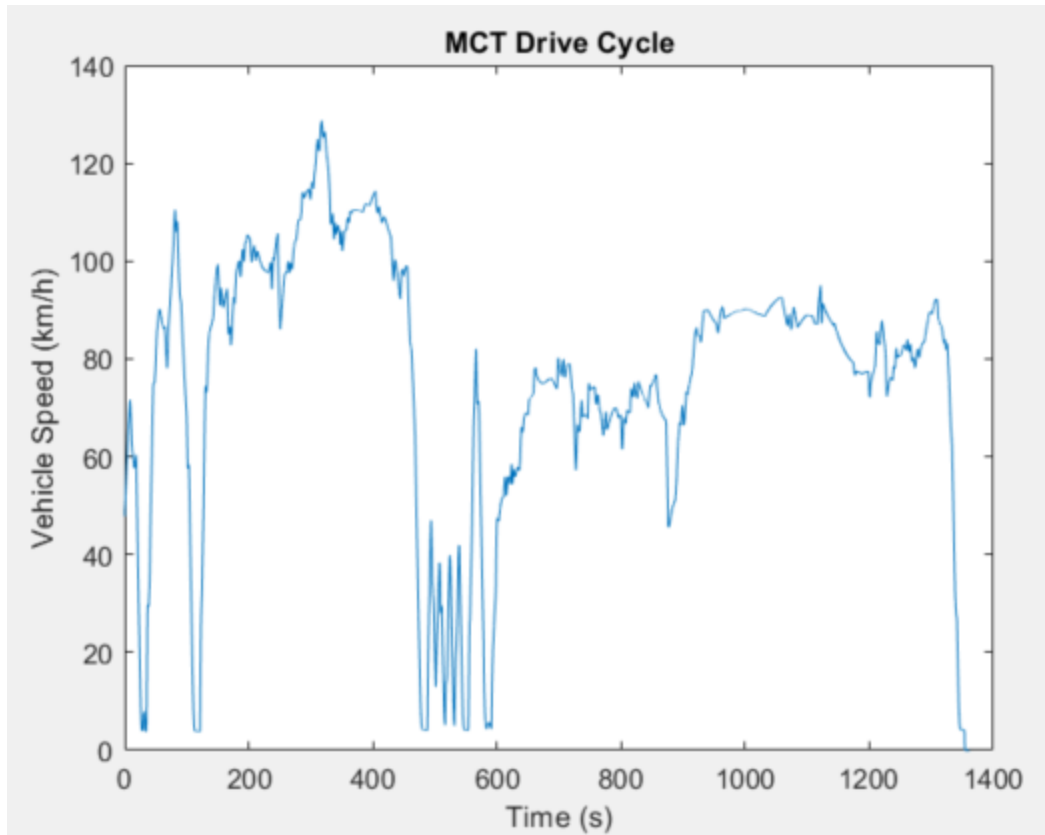


Figure 2.13. MCT Drive Cycle.

2.4.4. Equation-based Modeling

The equation-based modeling approach in Simulink involves the representation of each vehicle component or subsystem as a series of equation blocks connected to each other through signals that are calculated and updated at each time step. Figure 2.14 is an overview of the equation-based model in Simulink to meet the EV specifications previously described.

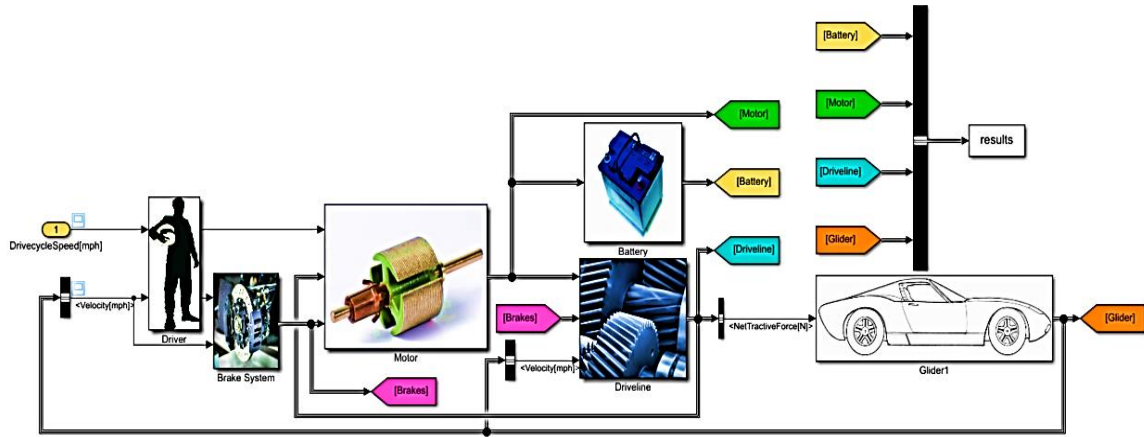


Figure 2.14. Simulink Equation Based EV Model [39].

2.4.5. Glider Model

The glider model represents the point mass model of the vehicle dynamics previously described. It sums up the forces acting on vehicle body represented by a point mass, as described in Figure 2.15 and Equations 2.1 – 2.5. Table 2.2 is a summary of parameters used for the calculation of vehicle dynamics and determining the vehicle speed at each timestep. Figure 2.16 is a closer look at the glider model subsystem within the Simulink model where the Equations 2.1 – 2.5 are implemented by taking in an input of tractive force and subtracting the summation of the road load forces to get the inertial force, which is converted into an acceleration based on the vehicle mass and then integrated over time to form the output of the model, vehicle speed, which is then fed back to the driver control subsystem in Figure 2.18. Figure 2.17 is a block diagram which represents the calculations for determining values such as distance, tractive energy consumed, tractive power, velocity, braking energy and so on. Note that simulation block inputs are indicated with yellow and block outputs are indicated with red.

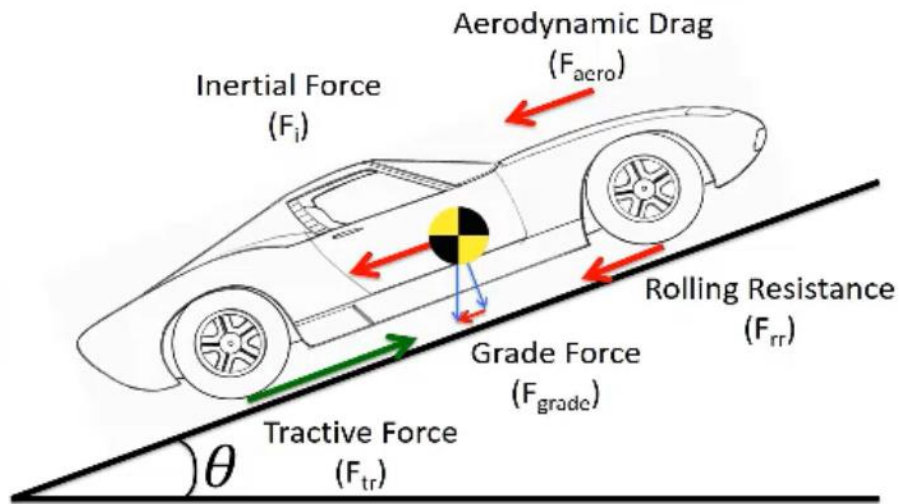


Figure 2.15. Vehicle Body Glider Model [39]

Table 2.2. Glider Model Parameters [39]

Parameter	Unit	Description	Value
ρ	kg / m^3	Air Density	1.23
C_d	-	Drag coefficient	0.38
A_f	m^2	Vehicle frontal Area	2.1
V	m / s	Vehicle Speed	-
a	m / s^2	Vehicle acceleration	-
m_i	kg	Vehicle inertial mass	1678.30
m	kg	Vehicle Mass	1616.15
g	m / s^2	Gravity	9.81
θ	Degrees	Road angle	0
C_{rr}	-	Rolling resistance coefficient	0.01

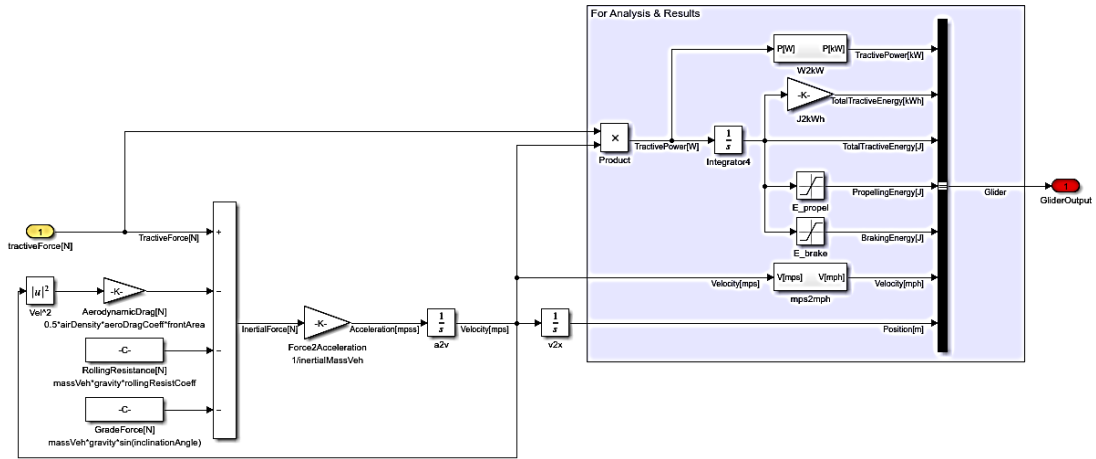


Figure 2.16. Vehicle Glider Model Subsystem [39]

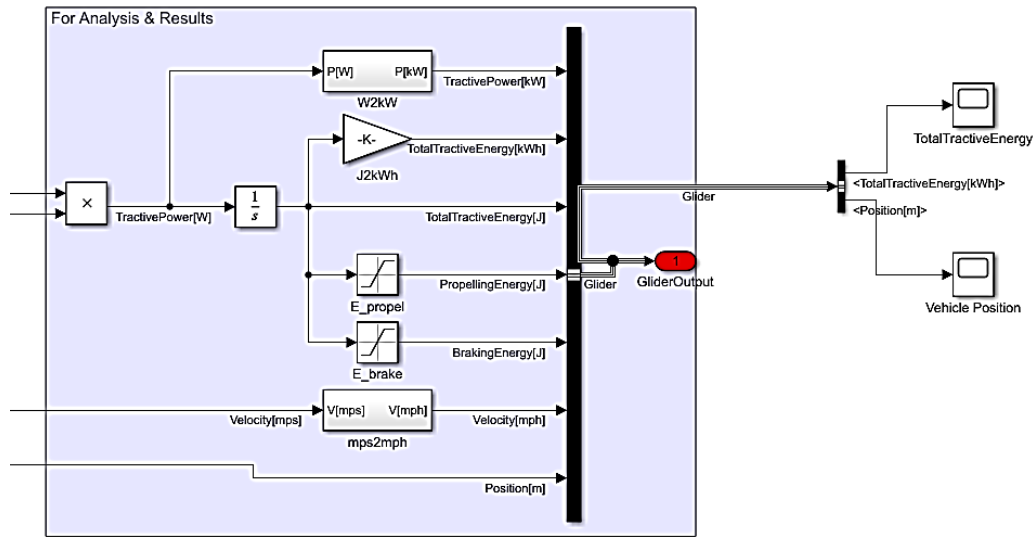


Figure 2.17. Energy and Power Analysis of Glider Model Subsystem [39]

2.4.6. Driver Model

The inputs to the driver control block are the drive cycle reference speed and the vehicle speed feedback from the glider model block. The error between the two speeds is

fed back into the PID controller and the output is a driver command of either an accelerator pedal position (APP%) or a brake pedal position (BPP%).

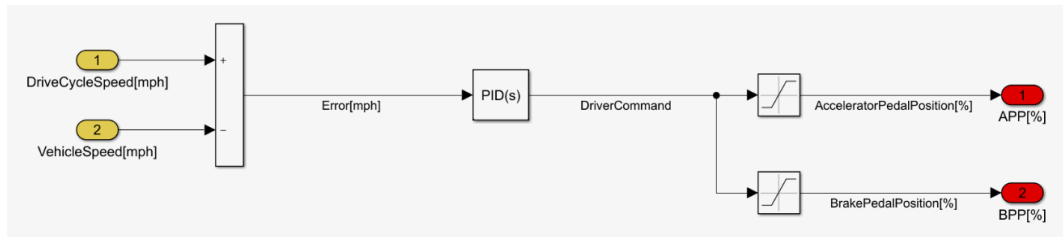


Figure 2.18. Driver Control System Block [39]

The modeling approach of the driver subsystem mimics a real-world driver control operation, where the driver is the PID controller in this case and he/she observes the vehicle speed at any given time and responds with a force on either the accelerator or brake pedal to bring the vehicle to a desired speed.

2.4.7. Brake System

The brake system takes an input of vehicle speed and BPP%. The BPP% signal is used to determine the amount of braking force that the driver/PID is intending to apply to the vehicle and distributes this force into a regenerative braking force output and frictional brake output, based on limitation of the motor and systems regenerative power. The vehicle speed input is used to determine if the vehicle speed is above a certain speed threshold needed for regenerative braking to be applied. Figure 2.19 is a detailed description of the vehicle braking system block.

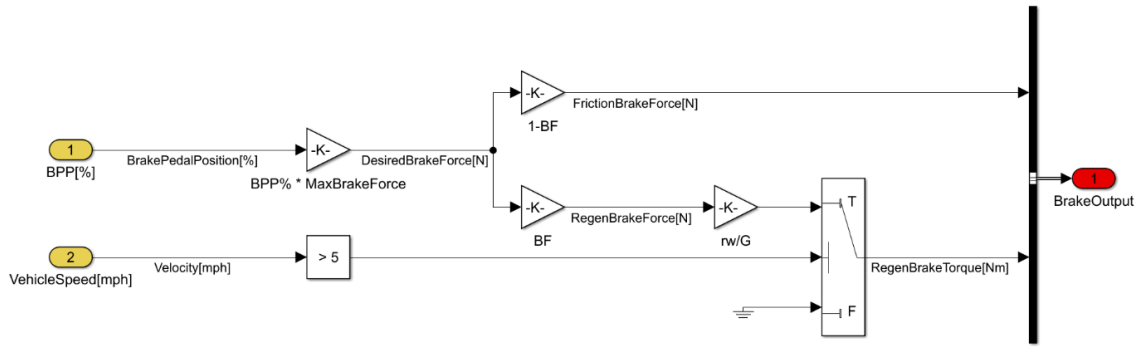


Figure 2.19. Braking System Block [39]

2.4.8. Motor Model

The electric motor model is based on the power loss equation for electric motors described in Figure 2.20, where the motor output power is defined by the motor input power minus the motor losses. Table 2.3 describes the parameters definitions for calculating the motor loss model. The motor model receives an acceleration pedal position signal APP% input and motor speed feedback, these values are then used in the motor torque limiter sub-system described in Figure 2.21 to determine the maximum torque output. Similarly, the regenerative limiter subsystem determines the maximum allowable regenerative torque which is specified by a factor of the maximum allowable torque of the motor. The net torque is then used to calculate the output power using the motor loss model as described by [39]:

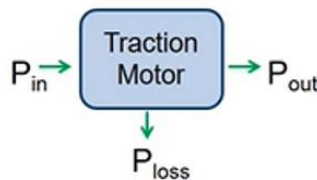


Figure 2.20. Motor loss model [39].

$$P_{mot} = T_{mot} \omega_{mot} \quad (2.12)$$

$$P_{loss} = k_c T^2 + k_i \omega + k_w \omega^3 + C \quad (2.13)$$

$$P_{in} = \tau \cdot \omega + P_{loss} \quad (2.14)$$

Table 2.3. Motor Model Parameters [39].

Parameter	Units	Description	Value
T	Nm	Maximum motor torque	450
ω	rad / s	Motor base speed	834
k_c	s	Motor loss constant	0.12
	$Kg m^2$		
k_i	J	Motor loss constant	0.01
k_w	$Kg m^2$	Motor loss constant	$1.2 e^{-05}$
C	W	Motor loss constant	600

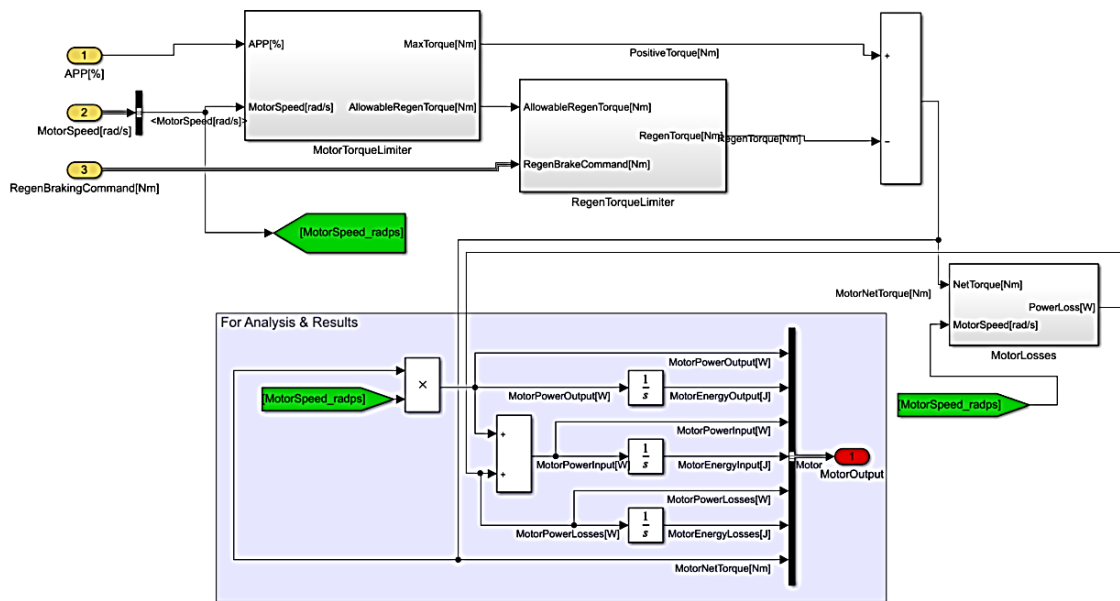


Figure 2.21. Electric Motor Model with motor loss model calculations [39].

2.4.9. Battery Model

The battery model is developed based on a constant voltage source, V_{oc} , in series with an internal resistance, R_{int} , as described by Figure 2.22. This model is much more simplified compared to the equivalent circuit model described in Chapter Three of this work and does not consider battery chemistry. It relies on a power loss calculation to determine the battery output current as described by the following equations and Table 2.4:

$$P_{ideal} = P_{actual} + P_{loss} \quad (2.15)$$

$$P_{ideal} = IV_{oc} \quad (2.16)$$

$$P_{actual} = IV_{oc} - I^2R_{int} \quad (2.17)$$

$$P_{loss} = I^2R_{int} \quad (2.18)$$

Table 2.4. Battery Model Parameters [54]

Parameter	Units	Description
<i>I</i>	<i>Amps</i>	Current
<i>V</i>	<i>Volts</i>	Voltage
<i>P</i>	<i>Watts</i>	Power
<i>R_{int}</i>	Ω	Internal resistance
<i>E</i>	<i>Joules</i>	Energy
<i>SOC</i>	%	State of charge

Figure 2.23 describes the battery model and loss model calculation in the Simulink EV model [54]. The state of charge (SOC) of the battery is determined by

integrating the power over time and comparing to the energy capacity variable set at the initialization of the simulation.

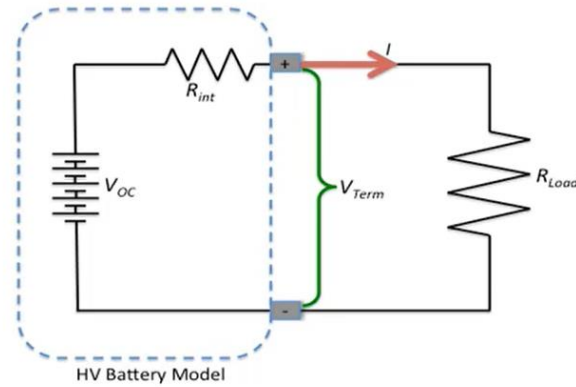


Figure 2.22. Battery Model with Internal Resistance [39].

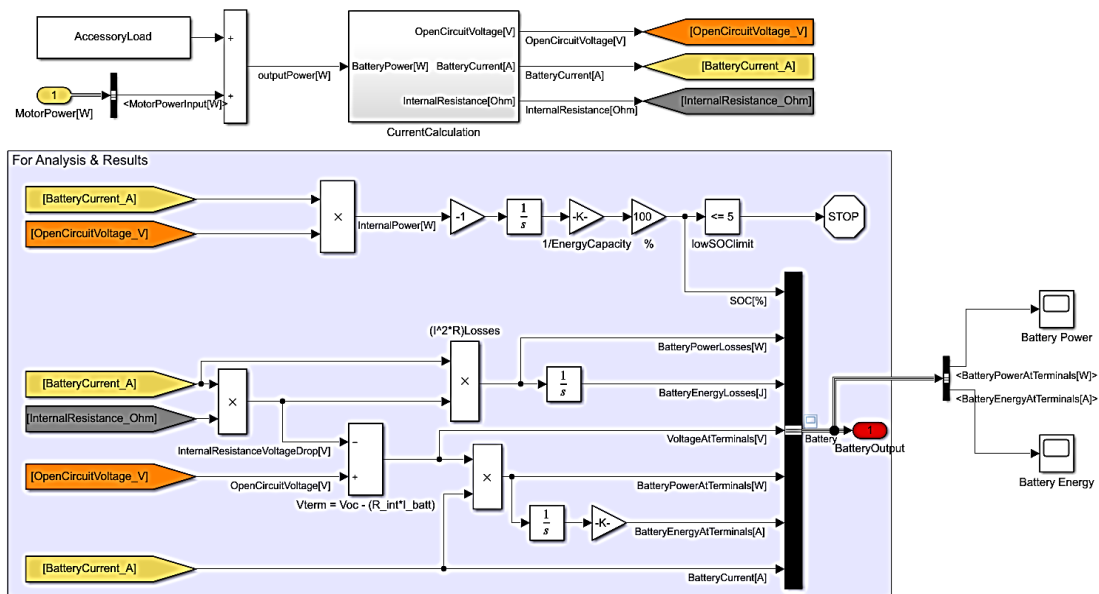


Figure 2.23. Battery Model with SOC and Power Loss Calculations [39].

2.5. Electric Vehicle Chassis Dynamometer Testing

EVs are characterized on a chassis dynamometer to determine their driving performance. The vehicle performance testing typically involves driving the vehicle through an EPA drive cycle, such as in Figure 2.13. Prior to dynamometer testing of an EV, the dynamometer must be calibrated to accurately represent the road load forces that are exerted on a vehicle. This involves road load coast down test, where the vehicle is driven on a flat straight road and accelerating the vehicle to ~60 mph, then shifting the vehicle to neutral gear to remove the regenerative braking capabilities and then letting the vehicle coast down naturally to determine the road load forces acting on vehicle, which include aerodynamic drag and rolling resistance. One such test was conducted and validated by putting the vehicle through a similar drive cycles on the road and the dynamometer [49], collecting data through the vehicle on-board diagnostic (OBD) port and then comparing the power and energy of the vehicle over the drive cycles. Figure 2.25 is a speed plot of the road and dynamometer tests and the difference in speed between both tests, showing a close correlation between speed over the entire drive cycle. Figure 2.26 is a plot of the power and energy for both the road and dynamometer tests. Although the dynamic behavior of the vehicle during the road and dynamometer tests varied, they followed a similar trend over time and the energy consumption was comparable.

Once the dynamometer was calibrated, the modified MCT test described in Figure 2.13 was conducted on the vehicle on the dynamometer to determine the energy efficiency of the vehicle. Three runs of the same MCT test were carried out on the vehicle and described in Figure 2.27. The power instantaneous and energy of each cycle was recorded during the drive cycles and described in Figure 2.28. Finally, a vehicle

acceleration performance, known as the wide-open throttle (WOT) test, was conducted on the vehicle to determine the vehicle initial acceleration capability described in Figure 2.29. The dynamometer tests resulted in an energy efficiency average of 297 Wh/mile and an initial acceleration of 7.5 seconds from 0 – 60mph (96.44kph).

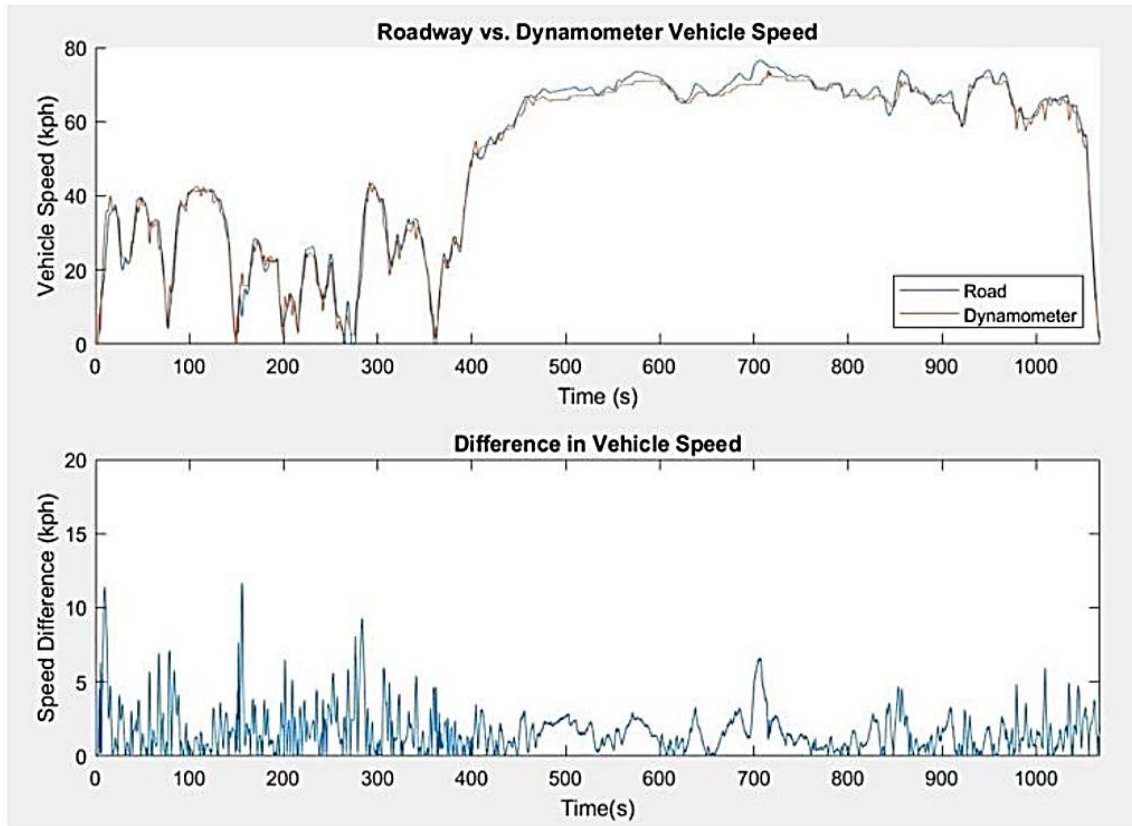


Figure 2.25. Road and dynamometer test vehicle speed and difference [37].

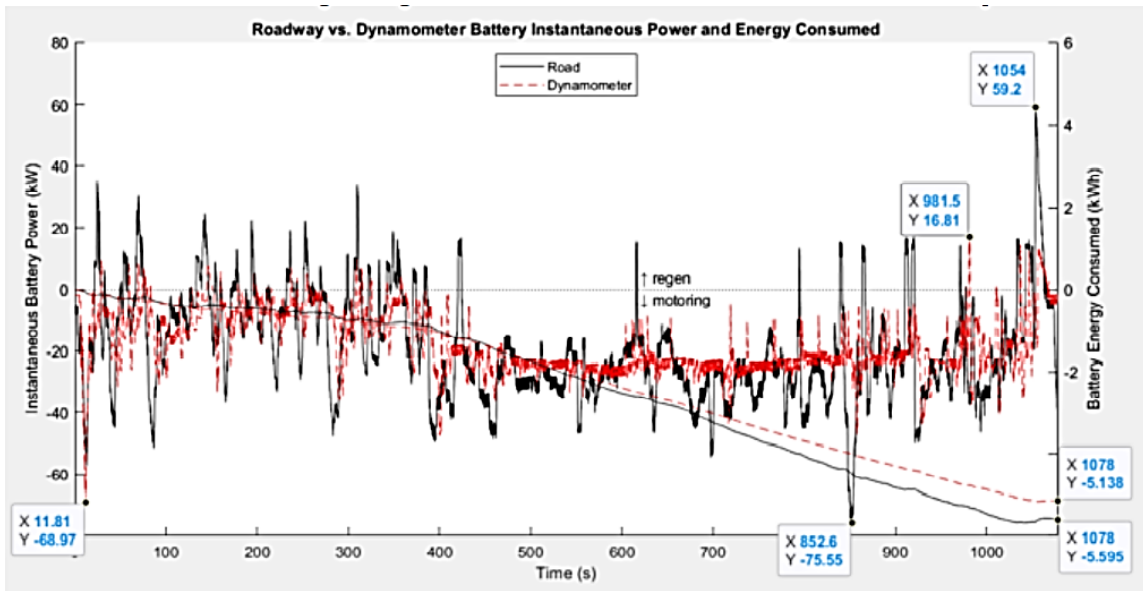


Figure 2.26. Road and dyno test vehicle power (left axis) and energy (right axis) [37].

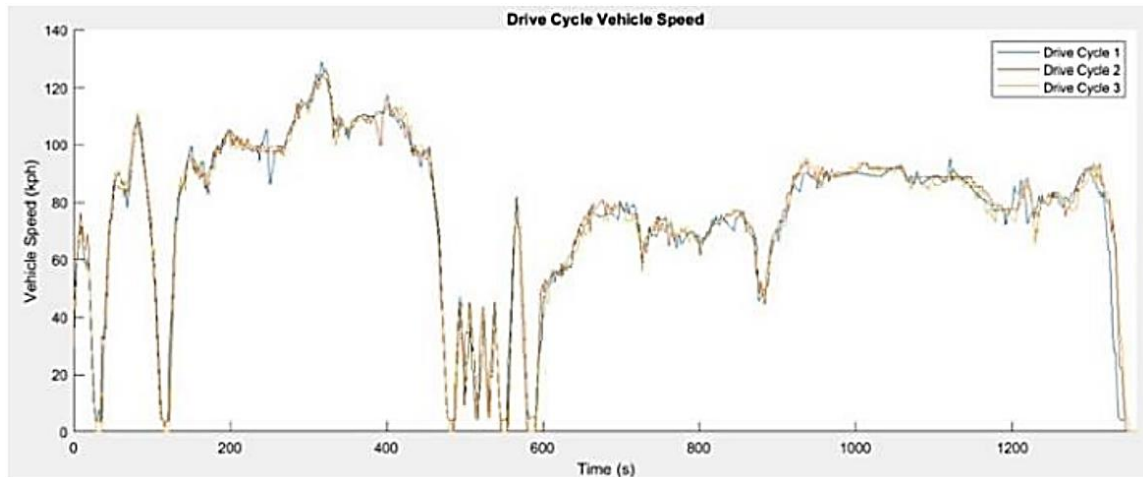


Figure 2.27. MCT drive cycle vehicle speed on chassis dyno [37].

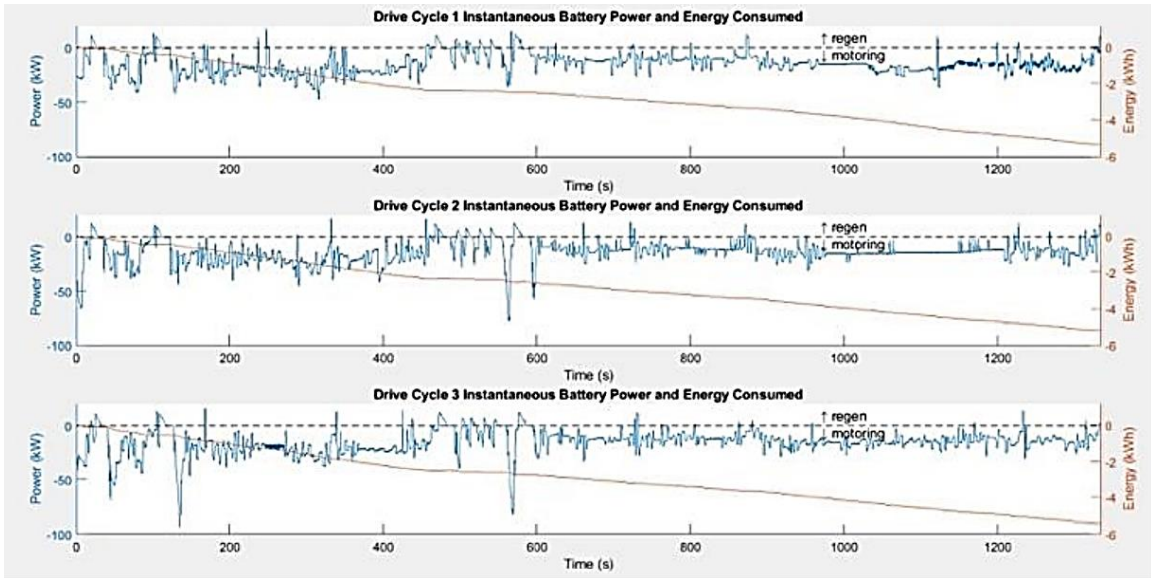
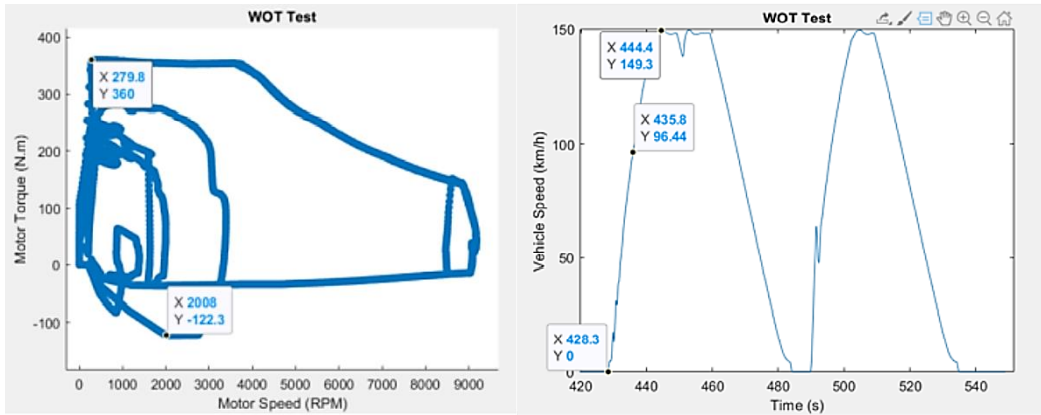


Figure 2.28. MCT drive cycle vehicle power(left axis) and energy (right axis) on chassis dyno [37].



(a)

(b)

Figure 2.29. The WOT Test: (a) Motor torque envelope (b) Vehicle speed [37].

The vehicle top speed was determined to be software limited to 93 mph (149.66 km/h), with a 0–60 mph (96.56 km/h) time of 7.5 secs (advertised 0–60 mph of 6.5 for vehicle under test), peak current of 452.2 A, peak motor torque of 360 Nm and peak axle torque of 2538 Nm. In Summary, the EV chassis dynamometer results serve as a strong

basis for validating the results of a vehicle model developed and simulated within a software environment through an iterative design process. In the real world, road grade plays a significant role on EV motor torque demand, thus small errors in the total load on the vehicle when tested on a dyno compared to real world driving may be observed; however, it is difficult and sometimes unsafe to perform some of the rigorous vehicle driving scenarios needed for testing high performance vehicles on public roads.

2.6. Electric Vehicle Model Simulation Results and Analysis

Given the high repeatability of the chassis dynamometer testing, the EV model developed above was then validated against the dyno work, with careful comparison of the observations, including speed, distance, energy expended and power between modeling, chassis dynamometer, and on-road measurements. It is important to note that due to the advanced dynamics controls on the real vehicle in comparison to the simplified PID controls modeled, the dynamic responses of the modeled vehicle and the real vehicle, such as motor torque and power, are expected to vary to a certain degree. However, the steady state values, such as speed, distance and energy, do show a strong correlation.

Figure 2.30 is a plot of the vehicle speed during the simulation overlaid on the drive cycle speed, which was recorded via the OBD port during dyno testing. From the plot in Figure 2.30, we observe that the modeled vehicle can follow the drive cycle input closely and meets the speed and torque response requirements. Figure 2.31 is a plot of the battery SOC over the drive cycle period. The model was initialized to 95% SOC at the beginning of the model and ended at ~85% at the end of the simulation. Recall from the

vehicle specification in Table 2.1 that the modeled vehicle battery total capacity 53kWh, indicating that ~10% of the battery total capacity was depleted during the drive cycle.

Figure 2.32 is a plot comparison of the battery energy over time between the dyno test and vehicle simulation, which is derived by integrating the battery power over time, as seen in the model calculations in Figure 2.23. Figure 2.33 is plot comparison of the vehicle distance over time, which is an integration of the vehicle speed over time.

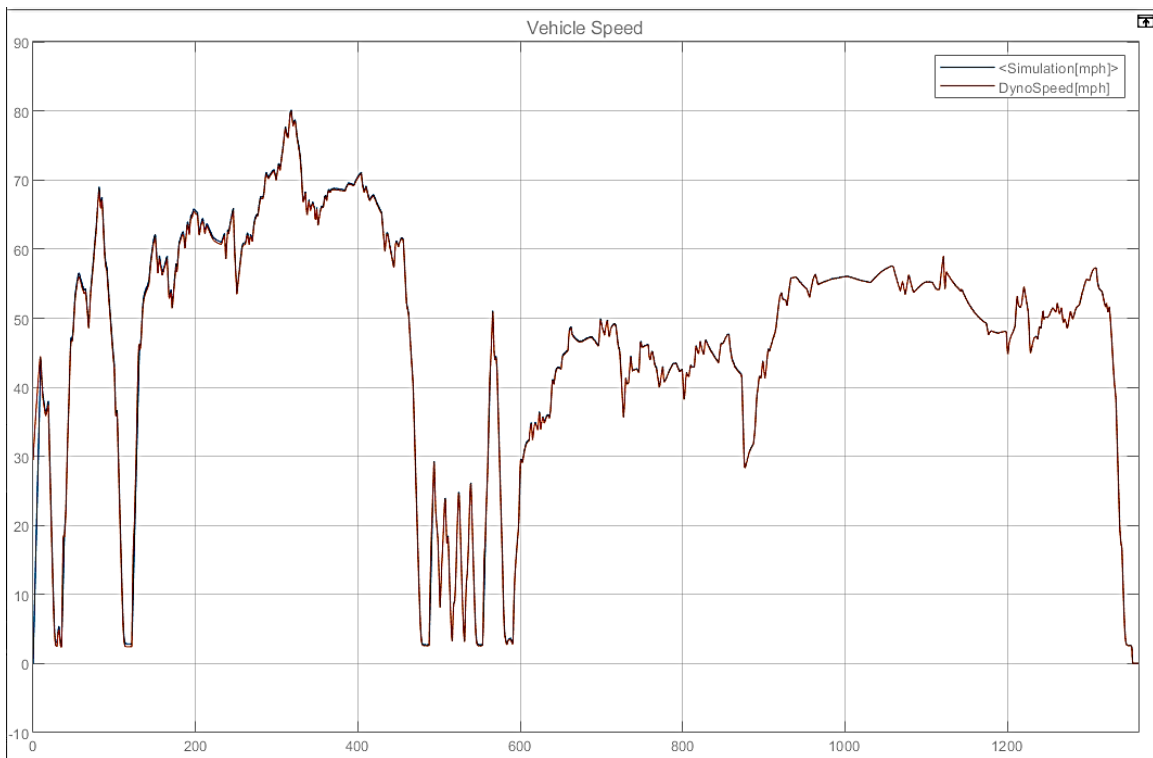


Figure 2.30. Modeled vehicle speed over time compared to dyno speed.

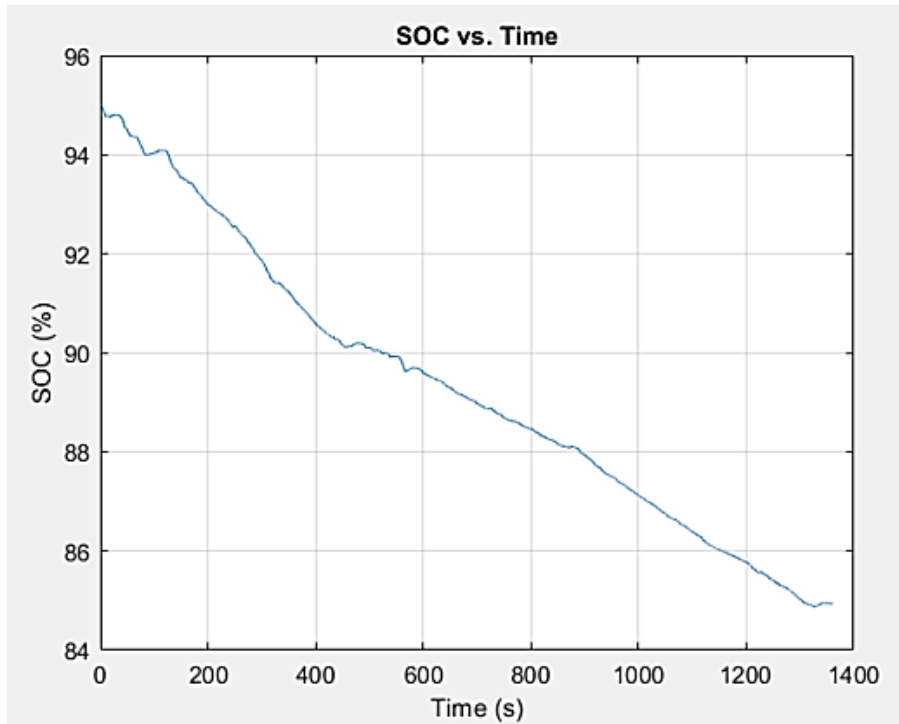


Figure 2.31. Modeled battery State of Charge (SOC) over time.

2.6.1. Energy Efficiency

The energy efficiency of the modeled EV can be derived by dividing the battery energy output by the vehicle distance covered. The total energy delivered by the battery model was 5.299kWh, while the distance travelled was 17.85 miles, having an energy efficiency of 292Wh/mile compared to the dynamometer tests results, which had an energy efficiency average of 297 Wh/mile.

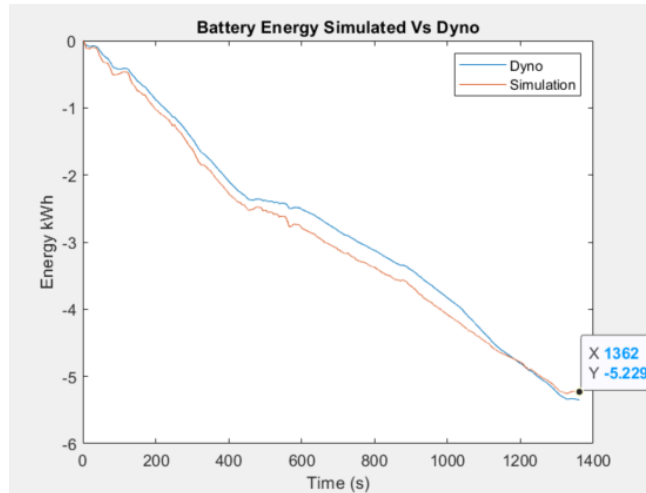


Figure 2.32. Battery energy over time.

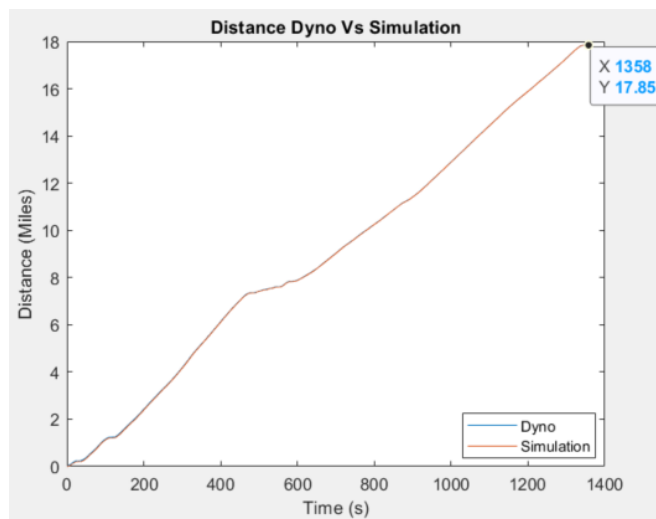


Figure 2.33. Vehicle distance covered over time.

2.6.2. Motor Torque and Power

Figure 2.34 is a plot of the vehicle power over the vehicle speed range, indicating the power regions the motor operated over the drive cycle. From the plot, we can determine the vehicle model rated speed is around 40 mph, and then, between 40 mph to 70 mph, the vehicle is in the constant power region, with a concentration of motor

operating points in this region. The diagonal dotted line that ramps up from 0kW – 150kW in the power plot is attributed to the initial acceleration of the vehicle from 0mph to ~40mph at the very beginning of the drive cycle and towards the 600 second mark. Figure 2.35 is a scatter plot of motor torque over the vehicle speed change from the simulated drive cycle and the dyno test. From these plots, we draw similarities between the two plots, where the maximum torque (simulation) and the peak torque (dyno) occur between 0 and 40mph speed range, the constant torque region, and then the gradual ramp down in torque as the speed increases. Similar to the observations in Figure 2.34, there is a concentration in operating point between 40mph to 70mph in both plots, which is consistent with the drive cycle speeds in Figure 2.30. There is however a significant difference in the dynamic behavior of the dyno motor torque compared to the simulation that can be attributed to the sophisticated motor control schemes implemented in the real vehicle compared to the simple PID controller that is modeled. These sophisticated controls are implemented in the real-world vehicle to allow for ease of drivability and responsiveness of the vehicle under test. For example, in the dyno torque plots, we always observed a continuity in the torque values without sudden jumps or drops in torque value as speed changes compared to the simulated torque-speed plots. This is due to the effective and careful avoidance of torque ripples by motor controller implemented on the real-world vehicle. The simulated vehicle model's torque controls simply calculate the maximum torque based on current vehicle speed and the requested APP% at each time step. A more advanced model will take into consideration the dynamic response of the vehicle and simulate a smoother transition in torque applied, similar to the dyno vehicle response. The expected torque envelope regions of the torque plots capture the

expected torque-speed envelope however, showing an attainment of maximum traction and regenerative torque at lower speeds and reduced torque at higher speeds, as indicated in the torque over time plots in Figure 2.36 as well.

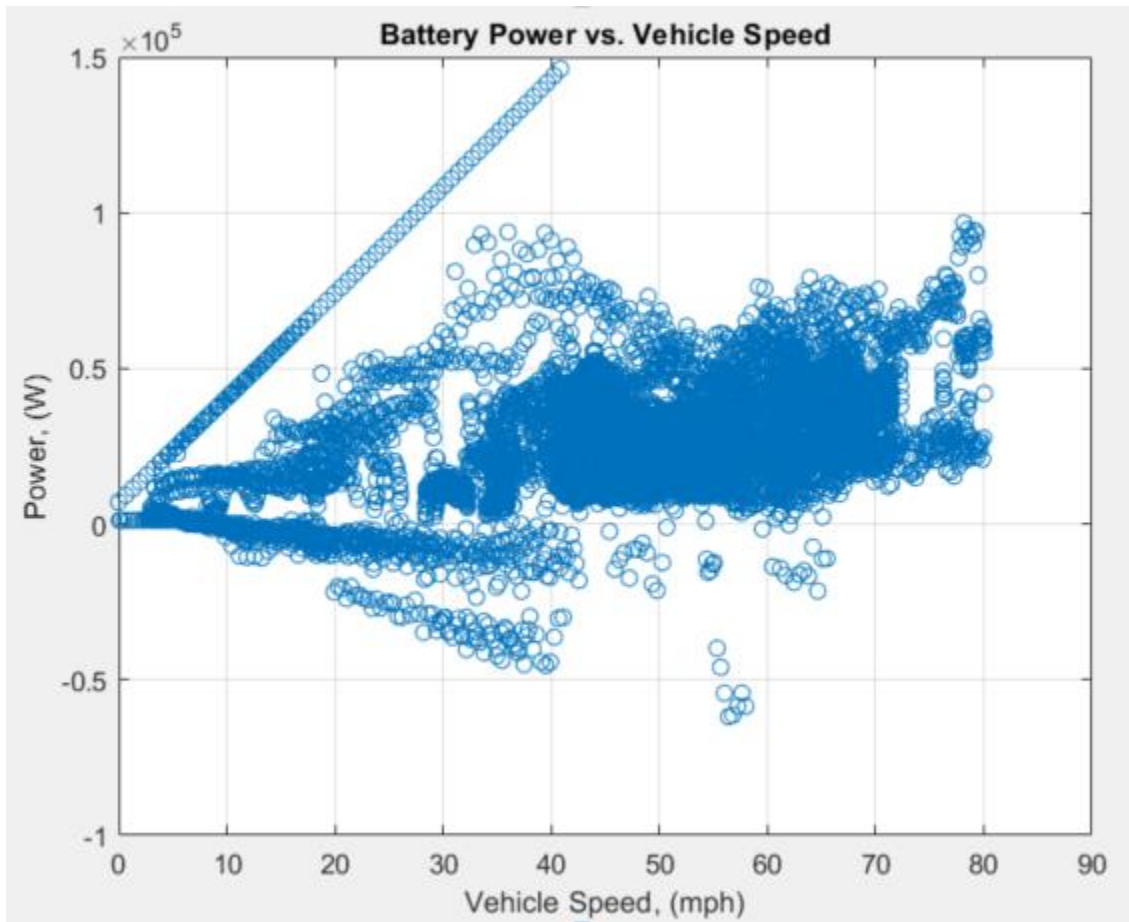
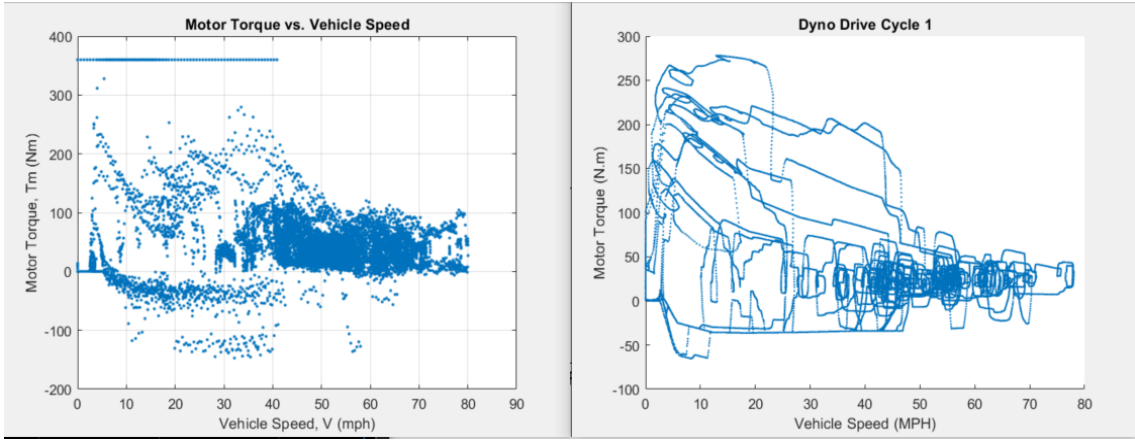


Figure 2.34. Motor power over speed.



(a)

(b)

Figure 2.35. Motor torque over speed: (a) Simulation (b) Dyno Test.

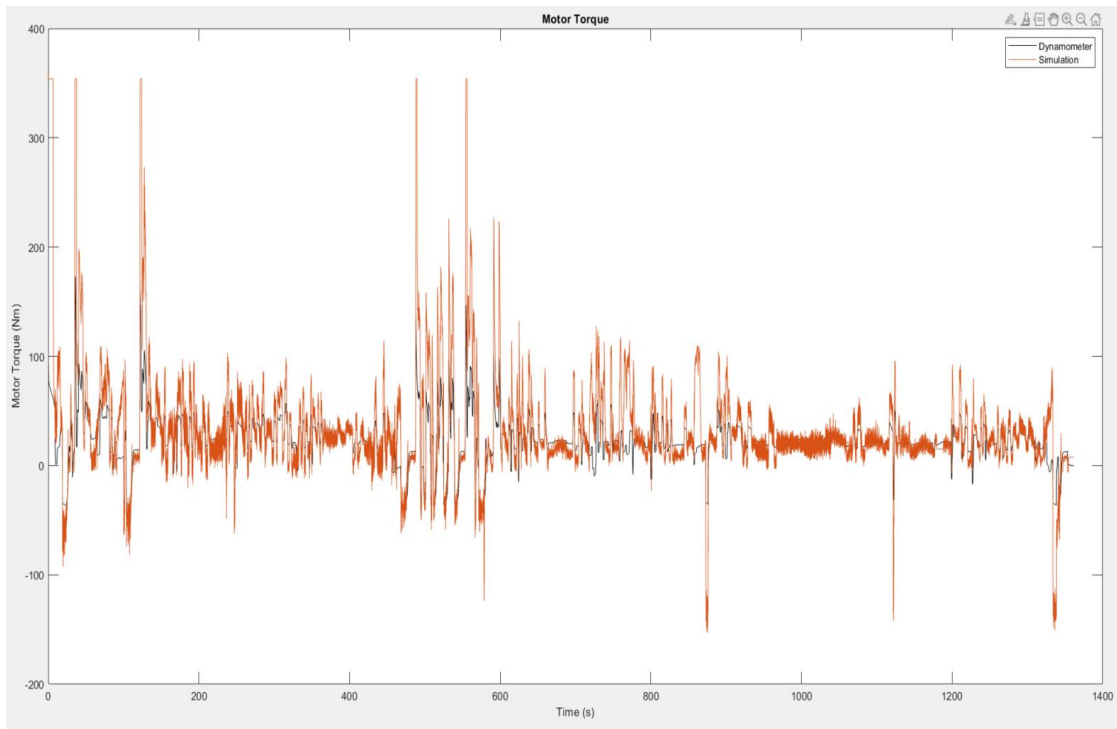


Figure 2.36. Motor torque over time plot.

2.6.3. Loss Model

Determining the energy losses in the model provides insight to where energy efficiency can be increased within the overall system. The total tractive energy consumption of the vehicle over the drive cycle is measured at 3.18 kWh as indicated in Figure 2.37, while the motor energy losses are measured at 0.71 kWh as indicated in Figure 2.38, and the driveline losses are measured at 0.5 kWh, indicating that the total energy used to overcome the road load forces acting on the vehicle, F_{RL} , is 0.839 kWh. Although Figure 2.32 validated the total energy consumption correlation of the model to the dyno, the figures mentioned above allow us to estimate, experiment and validate the efficiency of the real-world vehicle compared to the vehicle model. The vehicle model can be optimized iteratively to reduce these losses through either reduction in motor losses by adjusting the motors operational limits or modifying the driveline gear selection.

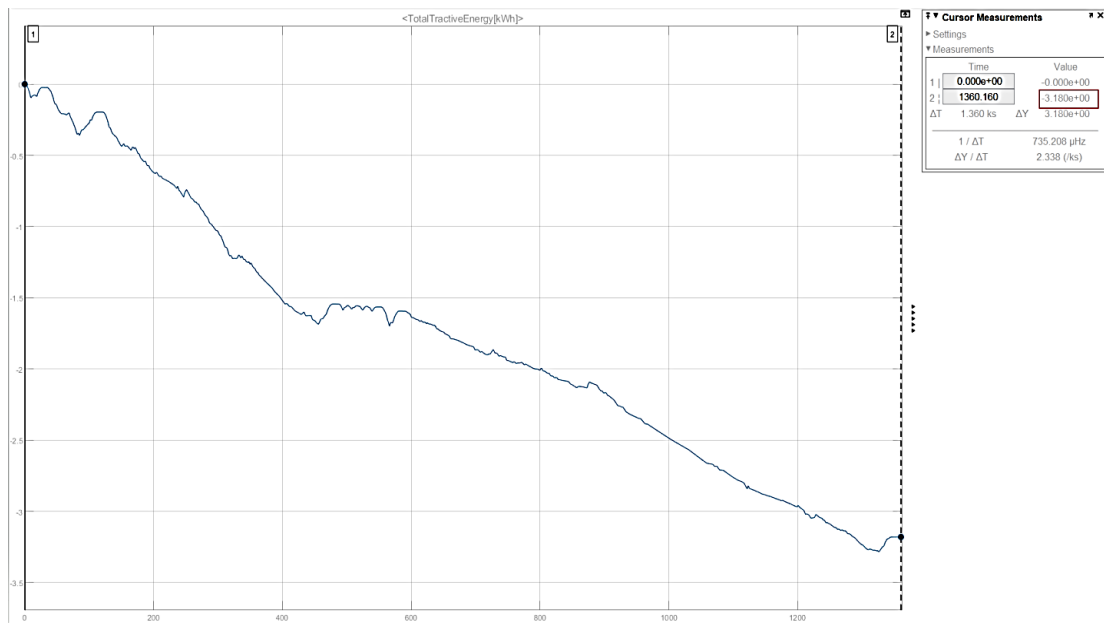


Figure 2.37. Vehicle tractive energy over time.

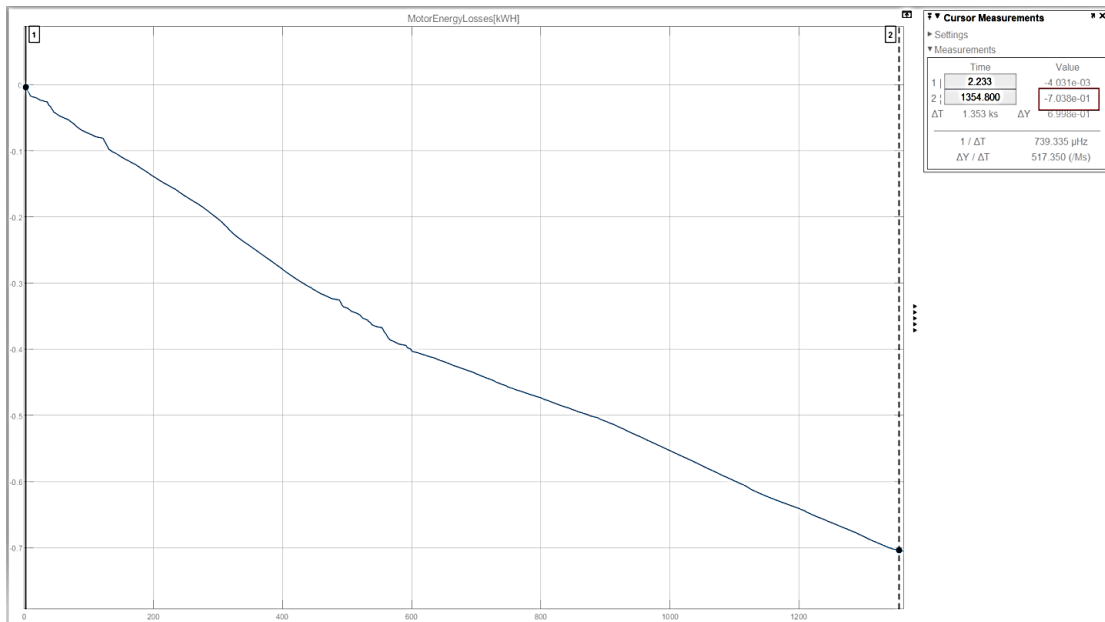


Figure 2.38. Motor energy losses over time.

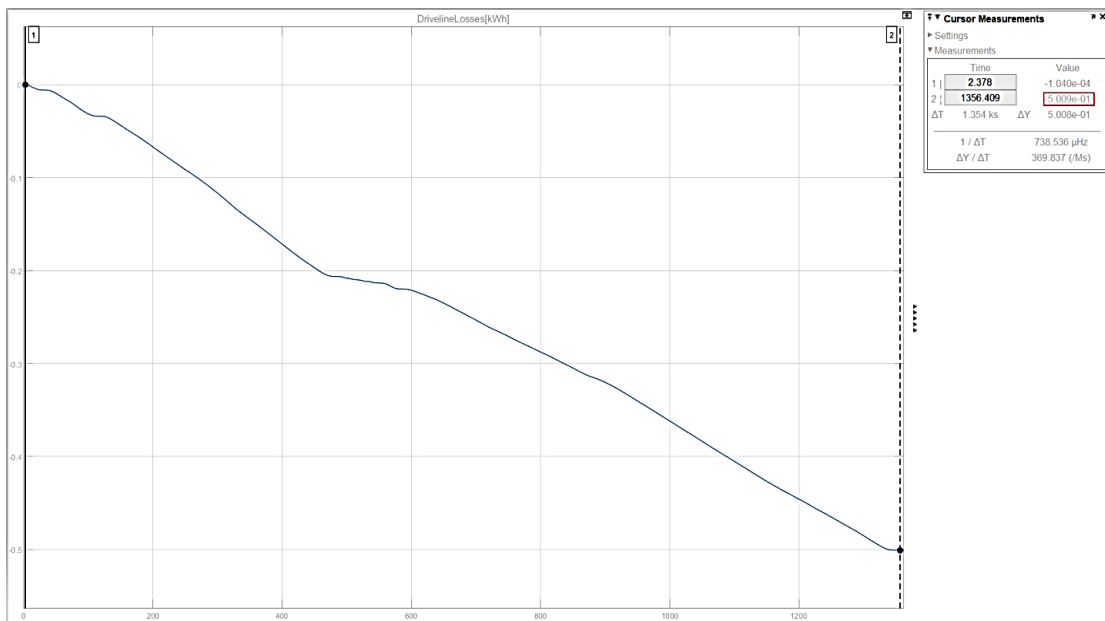


Figure 2.39. Driveline energy losses over time.

The energy efficiency results of the modeled high performance EV compared to the real-world vehicle showed close correlation with a root-mean-square error (RMSE)

value of 0.2. The vehicle speed and vehicle distance traveled of the model also resulted in negligible error values. The modeled motor control strategies, however, did not capture the dynamic and transient behavior of the real-world vehicle adequately. Although the equation-based model provided a valuable means of gaining an understanding of the how the modeled vehicle will perform under certain driving conditions from an energy efficiency standpoint, this modeling approach is not suitable for detailed analysis of vehicle dynamics and evaluation of control strategies.

2.7. Battery Swappable Electric Vehicle Powertrain Prototype Design

In this section, the details of an EV powertrain design prototype are described. The powertrain is designed onboard an existing Chevrolet Tahoe frame which has been converted to a fully EV. The battery packs on-board the E-Tahoe are designed to be completely swappable. Figure 2.40 shows a computer aided drawing (CAD) of the fully electric Tahoe chassis and physical prototype of the vehicle under development. The Chevrolet Tahoe chassis frame was selected for the prototype test bed platform, due to its ladder frame structure which allows for the implementation of a modular battery pack platform. Compared to “unibody” vehicle architecture or the “unified body” architecture where the body of the vehicle and the chassis are one and the same, the ladder frame architecture separates the body of the vehicle from the chassis of the vehicle that holds the powertrain components and suspension. The modularity between the ladder frame and body components, complements the accessibility and ease of swap-ability of the desired EV powertrain prototype.

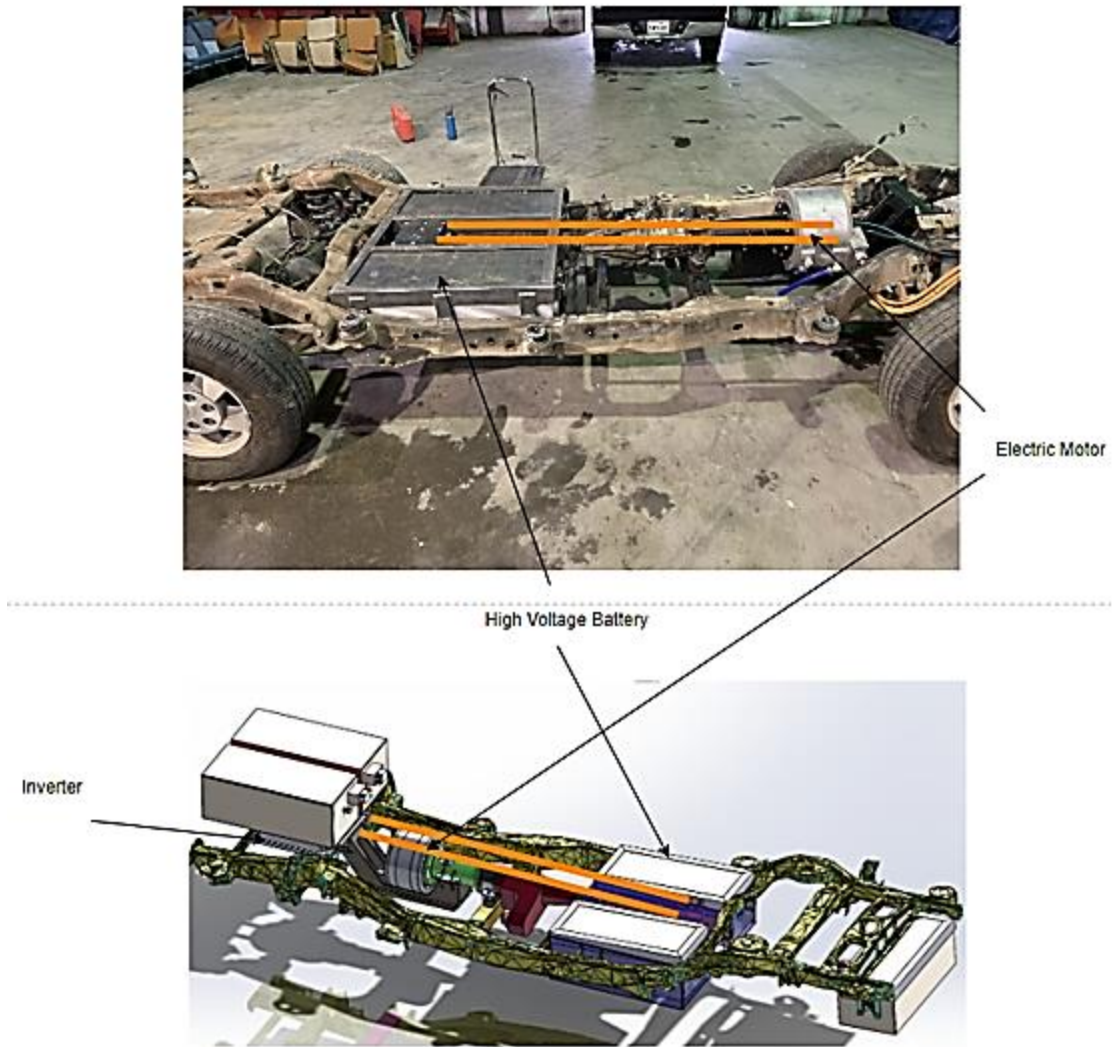


Figure 2.40. Battery Swappable Electric Vehicle Powertrain Chassis Prototype.

2.7.1. Mechanical Design

The mechanical components of the EV consist of rotating parts on the vehicle and are responsible for the translational motion of the vehicle body. Figure 2.41 is a MATLAB/Simulink Simscape model of the mechanical components of an EV consisting of the vehicle body itself, represented by the red block, which is propelled by the left and right tires that are mechanically linked to a rear differential through a gearbox. The gearbox receives rotational inertia in the form of torque from the electric motor which is

used by the differential and ultimately the right and left tires to propel the vehicle forward.

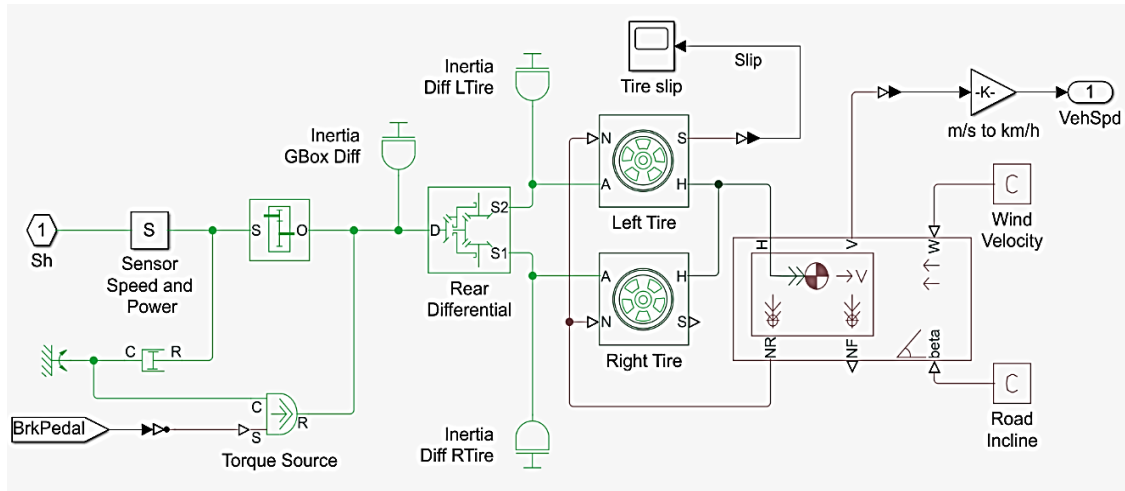


Figure 2.41. MATLAB/Simulink Model of Electric Vehicle Dynamics.

For this research, a novel EV mechanical powertrain is designed consisting of a UQM (motor manufacturer) PP220 motor with 250 hp and 500 Nm of torque, a GM np246 4WD transfer case with a gear ratio of 2.72:1, and stock front and rear differentials with an axle ratio of 3.73:1. This system equates to a 10.14:1 ratio when in direct drive, delivering an impressive 5070 Nm of torque to the wheels at 0 rpm. Figure 2.41 is a detailed CAD model of electric motor and driveline components. It can be observed that the electric motor is mounted to the vehicle with a tripod configuration, given the two mounts behind the electric motor and the mount in front of the motor, where the motor shaft housing mates with the transfer case. The mounts are supported with rubber bushings to allow for absorbing torque vibrations of the motor during operation. The motor and transfer case are linked mechanically through a custom shaft with an internal

spline on the motor side (female end) and an external spline on the transfer case side (male end).

Figures 2.42 are isometric and top views of the EV powertrain prototype. The motor mount weldment **1** cradles the electric motor **2** and is bolted to the motor adapter **3**, by four bolts, with two bolts on each side. The motor mount assembly is bolted to the transfer case **4** through the transfer case adapter **12**. Two drive shafts are attached to the transfer case pointing in opposite directions and can be linked to a differential in the rear and front of the vehicle. The half shaft **5**, which links to the front wheel differential, is shown in Figure 2.42. A rubber bushing **11** is placed in between the motor mount assemble mounting points **7-9** and the vehicle frame **10** to absorb the vibration and noise that results from the torque of the motor during operation. Figure 2.43 shows a cross-section of the motor mount weldment, motor, transfer case, drive shaft, motor adapter, transfer case adapter and transfer case. Figure 2.44 shows the locations of the three mounting points of the motor mount assemble to the vehicle frame, also called a “tripod” mount architecture. Finally, the front and rear differentials are connected to the transfer case through the main drive shaft and the half shaft, respectively.

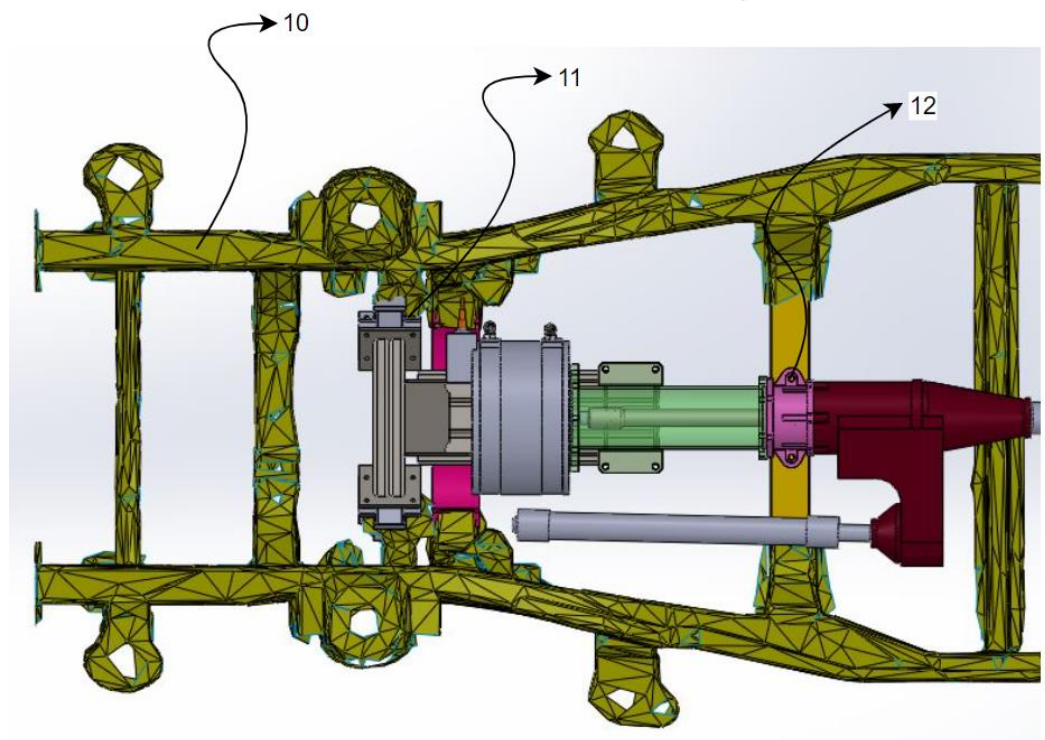
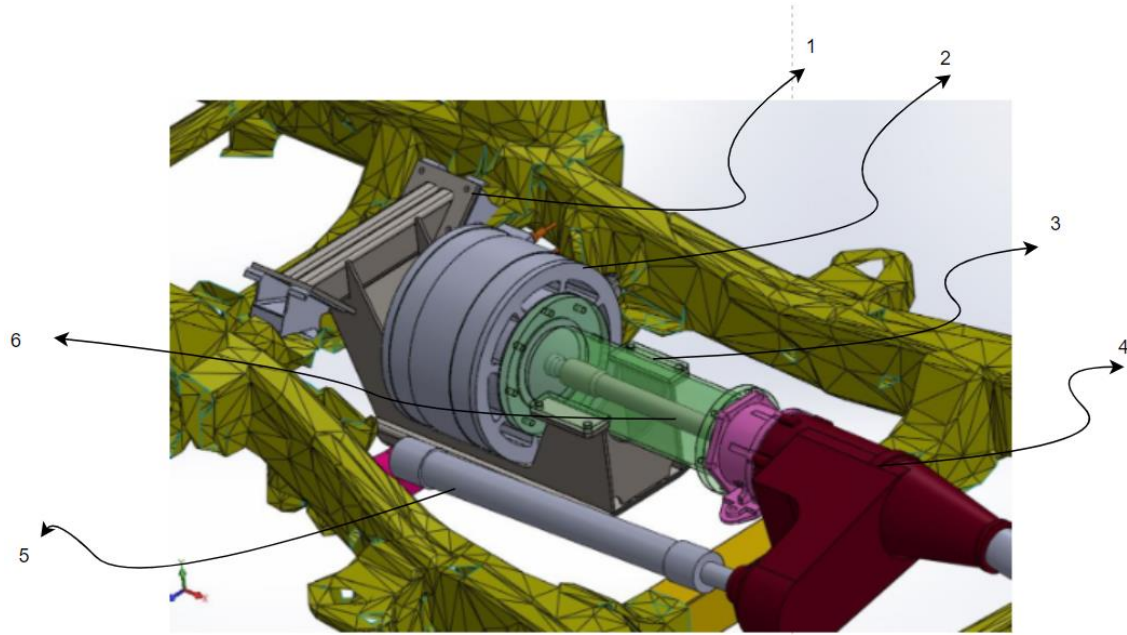


Figure 2.42. Isometric and Top view of vehicle powertrain mechanical design.

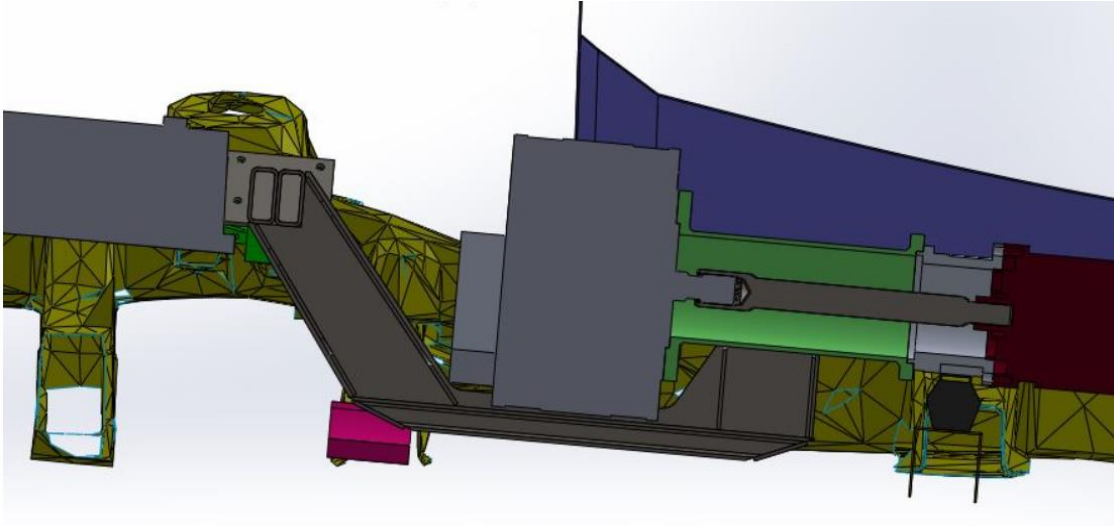


Figure 2.43. Cross section of vehicle powertrain mechanical design.

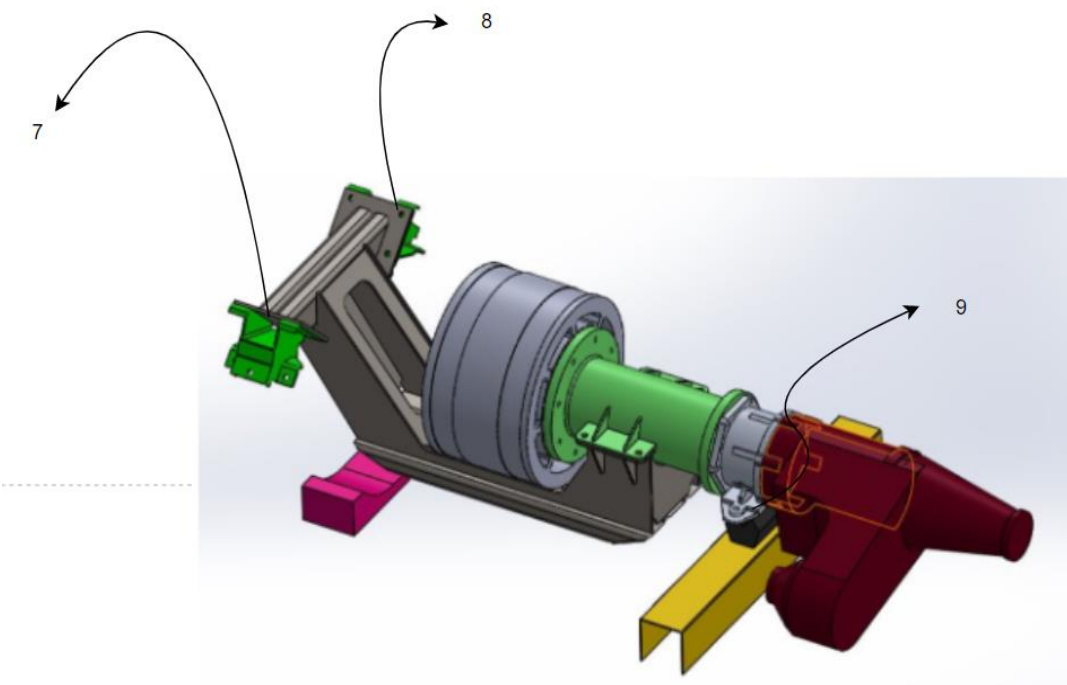


Figure 2.44. Electric drivetrain tripod mount locations.

2.7.2. Structural Design

An EV's battery pack integration into the vehicle chassis is critical to the structural integrity of the vehicle. In this work, a novel method of integrating a distributed

modular battery pack into a vehicle is designed and validated. Individual battery pack modules are housed inside of a battery pack assembly described in Figure 2.45 where **3** is the battery pack lid, **5** is the electrical connector, **2** is the battery module and **1** is the battery pack enclosure. The battery pack assembly also includes the housing for a wireless BMS for monitoring, protection and balancing of cells, an aluminum cold plate for extracting heat from a battery pack through convection heat transfer, hoses and quick disconnect valves for inflow and outflow of coolant to the chill plates, and HV connectors for connecting the individual battery modules within the pack and the entire pack to other packs in the distributed battery network. The unique design of the battery packs in this distributed modular format is a novel approach to battery pack integration into a vehicle chassis. It allows the battery pack to still be a structural part of the vehicle while allowing for flexibility of the powertrain to still be 4WD with a single motor, and for individual modular packs to be swapped from the vehicle easily, one at a time during a manual swap, or all at once during an automatic swap. A complementary structural component of this vehicle design is the battery collection frame, pictured in Figures 2.46 and 2.47, which is a structural frame that can be welded or bolted to the main vehicle chassis. The collection frame contains the battery latches to which the kingpins on the battery box attach. The latches on the battery collection frame force the battery pack assembly and all its connections to be aligned as the battery packs are inserted into the vehicle chassis.

Figure 2.48 is a detailed description of the battery pack latch assembly with an isometric, front and cross-sectional view. It features a spring-loaded cam that locks the battery pack in place when upward pressure is applied and a spring-loaded latch release

handle. The cross-section **72** is taken along section C-C, **49** represents the latch frame, **58** represents a handle bar for disengaging the latch, **59** represents the kingpin latch, **52** represents the latch cam, **51** represent the cam bushing, **70** represents the cam bushing, **57** represents the lock slide, **64** represents the compression springs for the latch release, **54** represents the spring pin, **53** represents the compression springs for the spring pin, **71** represent application of Loctite, **61** represents a flat washer, **56** is an oversized flat washer, and **55** is a self-locking hex nut. The following chapter discusses more in the design of the modular battery packs, the swapping methodology and novel concepts of modular battery packs and battery pack closed-loop cooling systems.

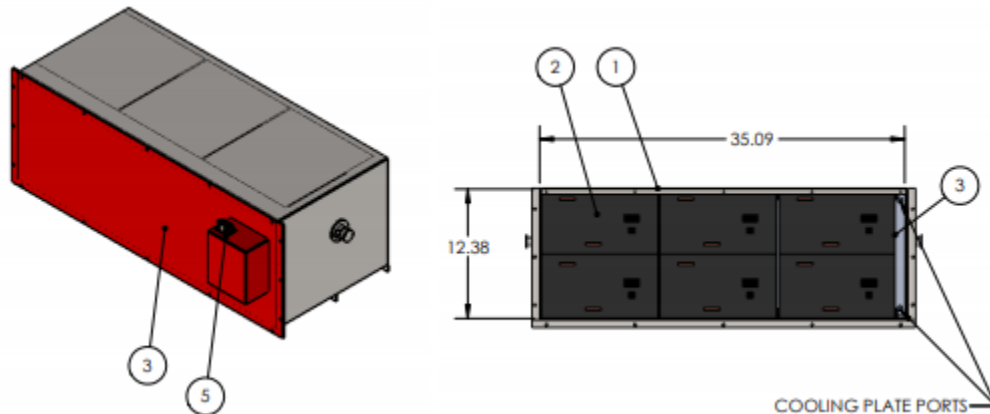


Figure 2.45. Battery Pack Assembly.

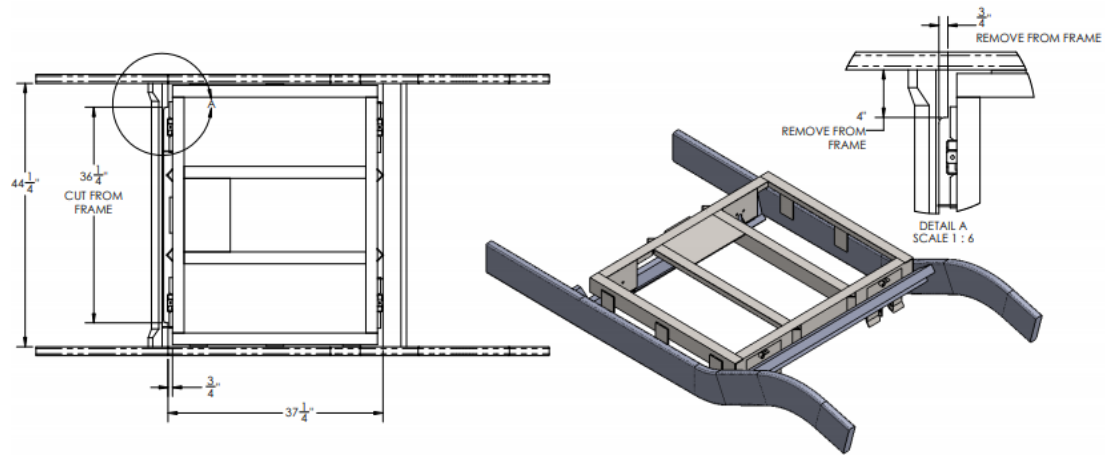


Figure 2.46. Battery Pack Collection Frame Detail.

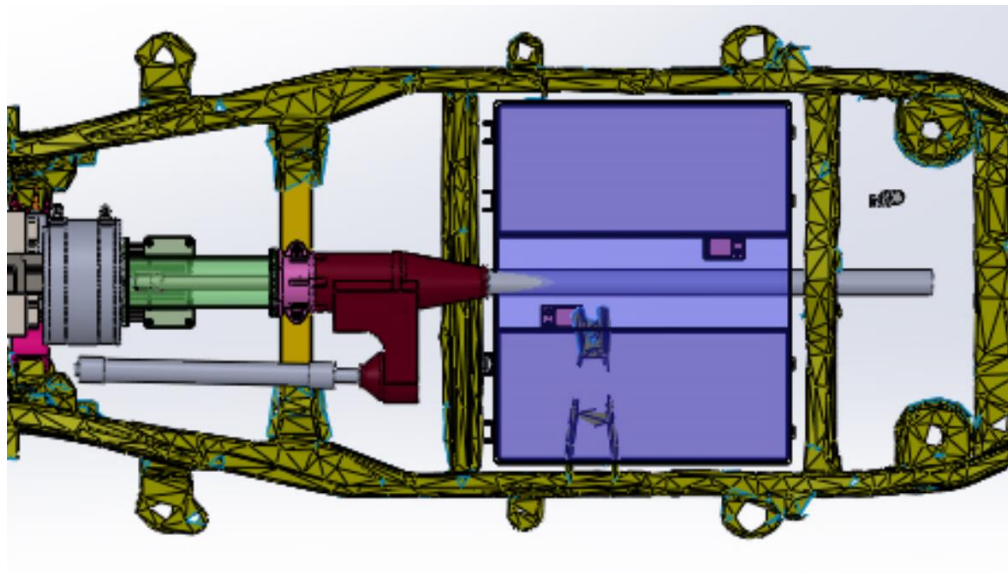


Figure 2.47. Battery Pack Collection Frame Top View.

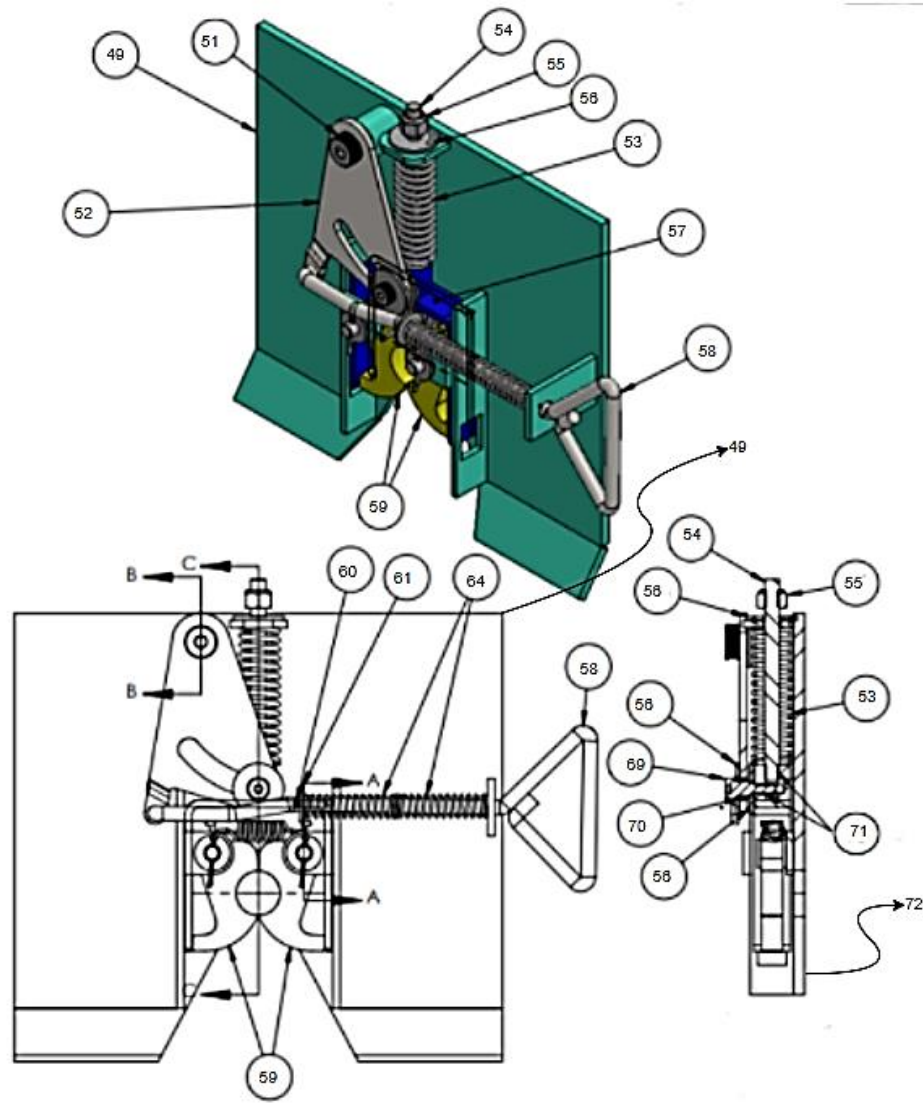


Figure 2.48. Battery Pack Latch Assembly.

2.7.3. Electrical Design

Figure 2.49 is the system overview of the UQM motor and controller system which converts HV DC battery voltage into torque as an input [57]. The vehicle input block is responsible for providing the control signals to the vehicle control unit (VCU), which then commands the UQM inverter controller via CAN controls. For this vehicle

prototype, a Thunderstruck Motors Vehicle Control Unit (VCU) was implemented, described in Figure 2.50. The complete vehicle control unit system also includes the following system components:

- 12V Power, normally connected to an EV accessory battery through the key switch
- CAN, used to communicate between the VCU and Inverter
- Throttle, which connects to a Hall or resistive throttle and determines the requested
- Precharge Control to enable a precharge relay
- Contactor Control to enable the main contactor
- Forward/Reverse (or Forward/Reverse/Neutral) input, to determine the direction of motor rotation
- Brake Switch, to request regeneration when the brake is applied Brake Pressure Transducer, which can request variable amount of regeneration depending on brake pedal pressure
- Brake Light output to turn the brake light on when there is braking regeneration. torque

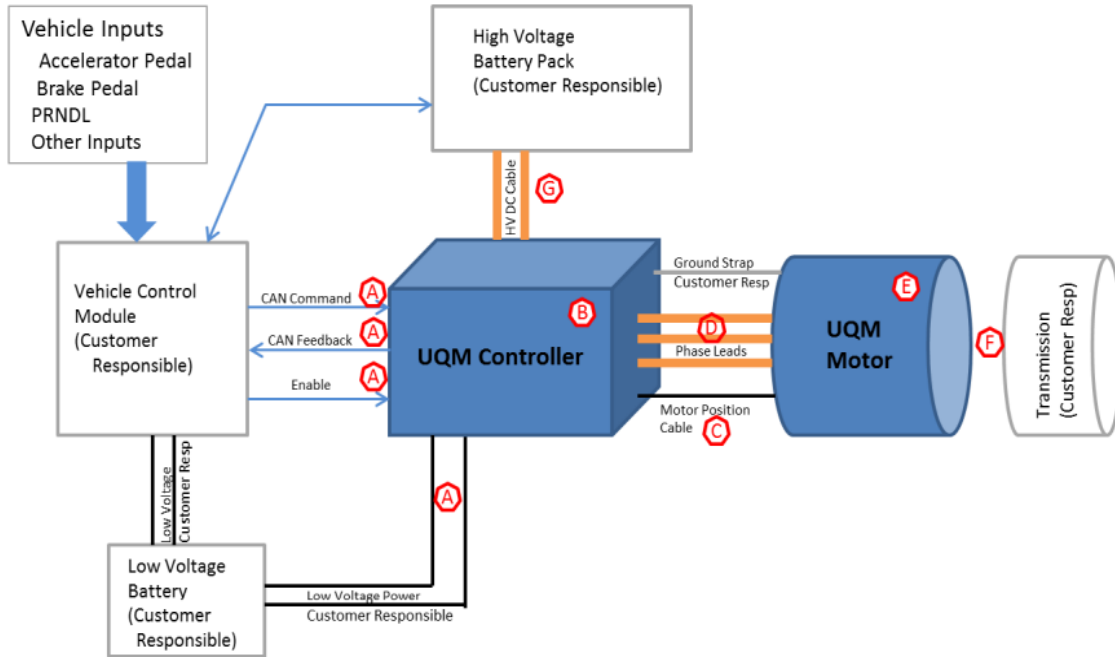


Figure 2.49. The UQM motor system block diagram [46].

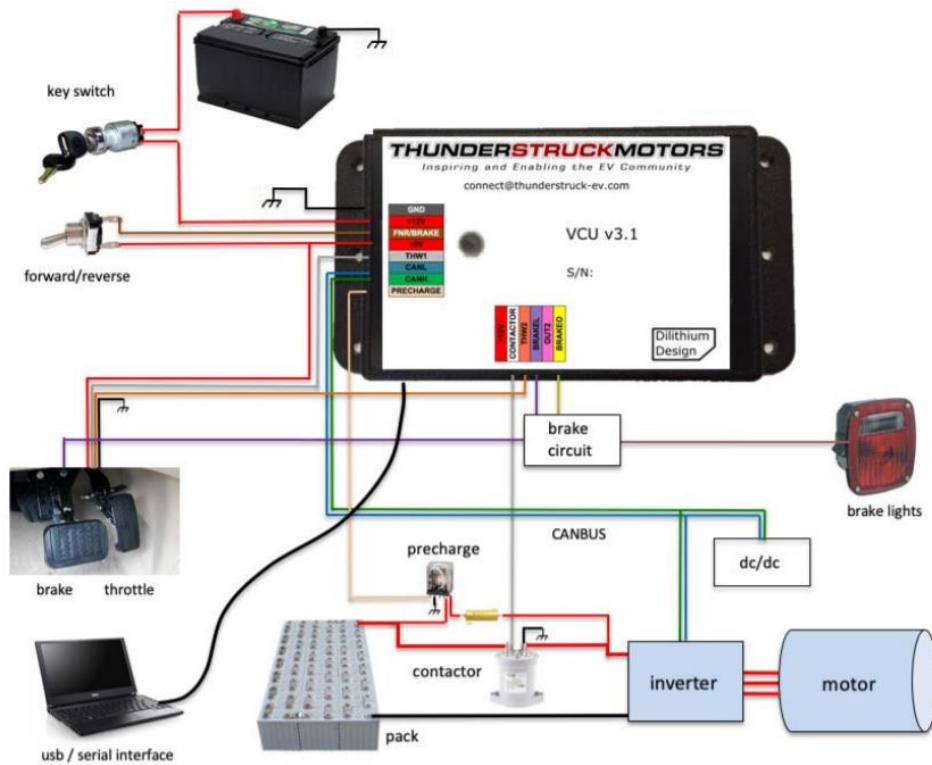


Figure 2.50. Thunderstruck motors VCU system block diagram [47].

2.7.4. Thermal Management System for Motor and Inverter.

The thermal management system for the UQM motor system is described in Figure 2.51. The coolant loop consisted of 50/50 water/ethylene glycol mix. Maximum temperature for inverter/motor is 60 °C and minimum flow rate is 10 L/min, which met the electric pump requirements, detailed in Table 2.5.

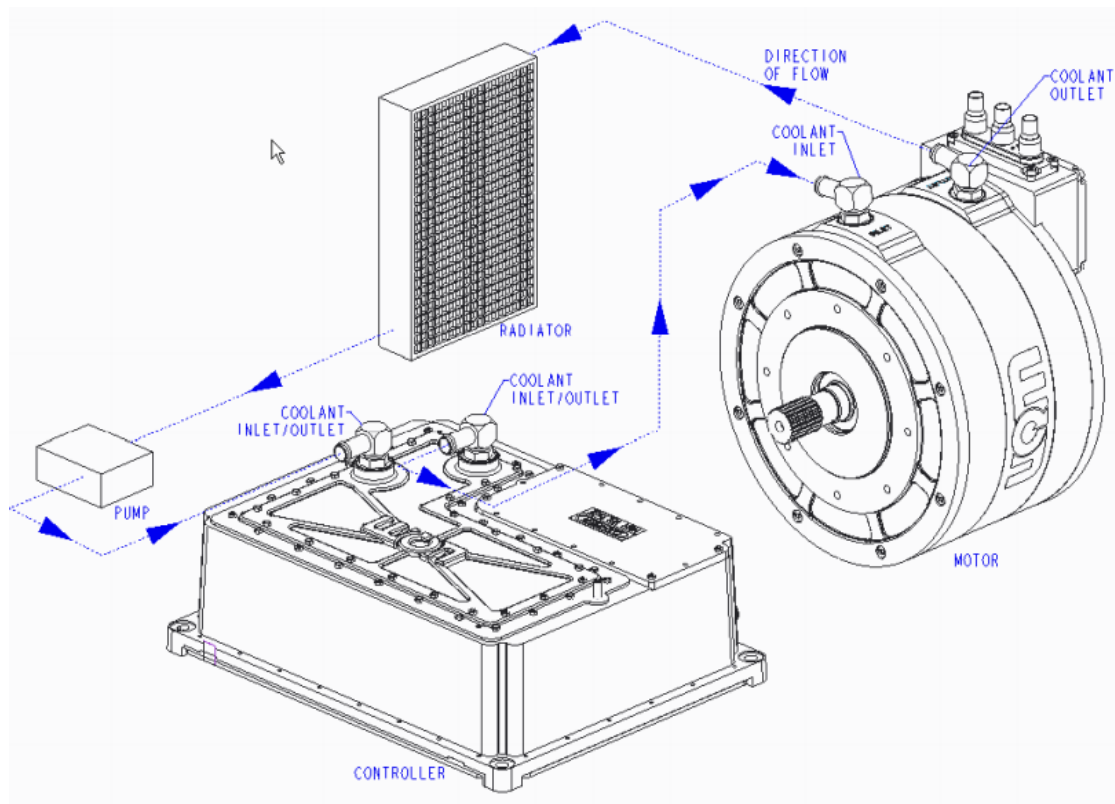


Figure 2.51. E-Tahoe thermal management system design [46].

Table 2.5. Drivetrain cooling requirements [46].

Requirement	Specification
Coolant Type	50/50 water to glycol
Maximum Inlet Coolant Temperature (full performance)	60° C
Minimum Coolant Flow Rate	10 liters per minute (LPM)

CHAPTER THREE

Battery Management System and Health Estimation

3.1. Introduction

This chapter presents technical details of developing a framework for EV battery and BMS modeling for a variety of usage conditions and applications. It also presents details for the accurate estimation of battery state of health (SOH), a vehicle parameter critical to the safety and life of an EV. The EV battery primarily provides propulsion power for the vehicle while also providing auxiliary power to other electrical components of the vehicle, such as the HVAC, power windows, power seats, interior and exterior lights and so on. The safety, performance, and operability of the EV are heavily reliant on the health and life of the battery. The cost of replacing the EV battery could also be significantly high, sometimes up to 30 – 50% the cost of the entire vehicle. This is primarily due to the cost of the batteries themselves (\$150/kWh for Li-Ion Batteries) [48], but also due to the labor, complexity, logistics and tooling/equipment needed to store, ship and replace heavy packs that could weigh up to one-third of the weight of the entire vehicle.

The future of mobility will be autonomous, electric, and shared, with millions of EVs on the road as often as possible connecting people, delivering goods and providing various services with minimal down time. The e-mobility future will be powered by battery technologies that will provide power to EVs while also providing energy storage backup support and other ancillary services to the grid. To accomplish this daunting task,

it is important to understand and estimate accurately the SOH of batteries in different operating conditions. Characterization of the different factors that affect battery health, both quantitatively and qualitatively, can help engineers design battery controls that improve powertrain performance, increase customer confidence in EV parameter estimations, such as state-of-charge (SOC) and range, and improve fleet management and vehicle serviceability through improved diagnostics and prognosis.

3.2. Background

During the vehicle design stage, EV design engineers design the vehicle from both a performance and durability requirement standpoint. To validate the different design requirements, high fidelity models of the vehicle must be developed that accurately describe the performance, safety, and quality of the vehicle. High fidelity models of the EV battery packs that accurately characterize the battery SOH under different operating conditions is a particularly challenging problem. This is mainly due to the computational complexity of accounting for the number of dynamic and non-uniform physical activities occurring inside of a battery as it is cycled under various duty cycles and conditions.

Typically, at the initial stage of the vehicle design, engineers are limited to battery performance and aging test data that have been retrieved under controlled laboratory conditions and make design conditions based on this data. However, in practice, this data does not accurately depict real-world operating conditions. Poorly designed battery controls and battery state estimations could lead to unexpected battery faults, significant loss in capacity/range, high warranty costs, vehicle recalls and customer dissatisfaction.

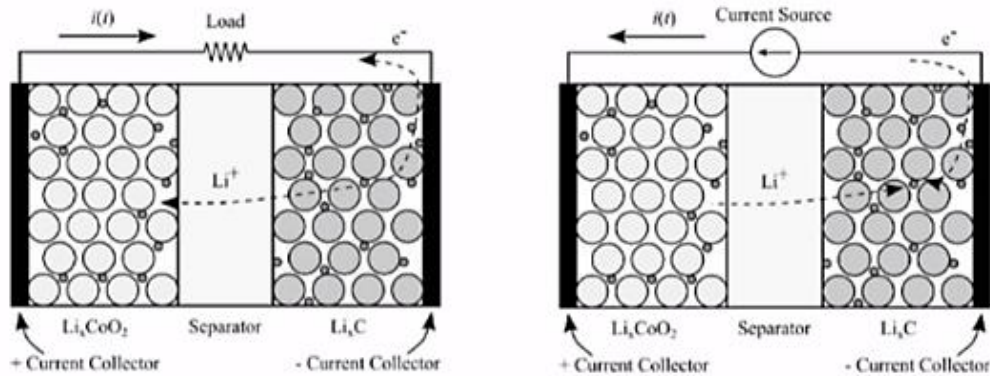
In the following sections of this chapter, a detailed description of Li-ion chemistry, an implementation of battery parametrization and modeling techniques, and a battery management system and battery state estimation and control framework are all described. This framework combines laboratory battery test data with high fidelity data-driven models to perform state estimation and battery aging/life predictions. This will, in turn, improve the vehicle design process by providing vehicle design engineers with more accurate models of the battery packs while also improving diagnostics and prognosis of field vehicles and potentially reducing vehicle warranty costs and improving customer loyalty and satisfaction.

3.3. Lithium-Ion Battery Chemistry

Li-ion battery (LIB) are the most common type of battery chemistry used in modern EV applications due to their stellar energy and power density characteristics compared to other battery types and chemistries. Lithium metal is light weight and has the greatest electrochemical potential of all metals [35]. This unique property of lithium allows Li-ion batteries to provide the highest specific energy density per weight compared to other chemistries such as Lead Acid or Nickel-based batteries. The LIB has no memory effect, minimal self-discharge, low maintenance and allow the flexibility of being manufactured in different geometries and sizes, which is beneficial for EV applications [35].

The LIB cell is the smallest unit of the LIB pack. The LIB cell consists of a positive electrode, known as the cathode, and a negative electrode, called the anode, separated electrically by a permeable solvent, called the electrolyte. The positive

electrode (the cathode) is typically a lithium metal oxide of some sort, such as LiCoO_2 , shown in Figure 3.1. The anode consists of porous carbon graphite that accept Li^+ during charging (Figure 3.1b). This process is referred to as intercalation and the reversible nature of this phenomena is what makes Li-ion batteries very practical for EV applications. During discharge (Figure 3.1a), the anode material undergoes oxidation and Li^+ flow back to intercalate with cathode material which experiences reduction or gain of electrons in the external circuit, which by convention, is the current experienced by the load in the opposite direction.



(a) Lithium Cell Discharging

(b) Lithium Cell Charging

Figure 3.1. Lithium-Ion cell cross section with LiCoO_2 Cathode and Li_2C Anode [14]

Many other types of lithium metal oxides cathode materials are common in LIBs and offer different advantages for different applications. For EV applications, the most common positive electrode materials are Lithium Manganese Oxide (LiMn_2O_4), shortened to LMO, Lithium Nickel Manganese Cobalt Oxide (LiNiMnCoO_2), shortened to NMC, and Lithium Nickel Cobalt Aluminum Oxide (LiNiCoAlO_2), shortened to NCA [6]. Variations of anode materials also exist, such as Lithium Titanate (Li_2TiO_3),

shortened to LTO, which replaces the carbon graphite material with a more durable structure. However, carbon graphite is the dominant anode material in EV applications, due to the significantly higher specific energy density per weight. Carbon anode-based batteries can have energy densities as high as 250Wh/kg compared to LTO batteries, which are 50-80Wh/kg.

3.3.1. Lithium-Ion Battery Aging

Battery cell aging implies irreversible reactions that occur in a battery over time and have adverse effects on battery performance and dependability [14]. This phenomena in batteries are not quite understood fully and the non-uniform occurrence makes it difficult to model. It is critical however, for safe operation of EVs, to qualitatively and quantitatively understand the aging phenomena from a practical sense.

Cell aging can be quantified by two simple concepts, capacity fade and power fade. Capacity fade occurs when the total capacity of a battery or the total amount of charge that can be retrieved or put into a battery decreases over time. Capacity fade is typically the metric used in determining the end-of-life (EOL) of a battery pack or cell by original equipment manufacturers (OEMs), which is typically 70% of the original capacity for EV applications. Power fade however, correlates to an increase in the equivalent series internal resistance of the cell or pack, which is a major factor in the power calculation or state of power (SOP) determination of an EV [50]. These characteristics in li-ion batteries occur primarily due to side reactions inside of the battery and physical deterioration of battery components under normal and strenuous battery operating conditions.

3.3.2. Lithium-ion Cell Aging - Qualitative analysis

Capacity and power fade in a Li-ion cell could occur from a number of different physical and chemical processes that may or may not have a direct correlation. This makes understanding Li-ion aging models a rather daunting task. In the following sections, a detailed overview of mechanisms that lead to aging in Li-ion batteries are presented. Aging phenomena in the positive cathode electrode differ significantly from aging in negative electrode materials and is characterized as such.

3.3.3. Lithium Ion Negative Electrode Aging

Graphite is the most commonly used material in li-ion cells and is the anode material of focus in most aging studies of li-ion cells. Aging effects in the anode of the cell can be observed at three different degrees of scale: the surface of the electrode particle, inside the electrode particle and more macroscopically within the composite anode structure as a whole [14].

When a molecule of the solvent comes in contact with the carbon during the intercalation of lithium ions, the electrolyte has a tendency to want to decompose and form other compounds with the graphite material. The product of this decomposition is a redox reaction that consumes some of the lithium ions, carbon particles and some of the electrolyte material [14]. This decomposition forms what is known as the solid-electrolyte interphase (SEI) film on the electrode surface. The formation of the SEI, typically inhibits the solvent from further reaction with the carbon electrode material and its porosity is such that lithium ions can still penetrate through its pores to intercalate with the carbon, however, some lithium ions are consumed in the process of creating the SEI and some capacity is lost initially.

Elevated temperature operating conditions of the cell could allow for accelerated aging of the cell as high temperatures could result in further decomposition of the SEI and increased reaction between the graphite material and the electrolyte to form new SEI layers, thereby further increasing the internal resistance of the cell and consuming additional lithium ions in the process or displacing carbon particles that would otherwise be hosts of lithium ions, forcing the lithium ions to combine with other unwanted compounds and form lithium metal. The process of forming lithium metal in the cell is called lithium plating and is an irreversible reaction. At lower temperatures lithium plating could further decompose into lithium dendrites and puncture the electrolyte separator potentially causing an internal short between the anode and cathode, a situation which could be dangerous and lead to fires.

Figure 3.2 is a diagram that describes changes at the anode and electrolyte interface. The formation of the SEI as can be observed from Figure 3.2 is accompanied by the release of gaseous electrolyte decomposition which must be vented out of the battery. The exact amount of lithium ion consumed during the multiple stages of irreversible formulation of the SEI layer is not entirely known but is estimated to be dependent on the conditions with which they are formed, and the surface area of the graphite exposed to the electrolyte solvent.

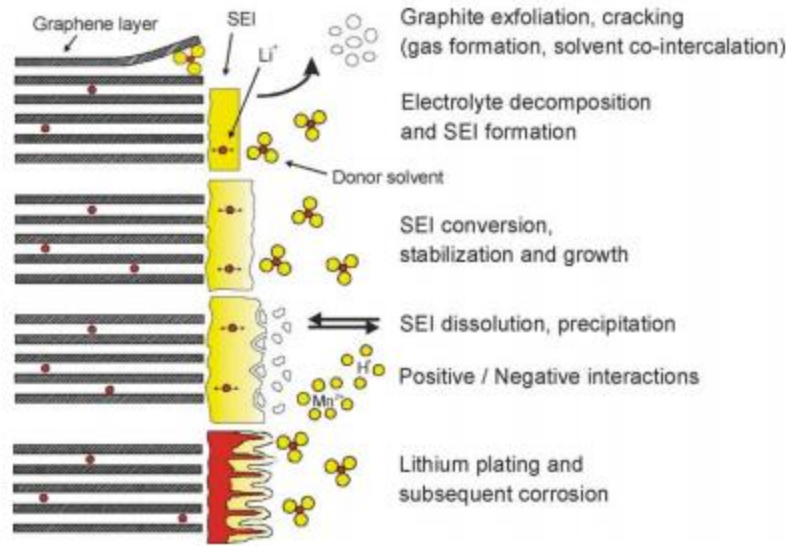


Figure 3.2. The SEI layer formulation between anode and electrolyte material [14].

Aging can also occur inside of the carbon particles themselves. Intercalation and deintercalation of lithium particles repeatedly over varying operating conditions can cause stress on the graphite particles and result in cracking of the particles, thereby damaging its structure and reducing potential hosts for lithium ions within the composite electrode.

Charging and discharging of cells over repeated cycles leads to small volume changes in the particles of the electrode which can cause stress and cracking of the electrode material, leading to further exposure of the graphite to the solvent and further decomposition of the SEI and creation of new SEI layers.

The repeated stress and strain within the electrode material can transcend into electrical and mechanical failure of other physical components of the electrode material such as deterioration or corrosion of the current collector, electrical contact loss between

binders and particles, current collector and particles, and so on [6]. Table 3.1 below is a summary of the aging attributes of the negative electrode material in lithium-ion cells.

Table 3.1. Summary of aging at negative electrode [14].

Cause	Effect	Leads to	Enhanced by
Electrolyte decomposition, builds SEI, continuous low-rate reaction	Loss of lithium, impedance rise	Capacity fade, Power fade	High temperatures, high SOC (low potential)
Solvent co-intercalation, gas evolution and subsequent cracking formation in particles	Loss of active material (graphite exfoliation), loss of lithium	Capacity fade	Overcharge
Decrease of accessible surface area due to continuous SEI growth	Impedance rise	Power fade	High temperatures, high SOC (low potential)
Changes in porosity due to volume changes, SEI formation and growth	Impedance rise, larger overpotentials	Power fade	High cycling rate, high SOC (low potential)
Contact loss of active material particles due to volume changes during cycling	Loss of active material	Capacity fade	High cycling rate, low SOC
Decomposition of binder	Loss of lithium, loss of mechanical stability	Capacity fade	High SOC (low potential), high temperatures
Current collector corrosion	Larger overpotentials, impedance rise, Inhomogeneous distribution of current and potential	Power fade, Enhances other aging mechanisms	Overdischarge, low SOC (high potential)
Metallic lithium plating and subsequent electrolyte decomposition by metallic lithium	Loss of lithium (loss of electrolyte)	Capacity fade (power fade)	Low temperature, high cycling rates, poor cell balance, geometric misfits

3.3.4. Lithium Ion Positive Electrode Aging.

The most prevalent aging factor observed in positive electrode materials is the dissolution of the metals in the positive electrode into the electrolyte, creating high resistance films that can cause power fade effect in the cell. This typically occurs during low/high SOC operations. An explanation for this can be observed by looking at the layered structure of a positive electrode material. In Figure 3.3, it can be observed that the structure of material is such that lithium ions are stored in between thin and delicate layers of the metal oxide like pillars, as is the case in the Li-cobalt oxide shown in Figure

3.3. During charge, as the lithium ions are extracted from the metal oxide, at high SOC, there are only a few lithium (pillars) ions left in the cathode to keep the structure intact. At high temperatures, this could cause the metal oxide to become unstable and dissolve into the electrolyte resulting in capacity loss. These materials could sometimes end up at the negative electrode material, poisoning the negative electrode.

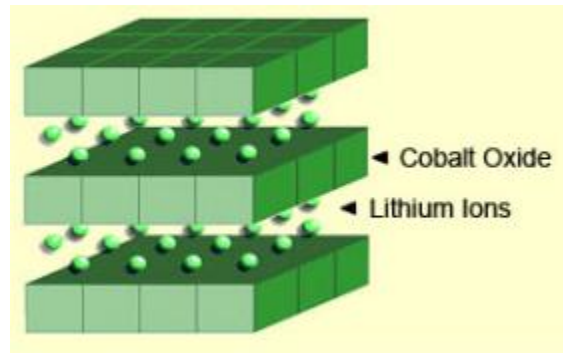


Figure 3.3. Li-cobalt oxide structure [35].

Other aging processes that occur in the positive electrode are summarized in Table 3.2.

Table 3.2. Summary of aging at positive electrode [14].

Cause	Effect	Leads to	Enhanced by
Phase transitions	Cracking of active particles	Capacity fading	High rates, high/low SOC
Structural disordering	Lithium sites lost and lithium trapped	Capacity fading	High rates, high/low SOC
Metal dissolution and/or electrolyte decomposition	Migration of soluble species,	Capacity fading	High/low SOC, high temperature
	Reprecipitation of new phases,	Power fade	
	Surface layer formation	Power fade	
Electrolyte decomposition	Gas evolution		High temperature
Binder decomposition	Loss of contact	Power fade	
Oxidation of conductive agent	Loss of contact	Power fade	
Corrosion of current collector	Loss of contact	Power fade	High SOC

Quantifying these aging processes described above with high fidelity models based on measurable data such as currents and voltages is the goal of this research work and a framework for doing this is proposed in this chapter.

3.4. Equivalent Circuit Model and Parameter Estimation

Simulating EV battery packs are important for computing key estimates of several battery parameters such as state of charge (SOC), state of health (SOH), state of power (SOP), range estimation, etc. Models and simulations of battery packs must provide a high degree of fidelity with minimal complexity.

Equivalent circuit models (ECM) are analogies that correlates the operation of simple circuit elements such as sources, resistors and capacitors to the electrochemical phenomena that occur inside of the battery. They have the advantage of being computationally simple and highly intuitive descriptions of the electrochemical reactions that occur in a cell and are useful for simple and fairly accurate estimations of battery state.

Figure 3.4 shows a generalized ECM that can be used to represent a single Li-ion cell [19], where open circuit voltage $OCV(z(t))$, R_l , C_l and R_o elements are a function of SOC and temperature T, and the cell output voltage is described by

$$v(t) = OCV(z(t)) - R_l \dot{i}_{Rl}(t) - R_o \dot{i}(t) \quad (3.1)$$

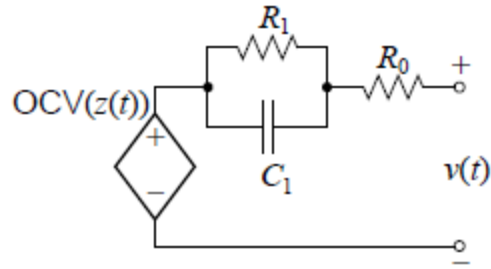


Figure 3.4. Equivalent Circuit Model of a Li-ion Battery [19].

The series resistor R_0 represents the instantaneous response of the cell voltages, while the RC pair represents the delayed response of the cell, as described in Figure 3.5.

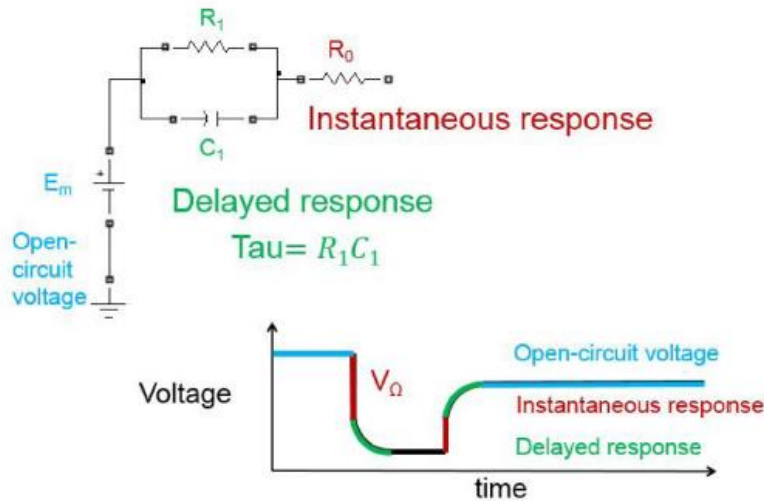


Figure 3.5. Illustration of equivalent circuit elements representation of cell voltage [19].

To estimate the equivalent circuit parameters for a given cell, the following experiments were carried out and the current and voltage profiles of the cell was measured throughout the experiment.

Keeping the temperature of the cell relatively constant beginning at 25 °C for each step, the following steps were carried out:

- Using a constant current at 1C rate, starting at 90% SOC (to avoid over-voltage) the cell is discharged by 10% to 80% SOC.
- The cell is left to rest for roughly 2 hours until all of the transients have settled.
- The cell is then discharged again by 10% at constant 1C and left to rest. This sequence is repeated until the cell is at 10% SOC left.
- The cell is then charged using the constant current, constant voltage (CCCV) method backs up to roughly 90% SOC.
- A new temperature is selected, the cell can come to the new temperature and the entire experiment is repeated again for the new temperature set.

After all experimental data is collected, initial guesses of the ECM parameters $OCV(z(t))$, R_1 , C_1 and R_0 are set based on voltage plot observation and MATLAB parameter estimation toolbox is used to fit the data measured during the experiment to newly estimated parameters iterated over time until a small margin of error for every corresponding SOC and temperature. Figure 3.6 shows plots of comparisons between simulated data and experimental data after this parameter estimation process has been completed. The result is a series of look up tables or matrices for all elements of the ECM corresponding to a certain SOC and temperature.

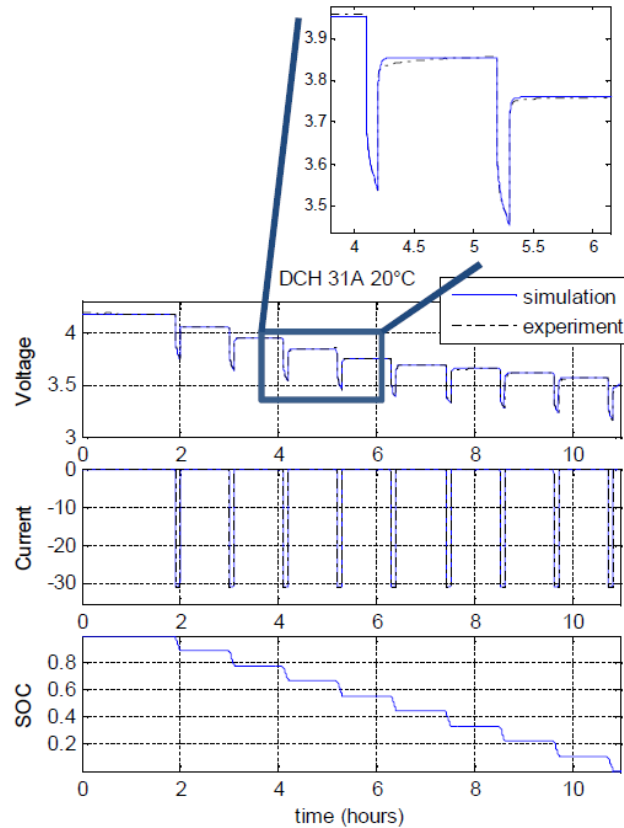


Figure 3.6 MATLAB parameter estimation simulated results compared to experimental data [19].

Table 3.3 below is an example of a 10 x 3 look up table (LUT) of ECM parameters modeled in MATLAB for a Li-ion cell. This cell model can be used to represent an ECM cell model in the Battery Management System (BMS) of an EV and aid in the quick estimation of different battery back parameters. The cell mass (`cell_mass`), cell mass density (`cell_rho_Cp`) and cell heat capacity (`cell_Cp_heat`) can typically be found in the battery specification sheet provided by the battery manufacturer. These parameters in addition to the parameters deduced from the parameter estimation technique can be used to represent a physical cell model within MATLAB/Simscape.

Table 3.3 ECM of Li-ion cell parameter estimation in MATLAB

Field ▲	Value
SOC_LUT	[0;0.2336;0.3294;0.4252;0.5210;0.6168;0.7126;0.8084;0.9042;1]
Temperature_LUT	[278.1500,293.1500,323.1500]
Capacity_LUT	[31,31,31]
Em_LUT	10x3 double
R0_LUT	10x3 double
R1_LUT	10x3 double
C1_LUT	10x3 double
cell_mass	0.8400
cell_rho_Cp	2040000
cell_Cp_heat	964.9200

Figure 3.7 is a Simscape model of a battery cell, which uses a LUT described in Figure 3.8 as variables that represent the cell. The modeled cell also allows for a physical thermal port to model the cell thermal conductivity properties with ambient or other cells around it. The modeled cell can also be initialized with an initial SOC and compute its internal SOC at every timestep during simulation. Figure 3.8 describes the parameters we set for the cell modeled. The main tab represents the main parameters of the cell which include the SOC, OCV, temperature, series resistance and capacity LUT. In the dynamics tab, we describe the delayed response LUT parameters which include the polarization resistance and the time constant which is a function of the polarization resistance and capacitance which are estimated from the parameter estimation process. The thermal tab indicates the parameters needed to calculate the thermal response of the cell and the variables tab allows us to set up some initialization properties of the cell such as initial SOC and initial cell temperature.

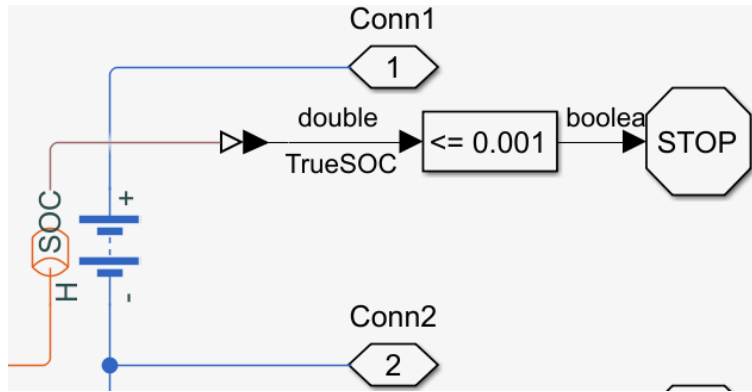


Figure 3.7. MATLAB/Simscape cell model with thermal port.

Figure 3.8 displays four screenshots of the MATLAB/Simscape cell model parameter configuration interface, showing various tabs and settings.

Screenshot 1: Main Parameters

- Vector of state-of-charge values, SOC: Battery.SOC_LUT
- Temperature dependent tables: Yes - tabulate parameters over temperature
- Vector of temperatures, T: Battery.Temperature_LUT (Unit: K)
- No-load voltage, V0(SOC,T): Battery.Em_LUT (Unit: V)
- Terminal resistance, R0(SOC,T): Battery.R0_LUT (Unit: Ohm)
- Ampere-hour rating, AH(T): Battery.Capacity_LUT (Unit: hr*A)
- Self-discharge: Disabled
- Extrapolation method for all tables: Linear

Screenshot 2: Charge Dynamics

- Charge dynamics: One time-constant dynamics
- First polarization resistance, R1(SOC,T): Battery.R1_LUT (Unit: Ohm)
- First time constant, tau1(SOC,T): Battery.R1_LUT.*Battery.C1_LUT (Unit: s)

Screenshot 3: Thermal Mass

- Thermal mass: Battery.cell_mass*Battery.cell_Cp_heat (Unit: J/K)

Screenshot 4: Override Table

Override	Variable	Priority	Beginning Value	Unit
<input type="checkbox"/>	Current (positive in)	None	0	A
<input type="checkbox"/>	Voltage	None	0	V
<input checked="" type="checkbox"/>	State of charge	High	- Battery.Qe_init)/Battery.Capacity_LUT(1)	1
<input type="checkbox"/>	Discharge cycles	High	0	1
<input checked="" type="checkbox"/>	Temperature	High	Battery.TempInit	K

Figure 3.8. MATLAB/Simscape cell model parameters.

Figure 3.9 is a model of a lithium ion cell that is thermally insulated and subjected to ambient temperature input T . The cell input is a drive cycle current measurement and the model is instrumented to measure voltage, temperature, and SOC. The model is initialized to a SOC of 50% and temperature of ~ 293 K.

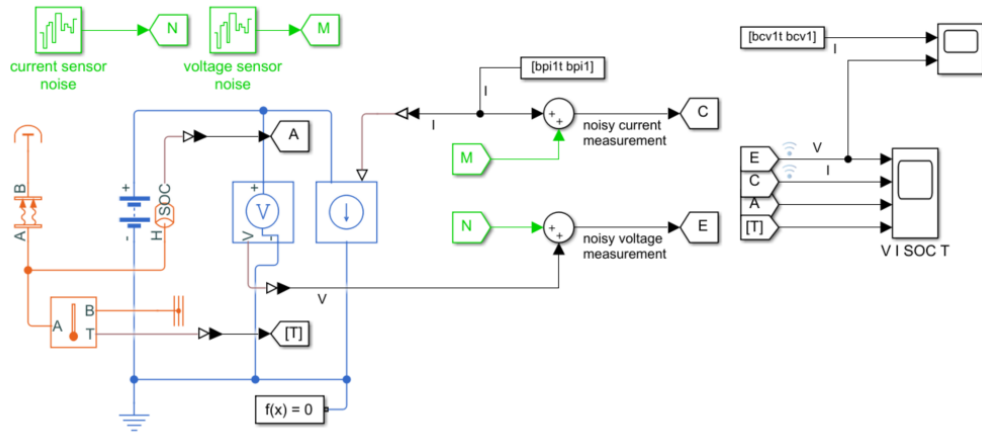


Figure 3.9. Model of lithium ion cell with thermal insulation and measurements.

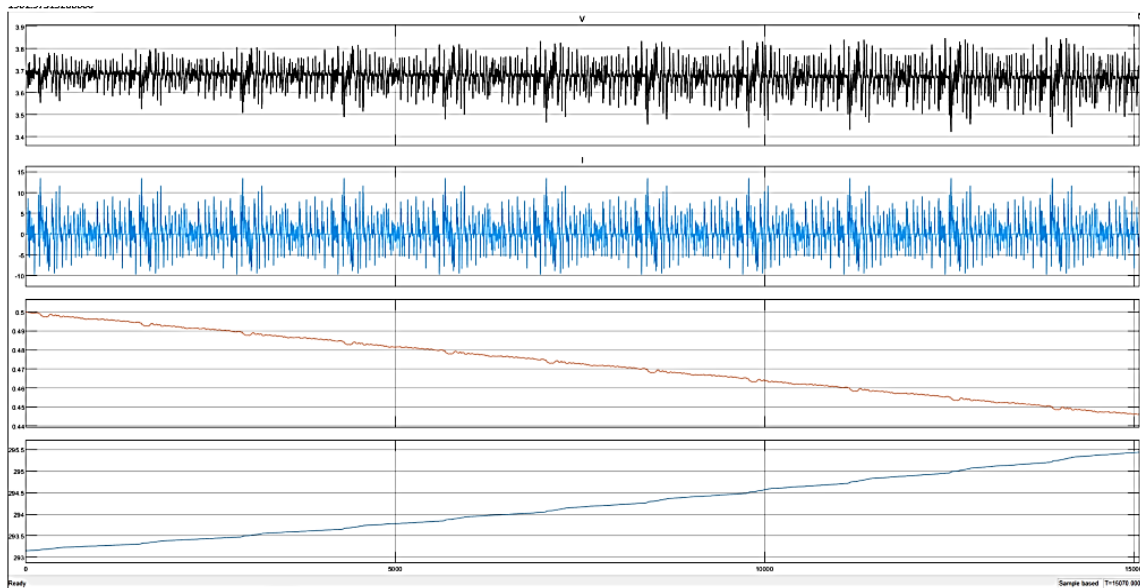


Figure 3.10. Measurements of Voltage, Current, SOC and Temperature.

The plots in Figure 3.10 show the dynamics of the cell being captured in detail. As the cell continues to be discharged and charged, the voltage of the cell responds similarly, the voltage plots look like an inverted version of the current input, due to the fact that a negative current represents load/discharge while positive represents charge. The SOC plot also responds dynamically, depleted to around 45% at the end of the simulation. The temperature of the cell also climbs from ~293 K to ~295 K.

3.5. Battery Management System

The battery management system is a critical component within a battery pack and is responsible for monitoring, protection, limitation and reporting of measurements from the battery pack. Modeling the battery pack with a BMS is important for representing the diverse duty cycles and environmental conditions that a battery will undergo in the real world. The model allows the different testing scenarios to be validated, for example a scenario where the battery SOC is low at say 30% and temperature is at 25°C. In this scenario, we might want to limit the current output of the pack due to the potential of an undervoltage fault if the requested current is too high. The plants being monitored and controlled by the BMS include the cells, cells temperature and voltage sensors shown in Figure 3.11, the passive balancing circuit in Figure 3.12 which includes a switch, a bleeder resistor and diode, and the pre-charge circuit in Figure 3.13. The pre-charge circuit takes input from the BMS and is used to protect the pack from an inrush of current when it is first connected to the pack or the inverter when it is initially connected to the battery. The cell strings in Figure 3.11 are indicative of the thermal asymmetry typically found in battery packs, where one end of the string is directly linked to ambient

temperature by convection while the other end is thermally insulated. This asymmetry can cause significant differences in temperatures across all cells.

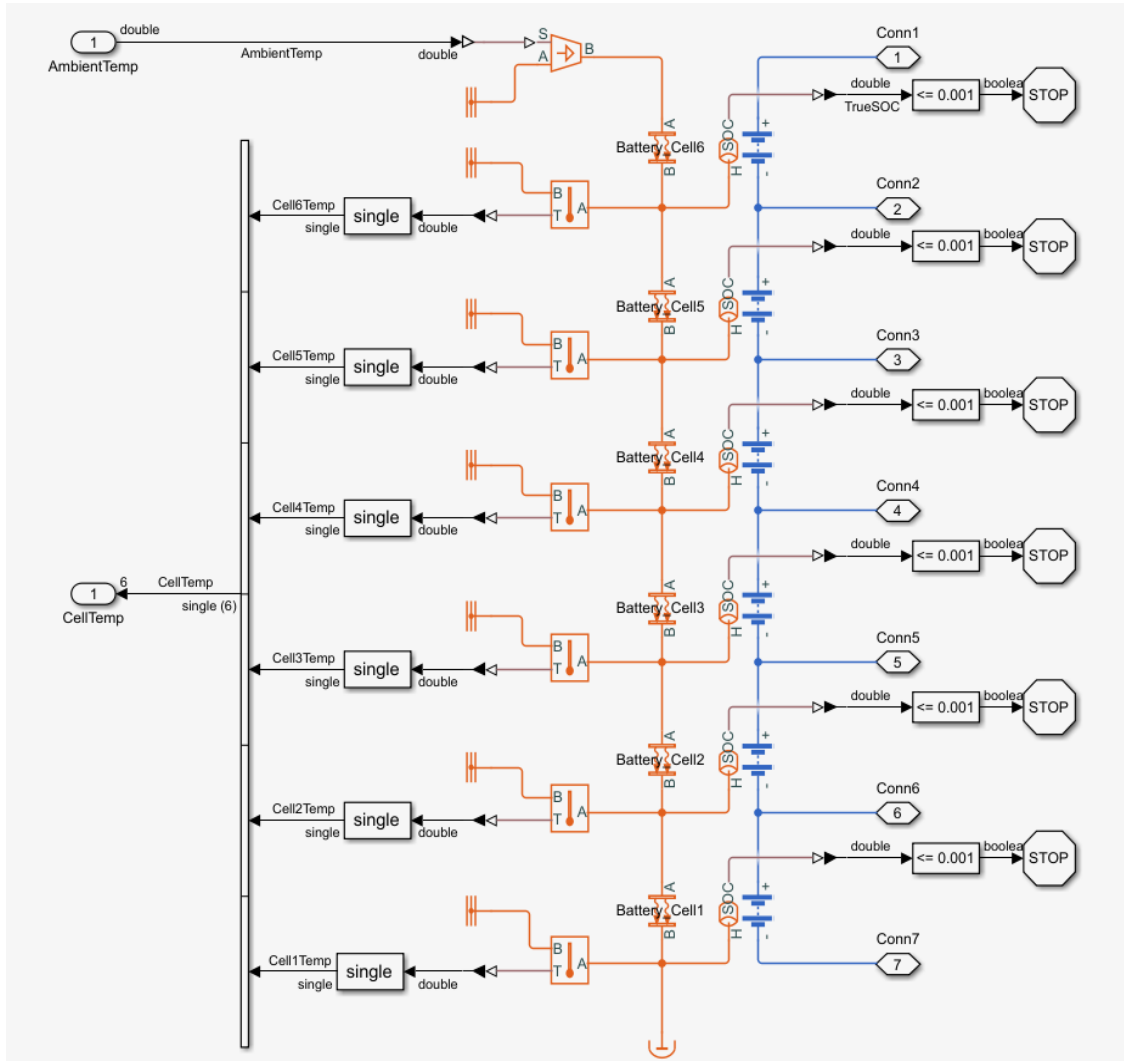


Figure 3.11. Battery Module with 6 cell strings and measurement sensors.

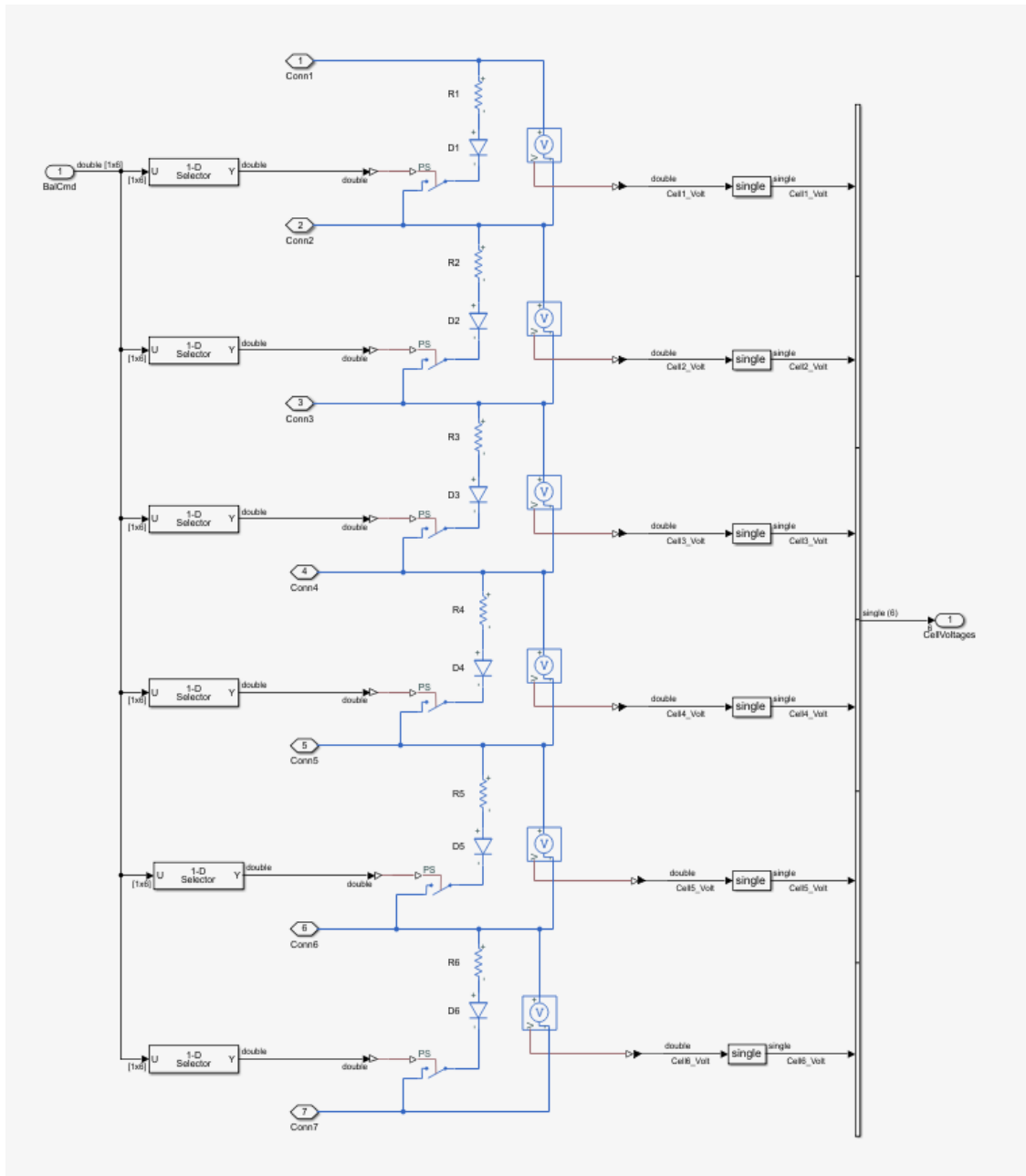


Figure 3.12. Battery passive balancing circuit.

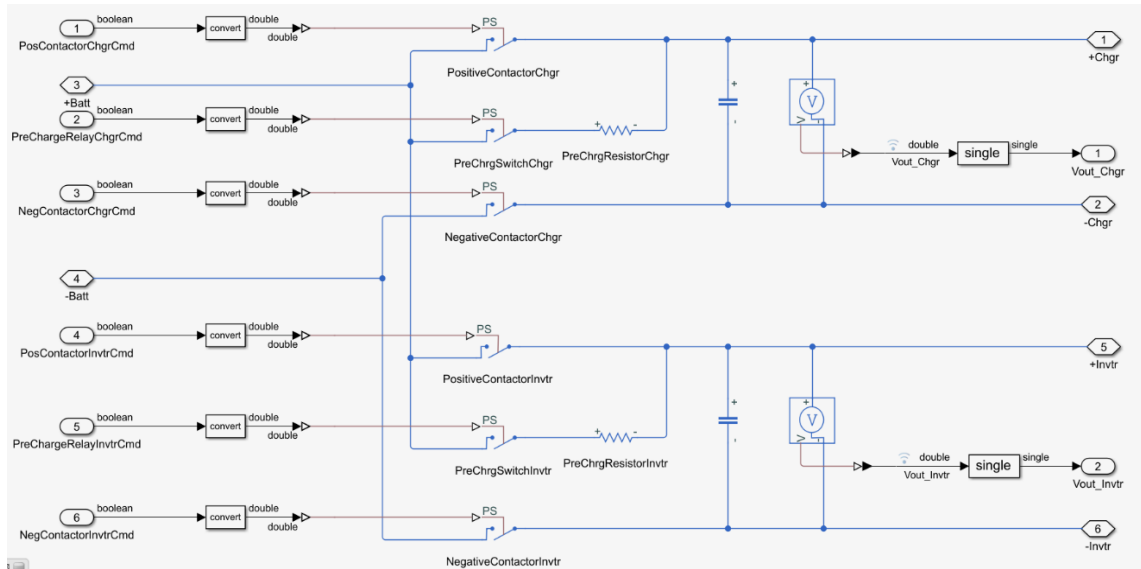


Figure 3.13. Battery pre-charge protection circuit.

Figure 3.14 is a diagram that describes the circuitry of a typical BMS. The BMS cell balancing and sensing module is responsible for sensing voltages of individual cells within the pack or module within an accuracy tolerance of $5\text{mV} \pm$ and balancing the voltage across all of the cells. The balancing could occur right after charging or during charging of the cells. The BMS is also responsible for over-charge/over-discharge protection with a delay time of 1000ms and a voltage tolerance of $\pm 0.1\text{V}$ the threshold voltage, over-discharge current protection with a delay time of 5ms, short circuit protection with a delay time of 5ms, temperature sensing and temperature protection with a tolerance of ± 5 degree C. The module also has a low power on-board computer, GPS sensor and wireless communication module. The onboard computer can run different algorithms online to help the battery pack understand it's current duty cycle, state of charge, state of power, state of health and optimal operational point. It can also communicate information such as individual cell voltages, pack temperature, and battery

states to main Vehicle Control Unit (VCU). The BMS algorithm is responsible for following functions:

- Computing the minimum cell voltage and maximum allowable current threshold based on maximum internal resistance and temperature limits.
- Defining the battery state which indicates standby, driving, charging and fault states.
- Detection and turning on fault states which include over temperature, over voltage, over current, under voltage.
- Defining and controlling the contactor ON and OFF sequences.
- Controlling the balancing switching logic during battery stand by mode.

Figures 3.15 – 3.17 are plots showing the results of a BMS controlled battery pack which transitions from driving to charging and then to standby states. From the cell temperature plots, the temperature differences in the cells can be seen overtime due to the thermal asymmetry of the cells, and the BMS states are noticed indicating the battery state transitions through the driving and charging cycles. These state transition concepts can be modeled within MATLAB/Simulink using Stateflow Toolbox. From the voltage plots, stacked balance can be seen across all cells, which is due to the fact that the cells are all modeled with the exact same LUT parameters, hence there is no need for a balance command by the BMS as indicated in Figure 3.17.

During driving the similarities can be noticed between the current and voltage curves over time, however the average voltage of the pack decreases over time at the end of the driving state. During charging, the charge current starts off at around 30A and stays constants until the cell voltage reaches the voltage threshold, at which point the

currents starts to derate until the batter is fully charged. This charge control is performed by the BMS maximum allowable charge current algorithm. Once the battery is in standby mode, the cell voltages begin to settle to the no load voltage (OCV).

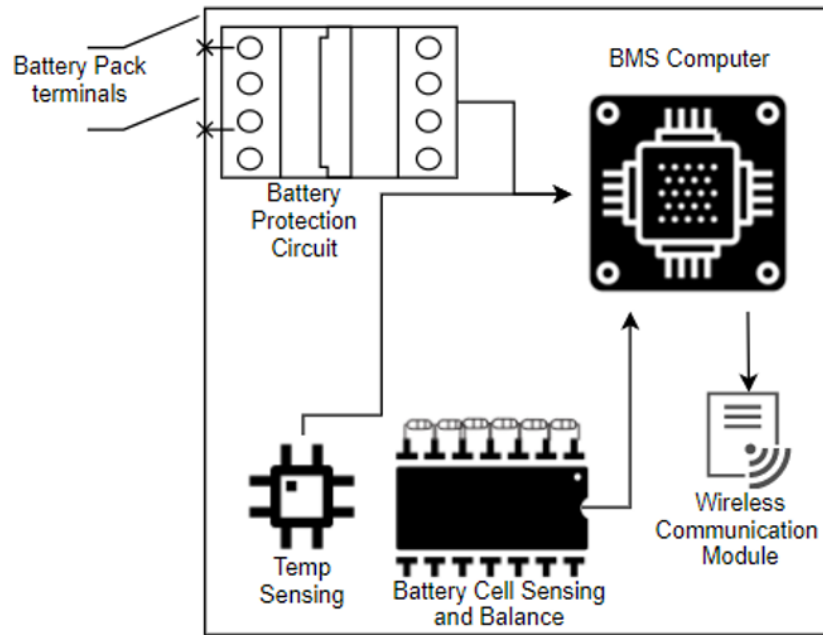


Figure 3.14. Battery Management System.

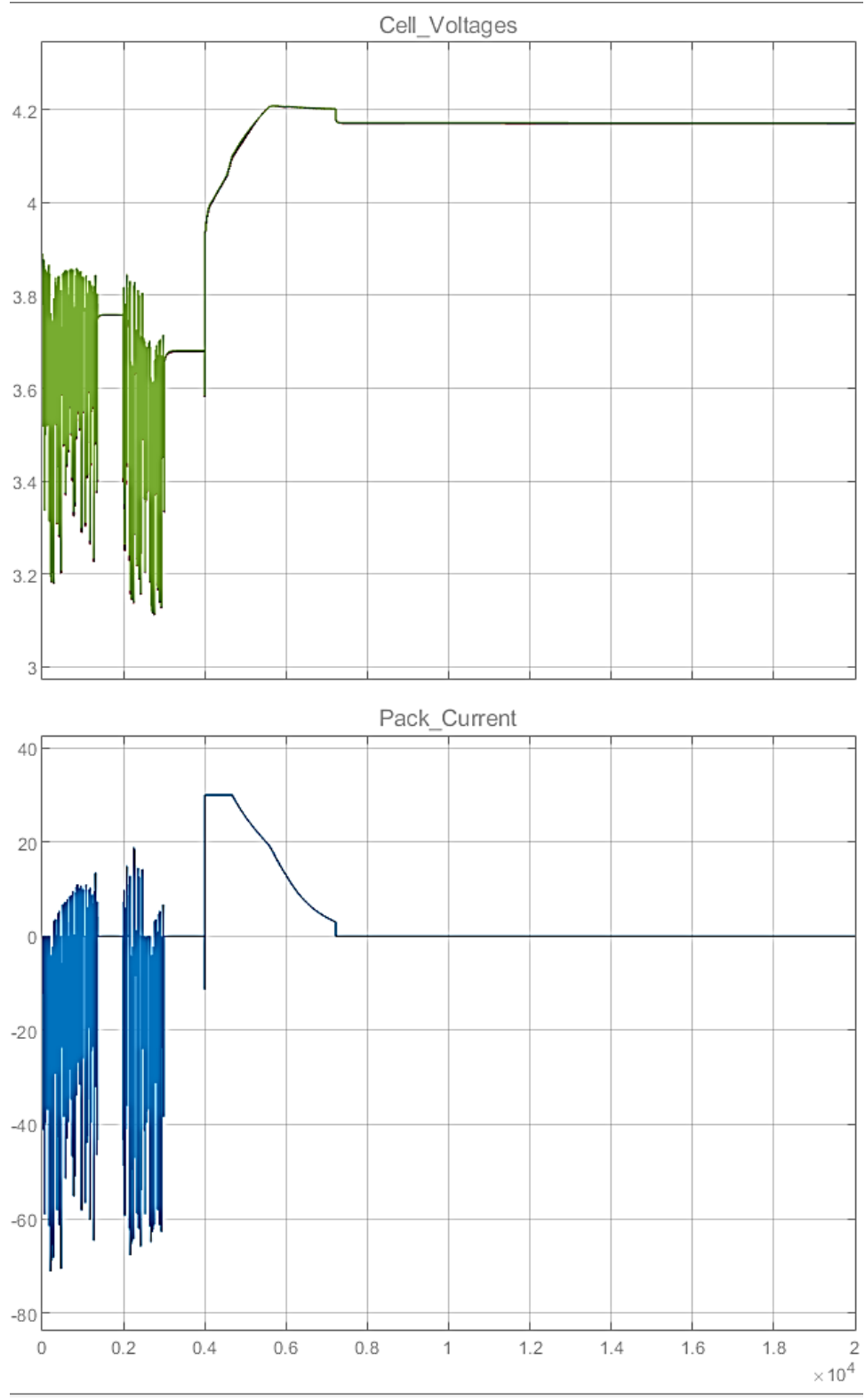


Figure 3.15. Battery voltages and currents for driving and charging cycles.

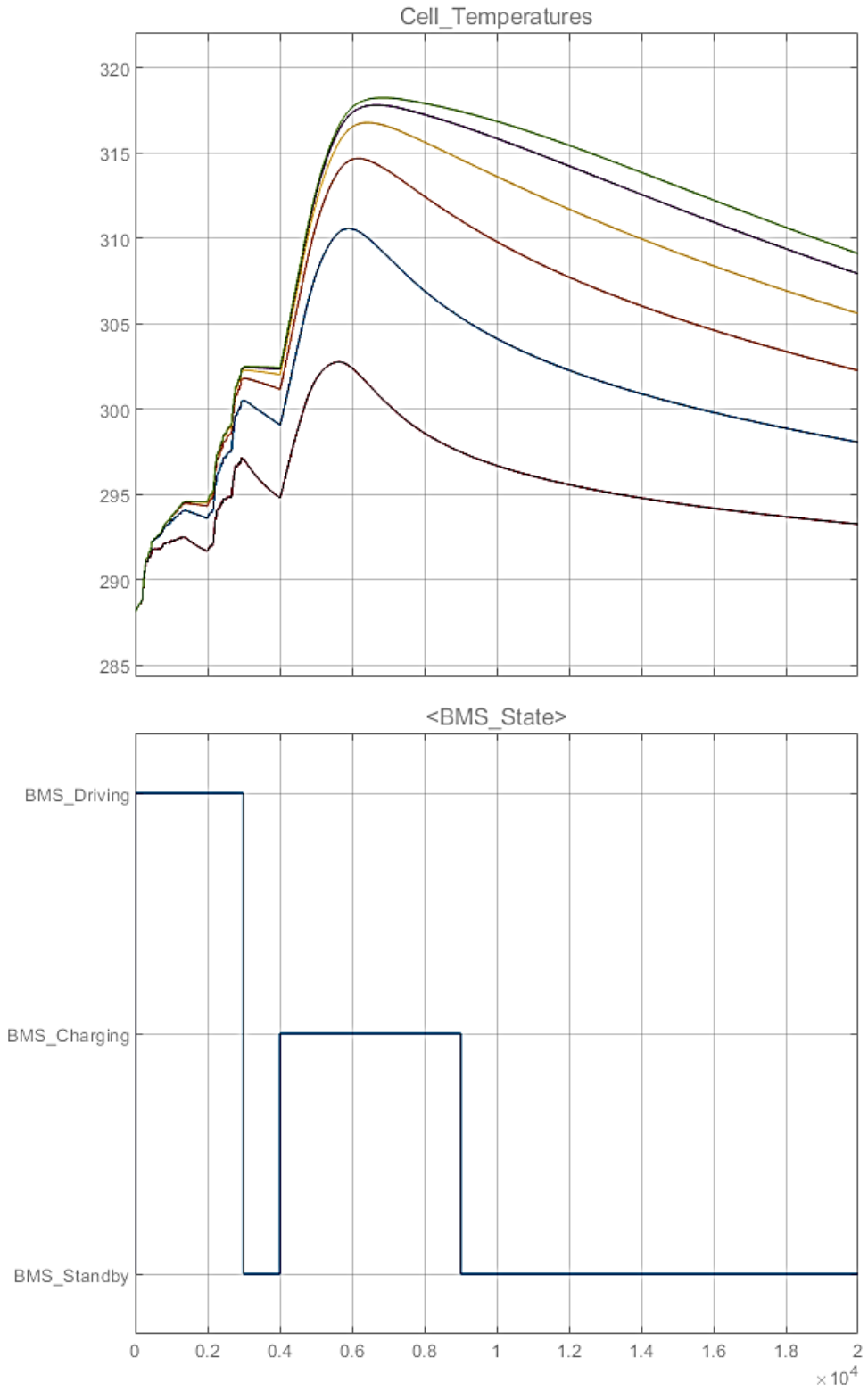


Figure 3.16. Battery cell temperatures and BMS states for driving and charging cycles.

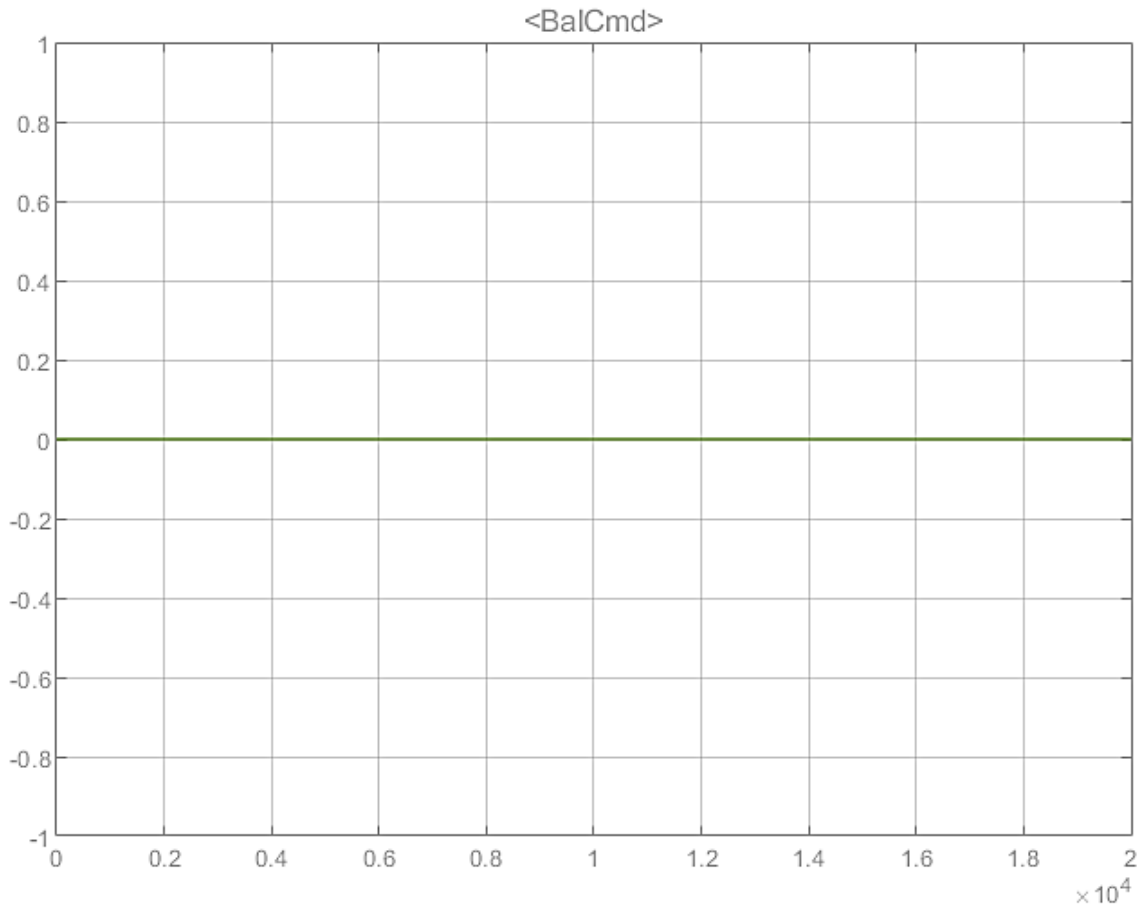


Figure 3.17. The BMS Balance command.

3.6. Battery State of Health Estimation

Rapid and accurate determination of the State of Health (SOH) of Li-ion battery-based energy storage system of an EV is necessary for optimal system operation, safety and reliability. Especially considering future Vehicle-to-Grid second life use applications. Current SOH estimation approaches either directly measure discharge capacity and internal resistance, or derive it from the battery pack's history, i.e., number of charge/discharge cycles and the associated charge- and discharge capacity and rate for each cycle [51]. EV batteries are considered to be at their end of life and due for replacement at below 80% of usable capacity compared to initial charge capacity. Figure

3.18 is a plot of tesla model S and X Tesla EV batteries degradation data aggregated over distance traveled; the distribution of SOH degradation could vary between EVs based on usage conditions as indicated in the figure.

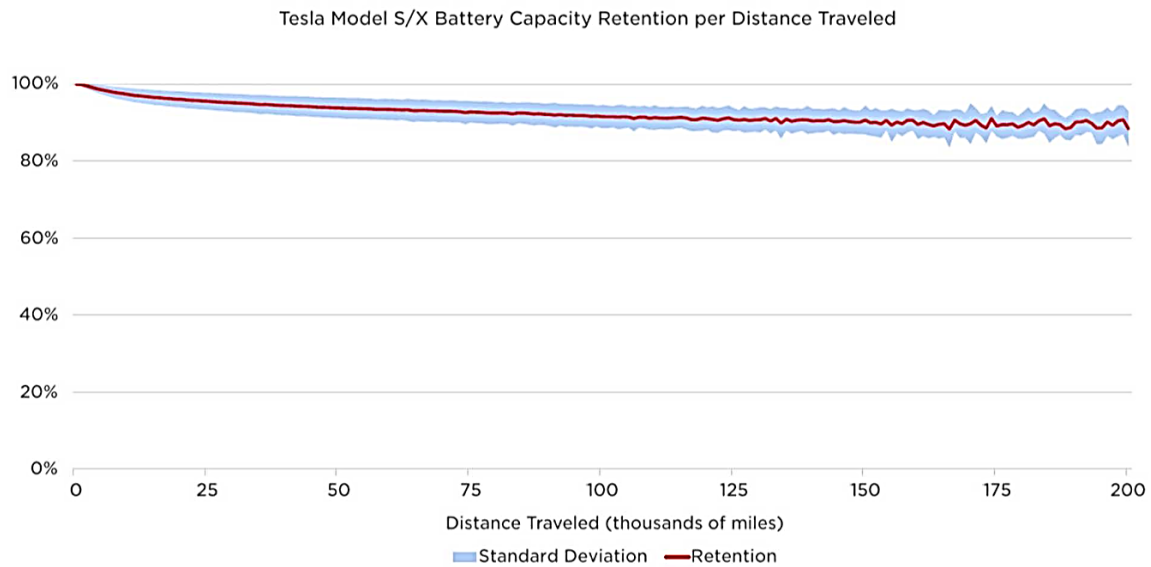


Figure 3.18. Tesla Model S/X Battery Capacity Retention over distance traveled.

Given the importance of SOH of batteries, a method for rapid and accurate determination of SOH was investigated and is proposed in this section. The common approach to battery charging is the Constant Current, Constant Voltage (CCCV) process shown in Figure 3.19, in which the maximum current supplied by the charger is maintained during the constant current portion of the charge (highlighted in red), and then a controlled constant voltage region kicks off where the voltage is held constant (highlighted in blue). At this time in the process, the current is tapered off by the charger controls to not cause the maximum voltage to be exceeded [50]. This transitional region (highlighted in orange) is of interest in rapid SOH modeling.

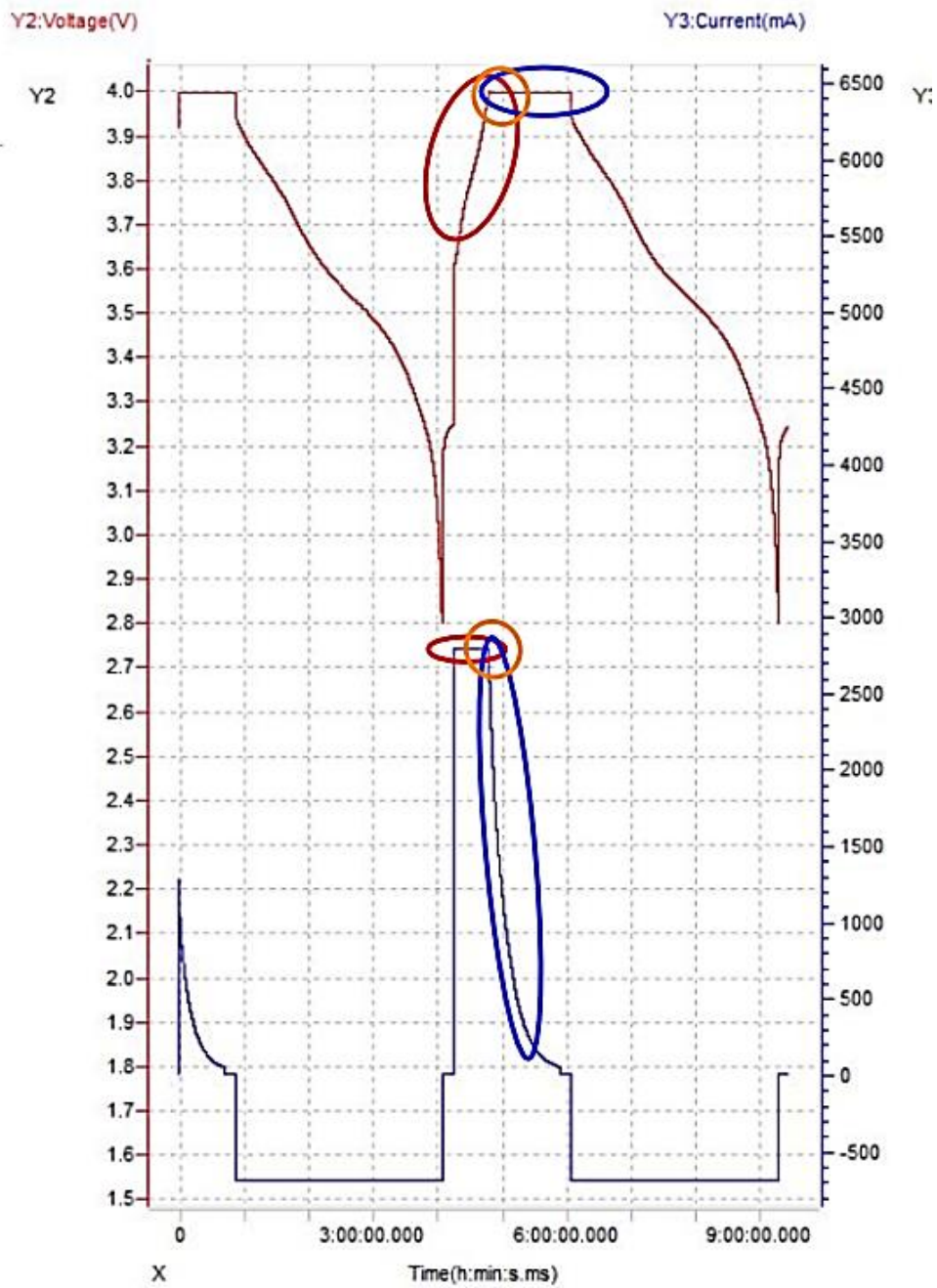


Figure 3.19. Battery Charging in CCCV.

3.6.1. SOH Estimation Experimental Validation

Researchers at MIT conducted aging experiments on 124 commercial Li-ion batteries cycled to failure under fast-charging conditions [53]. The cells were lithium-ion

phosphate (LFP)/graphite cells, manufactured by A123 systems cycled on a 48-channel Arbin LBT potentiostat in a forced convection temperature chamber set to 30°C. The cells have a nominal capacity of 1.1Ah and nominal voltage of 3.3V. Figures 3.20 and 3.21 are plots of the voltage and currents recorded during charge and discharge for each individual cycle that was run on one individual cell. Figure 3.22 is a plot of the charge capacity over all of the cycles. The red squares within the plots highlight region of time when the cells were being charged. From the current and voltage plots, it can be observed that the dramatic changes in the curves between the transition region from CCCV as the cell continues to age. The charging policy was set to start at a constant-current steps of 4C, 3C and then 1C, however as the cell aged, the voltage of the cell increased to the maximum voltage threshold much quicker causing the CV region to be kicked off earlier. From the charge capacity curve in Figure 3.22, it can be observed that the initial capacity during early cycles goes from 1.1Ah to 0.88Ah in later cycles, a 20% decrease in capacity.

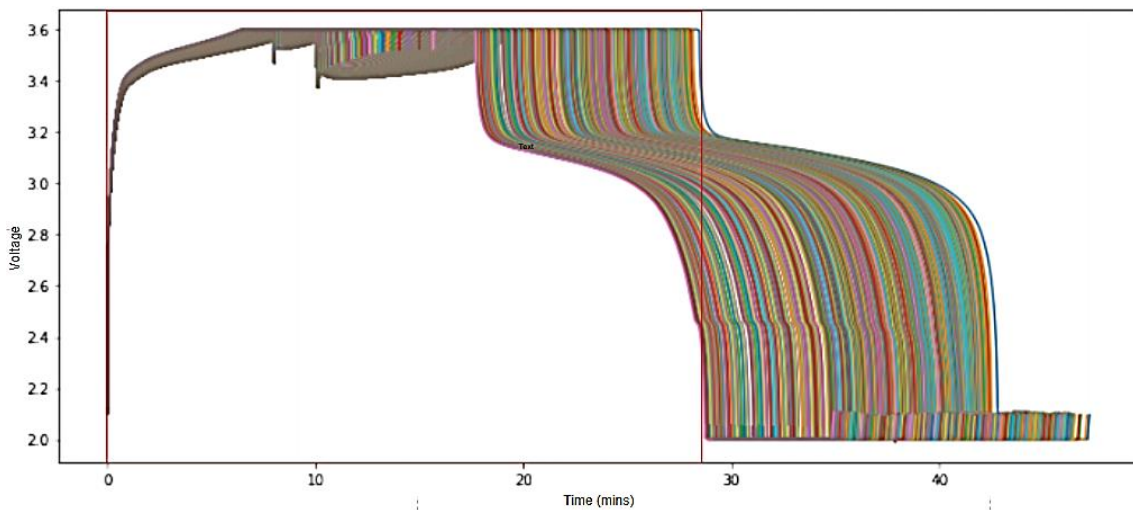


Figure 3.20. A123 Cell voltage over charge and discharge cycles.

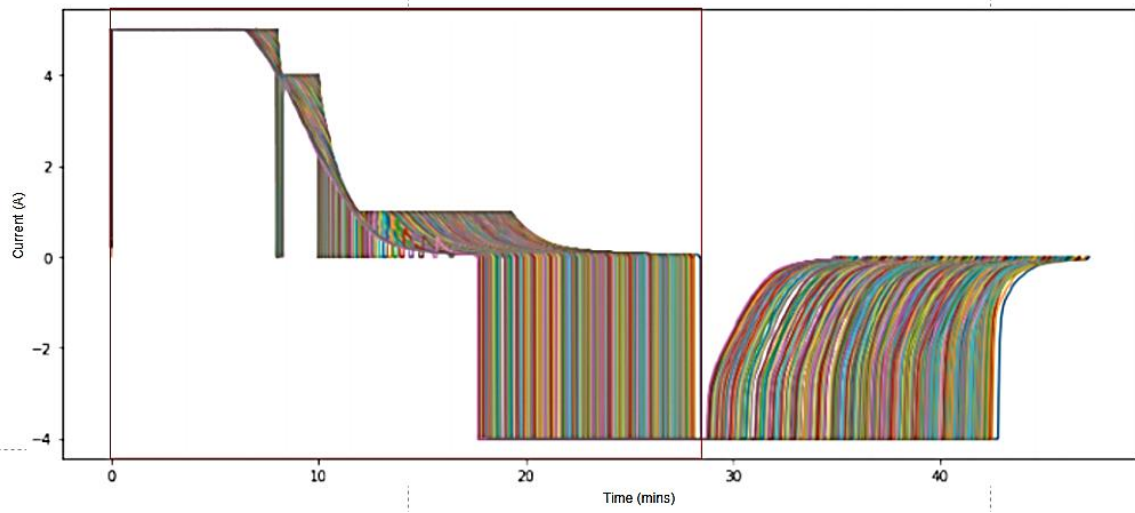


Figure 3.21. A123 Cell Current over charge and discharge cycles.

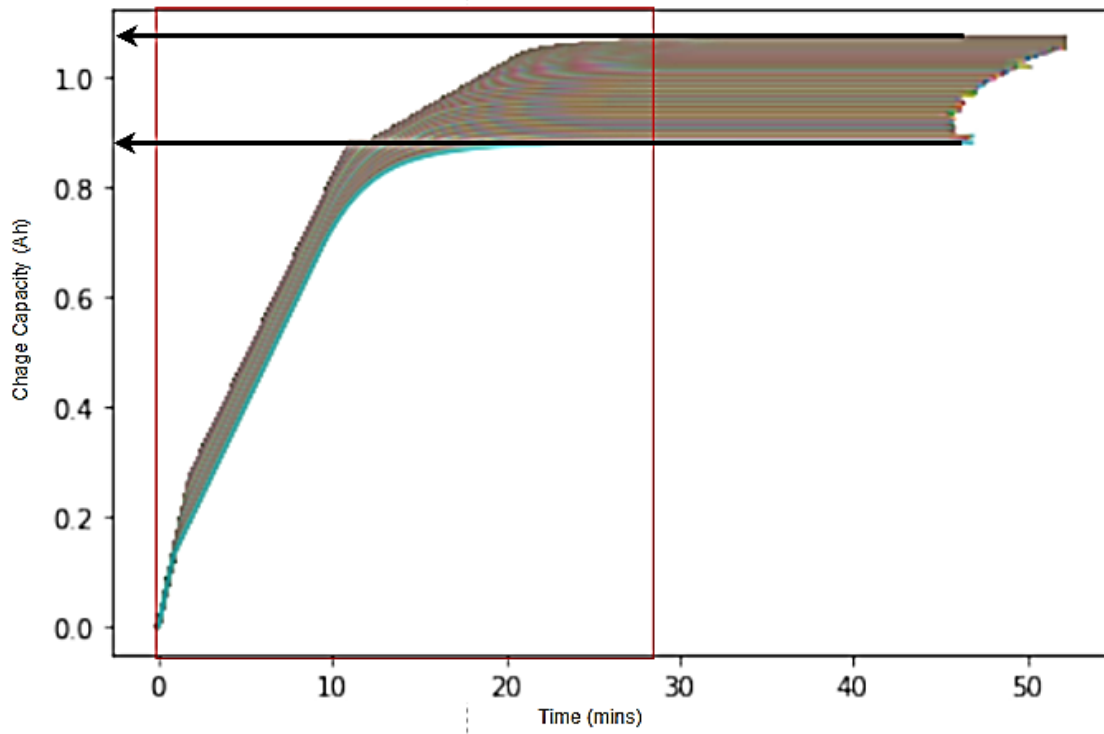


Figure 3.22. A123 Cell Charge capacity over charge cycles.

Figure 3.23 is a plot of charge capacity (Ah) over cycle indices for one of the A123 LFP/graphite cell, indicating the reduction in cell capacity as the cell aged. Figure 3.24 is a plot of the current in the CV region under the 1C charge policy indicating the changes in the curve as the cell ages, while Figure 3.25 is a plot of the voltage in the same CV region showing the charge controller keeping the voltage at the desired voltage maximum set within a margin of 0.0005V of the maximum voltage of 3.6V. Finally, Figure 3.26 is a plot of the gradient of the current curve at time $t+1$ for each individual charge/discharge cycle (cycle indices), showing a trend that correlates to the aging of the cell. Another measurable metric that can aid in the rapid estimation of the cell capacity/SOH is the charge time of the CV region for each cycle shown in Figure 3.27, however this method is less desirable in practice as the EV user may not complete the charging every time they plug in but are more likely to at least go through the transition from CC – CV during each charging session. Figure 2.28 is a model of current gradients mapped to capacity highlighting the correlation between the charge current gradient and capacity loss over the life of the cell.

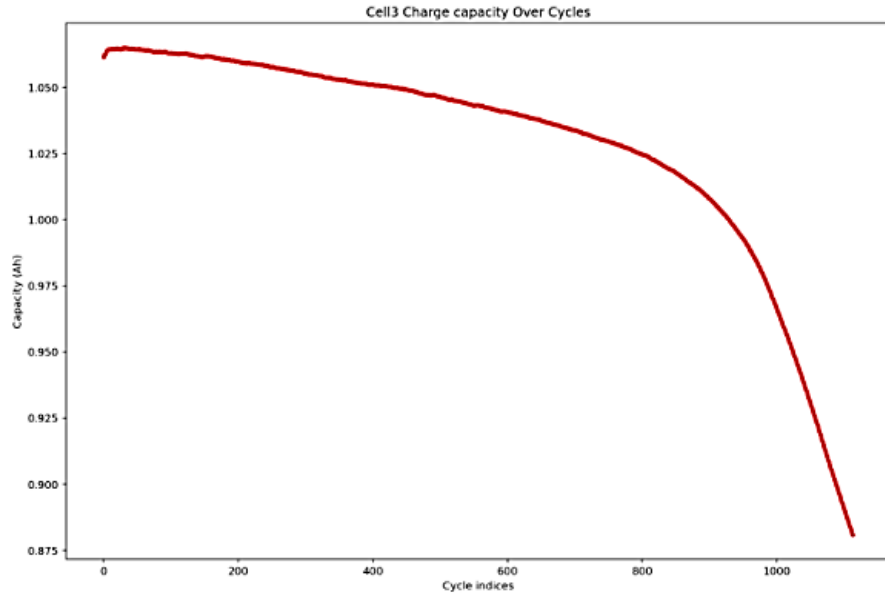


Figure 3.23. A123 Cell Charge capacity over charge cycle indices.

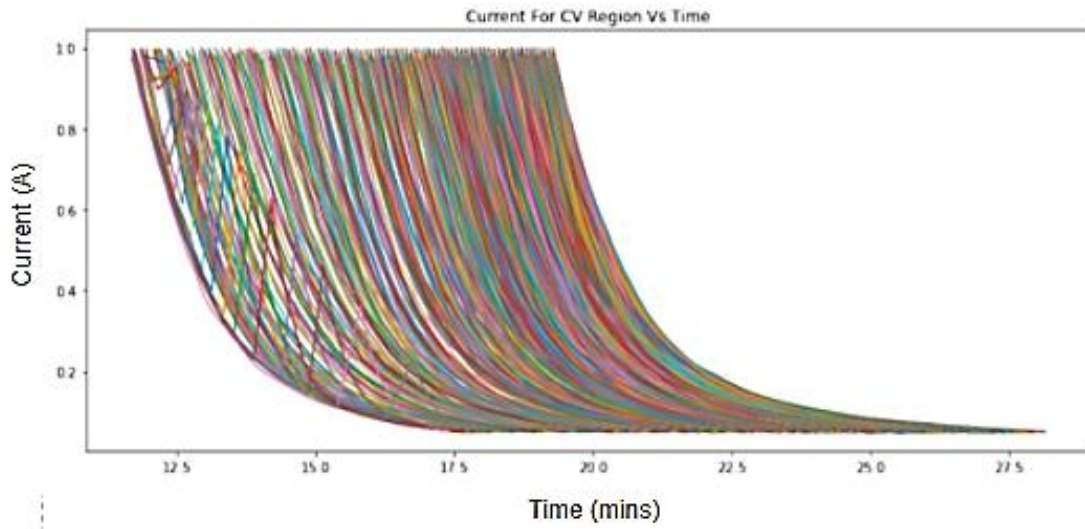


Figure 3.24. A123 Cell Current over charge cycle in CV region.

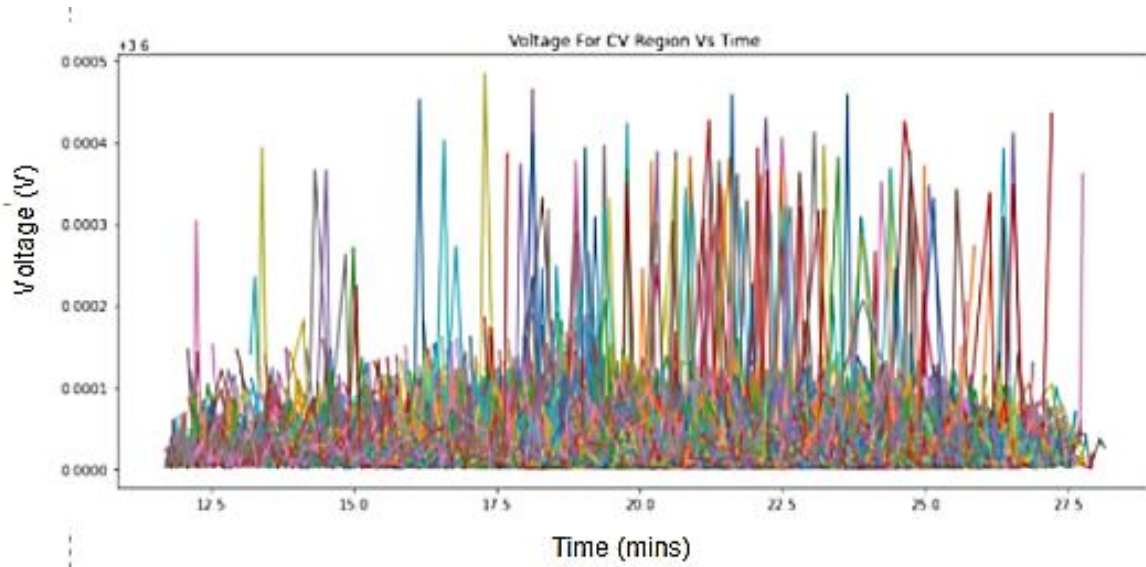


Figure 3.25. A123 Cell Voltage over charge cycle in CV region.

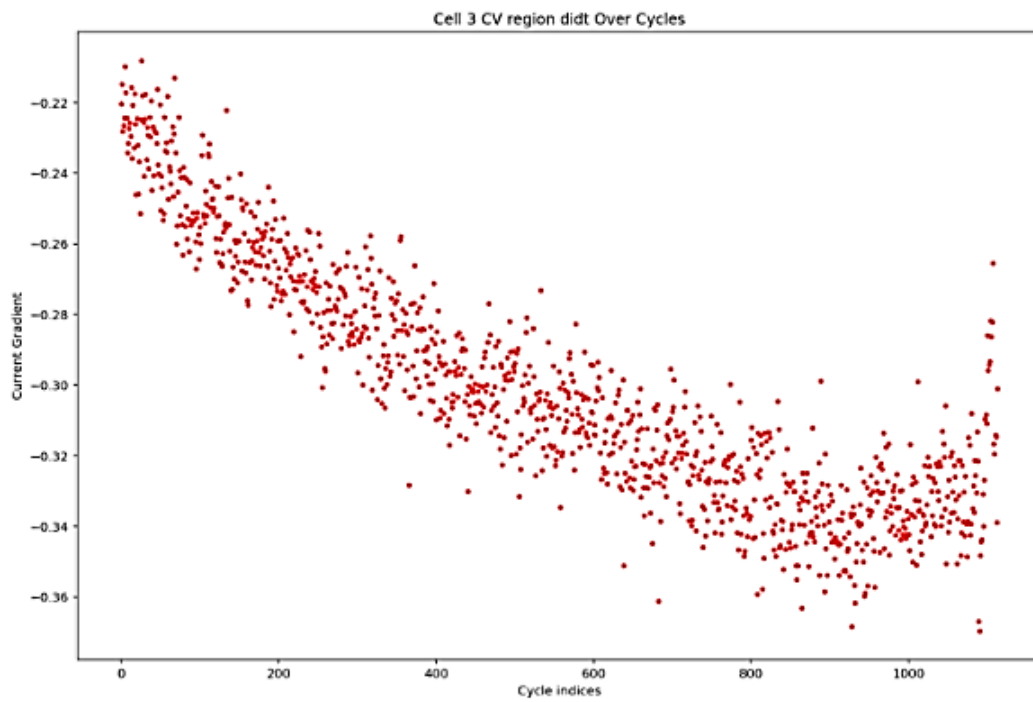


Figure 3.26. A123 Cell Current gradients in CV region over charge cycle indices.

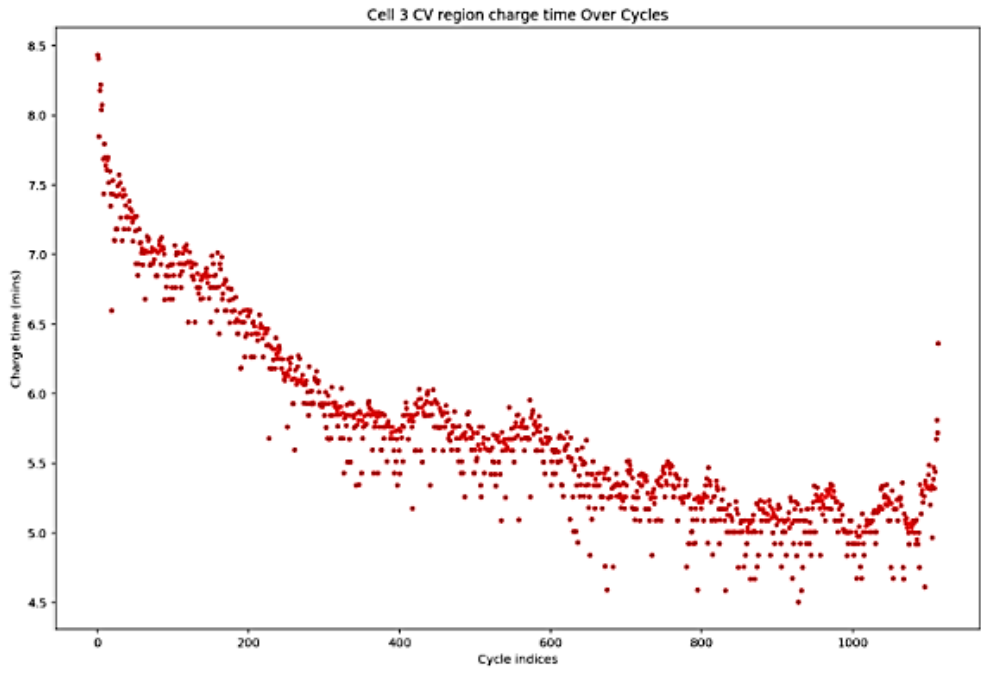


Figure 3.27. A123 Cell Charge time for CV region over charge cycle indices.

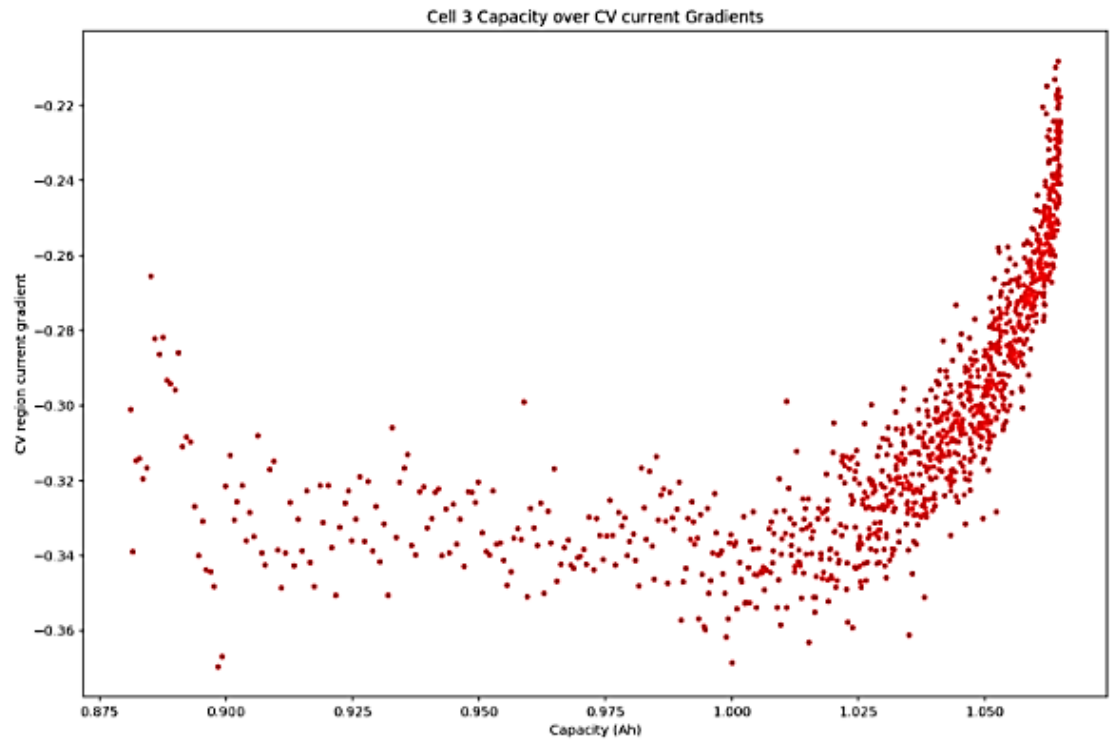


Figure 3.28. A123 Cell CV charge current gradient against capacity.

To further validate this rapid estimation methodology, application and robustness for other lithium-ion chemistries and charging policies, an experiment was set up in the Baylor Energy and Renewable systems lab. Nickel-cobalt-manganese (NCM)/graphite cells made by Panasonic were cycled (battery spec sheet shown in Figure 3.29) using an 8 channel, 5V 40A battery analyzer made by MTI corp.

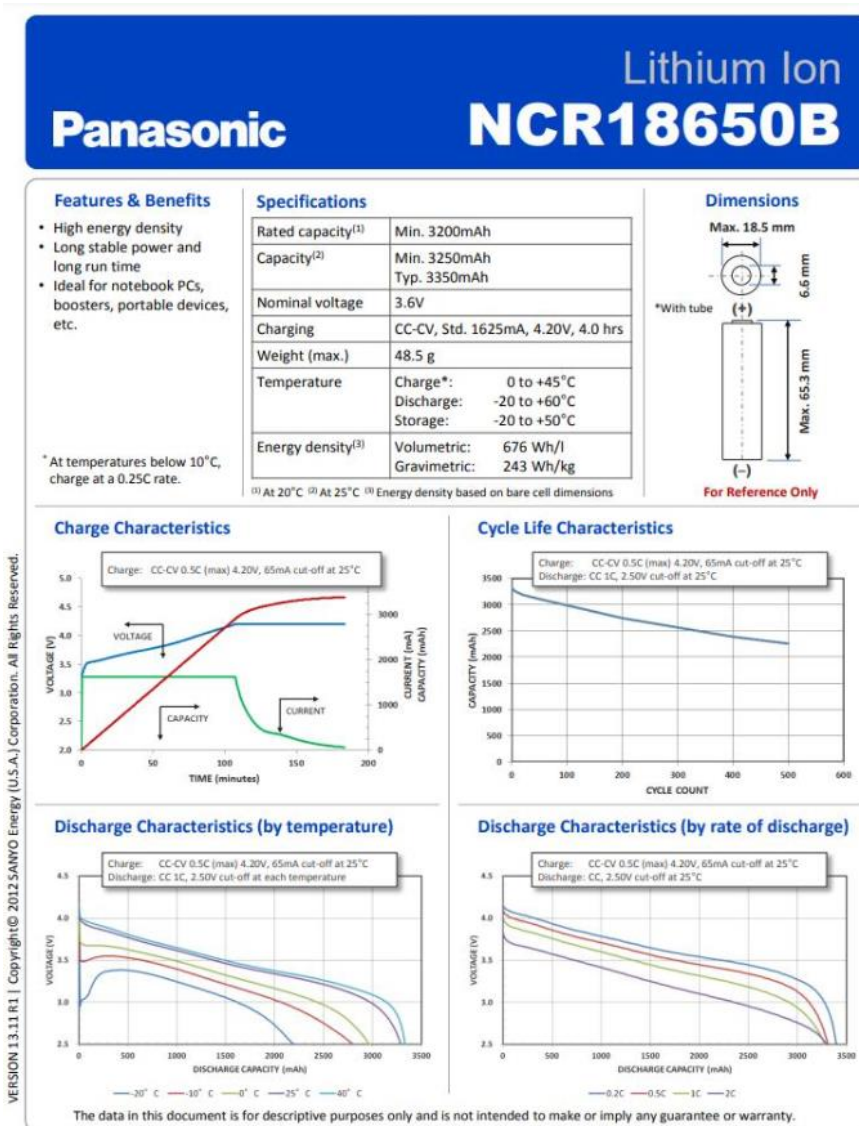


Figure 3.29. Panasonic NCM cell battery spec sheet.

A custom flooded battery enclosure shown in Figure 3.30 was designed and fabricated with a 3D printer to allow for coolant flow to extract heat by convection from the external surface of the cells so the temperature could be kept constant of 25°C during testing, this was monitored using a thermistor and Arduino setup. Figure 3.31 is a diagram of the experiment that was conducted.

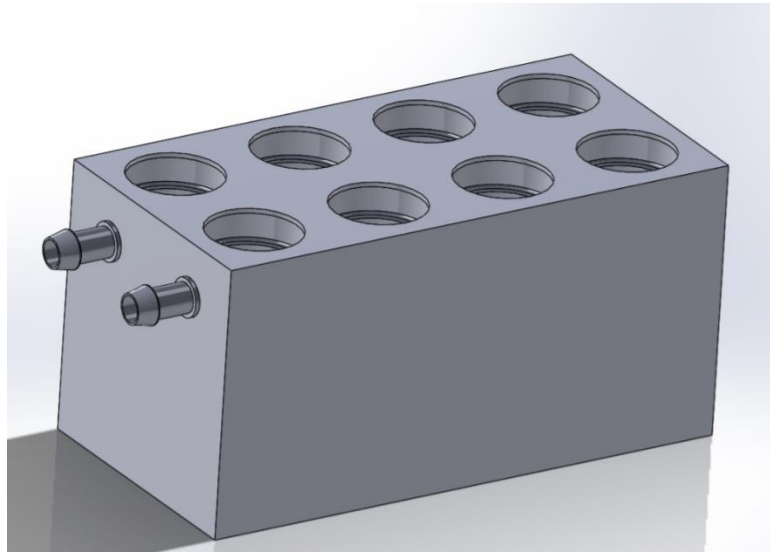


Figure 3.30. CAD 3D Model of flooded cell enclosure.

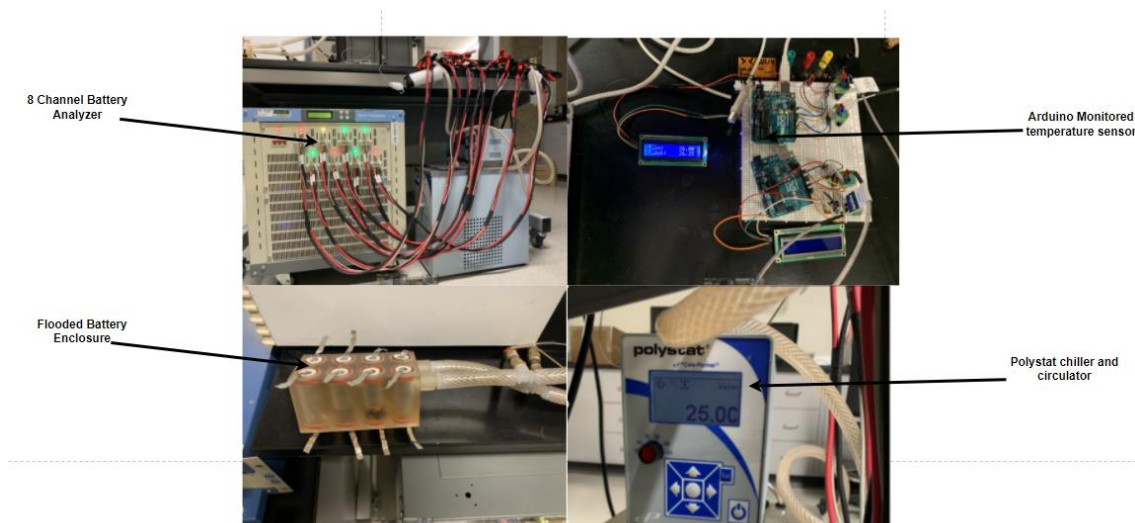


Figure 3.31. Battery aging cycler experimental setup.

Although the advertised capacity of the cells was around 3.5Ah, the experimental results showed that only 2.5Ah of charge capacity was attainable without compromising the safety of the cells. The cells were fast charged similar to previously described experiment in [59] at a constant current rate of 2C based on the advertised capacity, and the current, voltage and charge capacity were recorded while temperature was held constant. Figure 3.32 is a plot of the voltage during charge and discharge, Figures 3.33 is a plot of the current over the entire charge and discharge cycles, and Figures 3.34 and 3.35 describe the current and charge capacity plots for the CV region. In Figure 3.34 an exponential decay can be observed in current over time initially, however as the cells aged, the current gradient in the CV region became steeper. The cells were cycled for around 400 cycles, from Figure 3.35 it can be observed that the cell capacity started off at ~2500mAh during early cycles and depleted to ~2100mAh during the later cycles, similarly the initial exponential curve of the capacity during earlier cycles which then becomes a steeper and more linear as the cell ages.

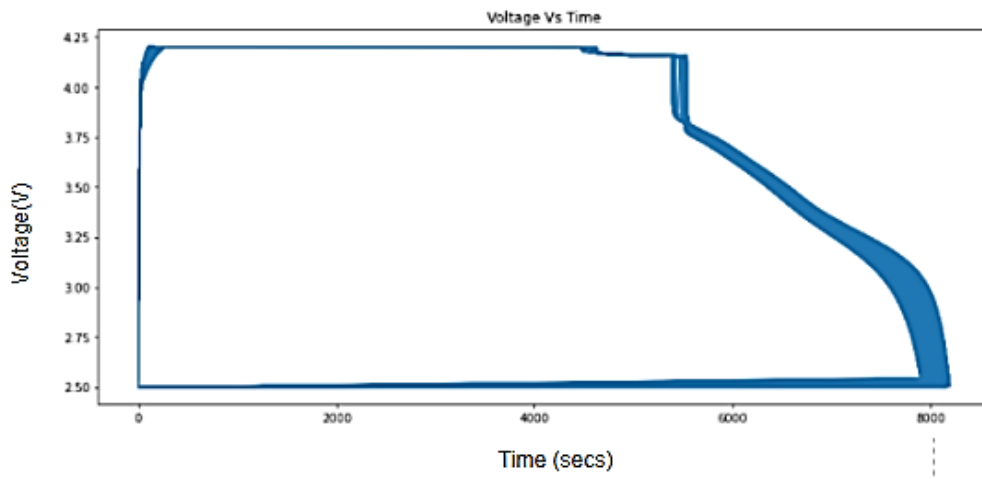


Figure 3.32. Panasonic Cell Voltage over time for charge and discharge cycles.

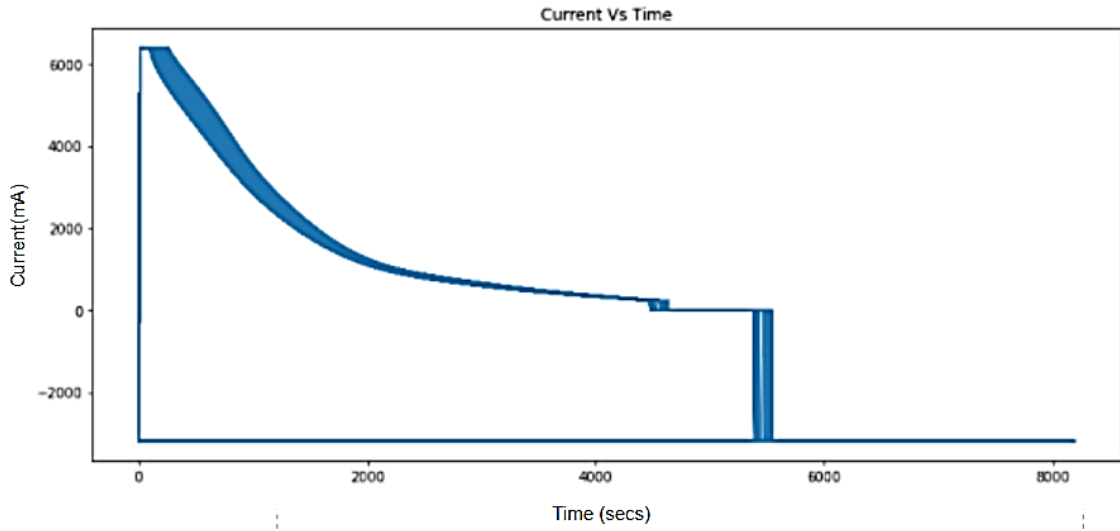


Figure 3.33. Panasonic Cell Current over time for charge and discharge cycles.

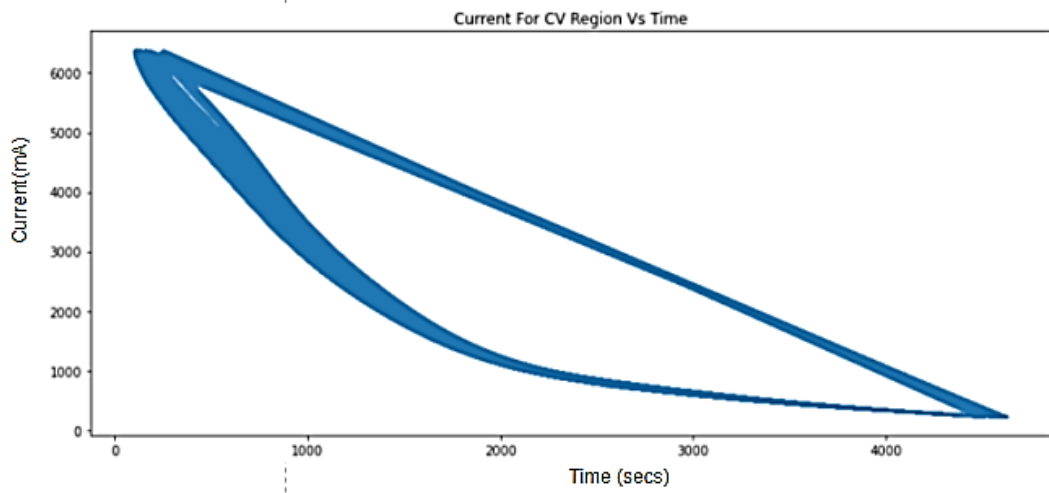


Figure 3.34. Panasonic cell current over time for CV region.

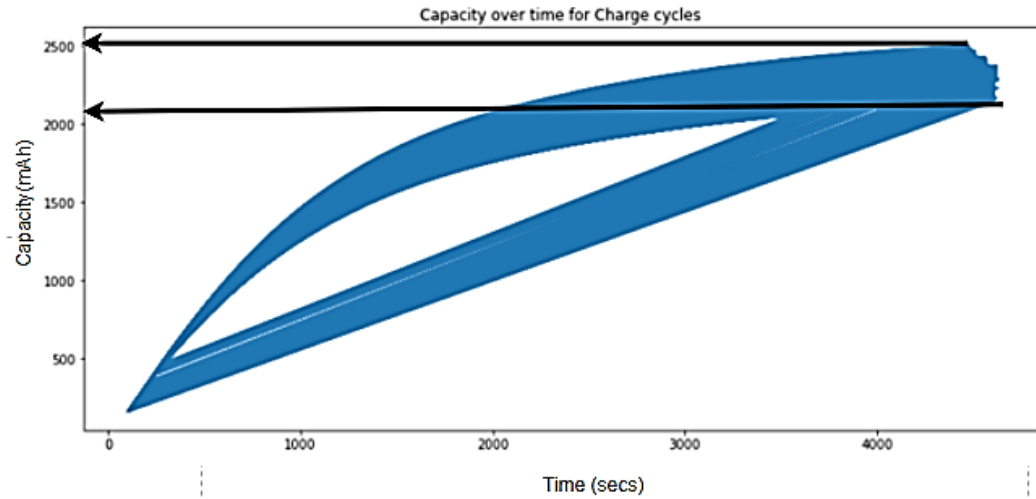


Figure 3.35. Panasonic cell capacity over time for CV region.

The gradients of the current curve in CV region at time $t+1$ were computed and plotted against the cycle indices in Figure 3.36. Similar to the results from the A123 cell experiments described in Figure 3.26, an exponential decay in the current gradients can be observed in the values of the gradient of the curves as the cells continue to age, further validating the robustness of this prediction methodology across multiple cell chemistries and duty cycles.

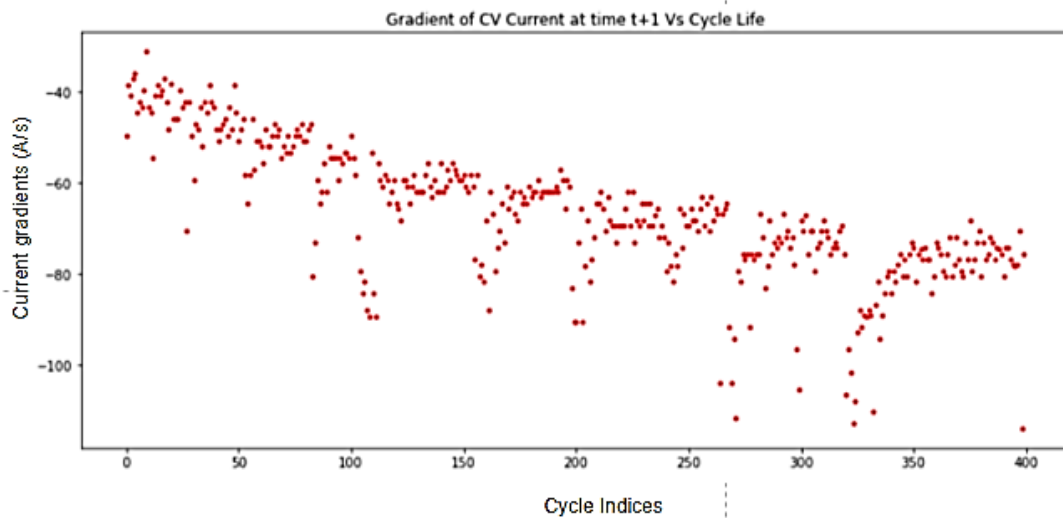


Figure 2.36. Panasonic cell current gradients against cycle indices.

3.6.2. Deep Neural Network SOH Estimation

Based on the experimental observation of current gradients as indication of battery capacity and SOH, a deep neural network model of the data recorded during the aging studies of the A123 battery cells was conducted. The A123 cell data was selected due to the volume of data collected given that over 100 cells were cycled, representing a decent sample size.

A deep neural network DNN model was developed and trained using the deep learning keras framework. Data recorded from 45 of the A123 cell ageing experiments previously described were used as training and test data. The details of the DNN development can be found in the Appendix A of this work. Table 3.4 is a description of the data inputs for the DNN model, where current gradient and CV time represent the gradient of the current curve computed for each cycle at the transition to CV charging and the time taken for the CV portion of the charge, respectively. Capacity indicates the charge capacity of each individual cell during each charge cycle representing the prediction output of the model. Note that the current gradient values are normalized for ease of modeling.

Table 3.4. Description of DNN data and statistics

	count	mean	std	min	25%	50%	75%	max
Current_Gradients	50,949.00	0.26	0.04	0.07	0.24	0.26	0.29	0.44
CV_Time	50,949.00	6.30	1.24	1.36	5.34	6.29	7.26	9.94
Capacity	50,949.00	1.03	0.04	0.88	1.01	1.04	1.06	1.08

Figure 3.37 is a plot of the resulting predictions for 1000 randomly sampled data points from the pool of test data that was excluded from the training dataset of DNN model. From the plot we can observe the model's ability to accurately predict the cell SOH/Capacity given any current gradient inputs.

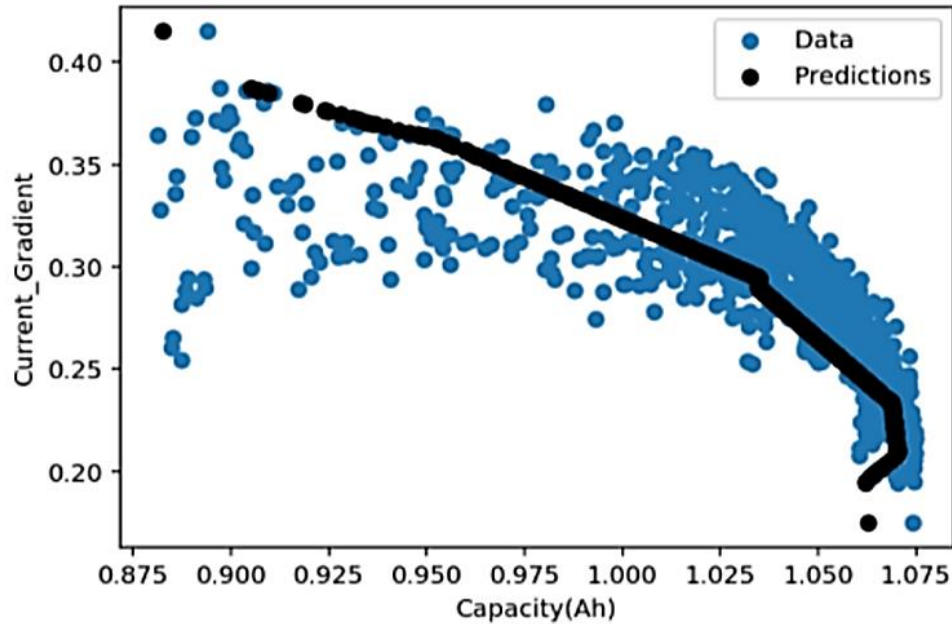


Figure 3.37. Deep Neural Network Model prediction of SOH.

The input of the model is the gradient of the CCCV charge curve transition and the output of the model is the capacity of the cell at the time of charge, representing the cell SOH. This model can be embedded easily into the on-board BMS and be used to estimate the battery SOH quickly and accurately during charging operations.

CHAPTER FOUR

Modular Connected Battery Pack, Battery Swapping Station and Vehicle to Grid

Traditional EVs contain a large battery energy storage system (BESS) as the source of power for the vehicle propulsion system. The battery pack is typically 50–100 kWh in capacity, costing thousands of dollars and has an adverse effect on the weight of the vehicle. However, studies have shown that the typical daily drive cycle for the average consumer is approximately 40 miles (64 km) for 95% of their drive cycles, corresponding to about 15 kWh capacity requirement for daily driving. A universal battery pack (UBP), referred to in this work, is designed as an alternative to the traditional battery pack. It has a highly reduced weight and can charge more quickly than conventional packs, it also has the capability of being able to be combined with multiple packs within an EV when a longer range is necessary. In addition, the battery packs are also connected through internet of things (IoT) to a cloud-based network to constantly manage the battery state of health (SOH), state of charge (SOC), and broadcast its various data points with the Battery Swapping Station and the Battery Sharing Network. Figure 4.1 is a diagram of the new battery placement architecture proposed inside of an EV. As seen in the figure, the battery pack in the front of the vehicle is designed to be a custom battery pack that could be permanently part of the vehicle or also be UBP that is swappable depending on the use case/application. This greatly reduces the load demand that the EV owner puts on the grid as the battery can be charged over a long stretch of time at night when load is minimal, and the electricity is cheaper. The UBP slot in the

vehicle is designed to provide the EV owner flexibility to participate in the Battery swapping network. The pack and collection frame are standardized to fit any vehicle built with a traditional ladder frame and capable of providing a range of 50 - 200 miles or more depending on vehicle weight, duty cycle and vehicle dynamics. The battery packs are available on demand at a Battery swapping network discussed in this chapter. Figure 4.2 is a description of the connected UBP. The UBP is modular and consists of high voltage (HV) connectors, optional low voltage (LV) connectors, a coolant connectors for thermal management (if pack is liquid cooled), and an IoT enabled, embedded device for intelligent on-board diagnostics and control of the battery pack also known as the Battery Management System (BMS) described in the previous chapter.

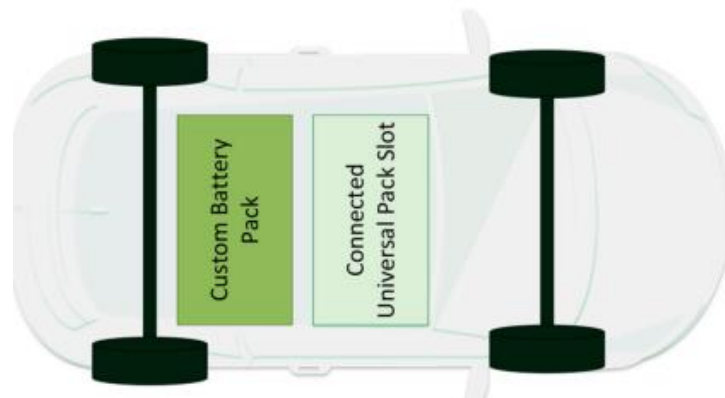


Figure 4.1. Novel Electric Vehicle Architecture with Custom Battery Pack and Universal Battery Pack Slot.

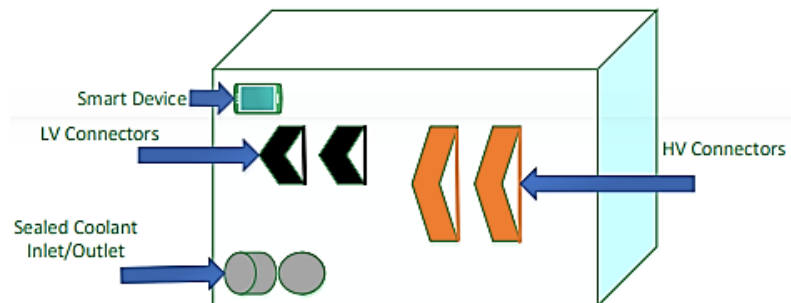


Figure 4.2. Universal Battery Pack Design.

Figure 4.3 is a CAD model of the UBP during the modeling and design phase of the prototype, Figures 4.4 and 4.5 are pictures of the a UBP during the design and fabrication phase.

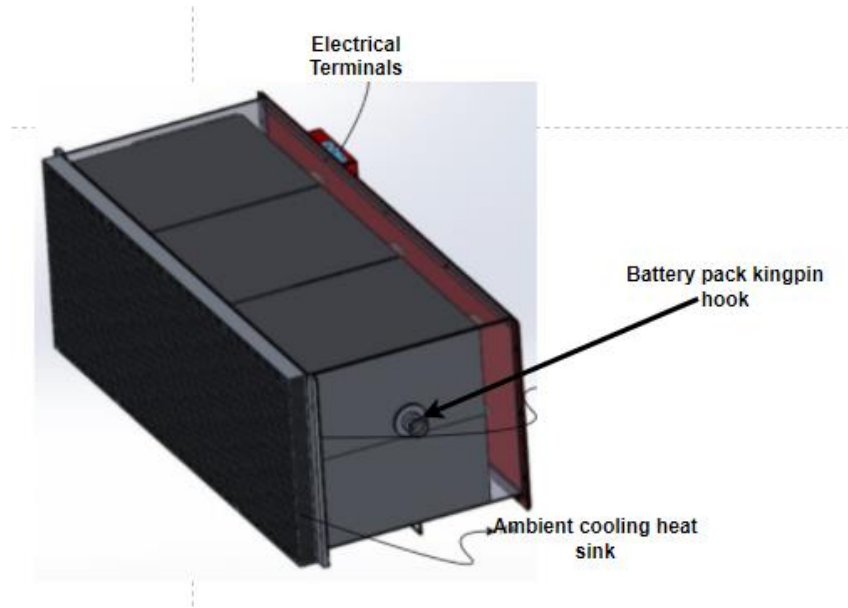


Figure 4.3. A CAD Model of UBP.

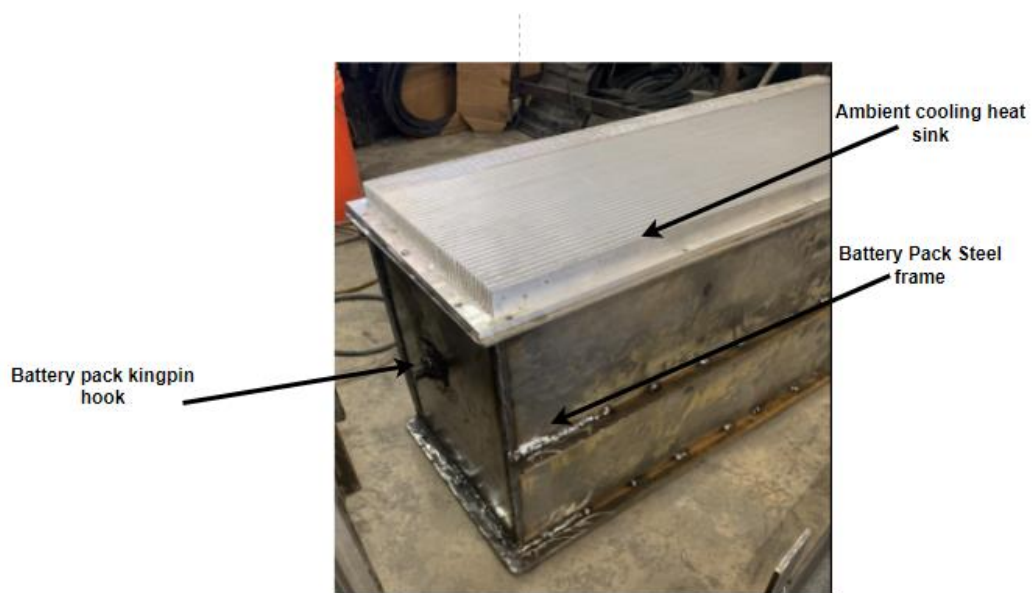


Figure 4.4. Fabrication of UBP.

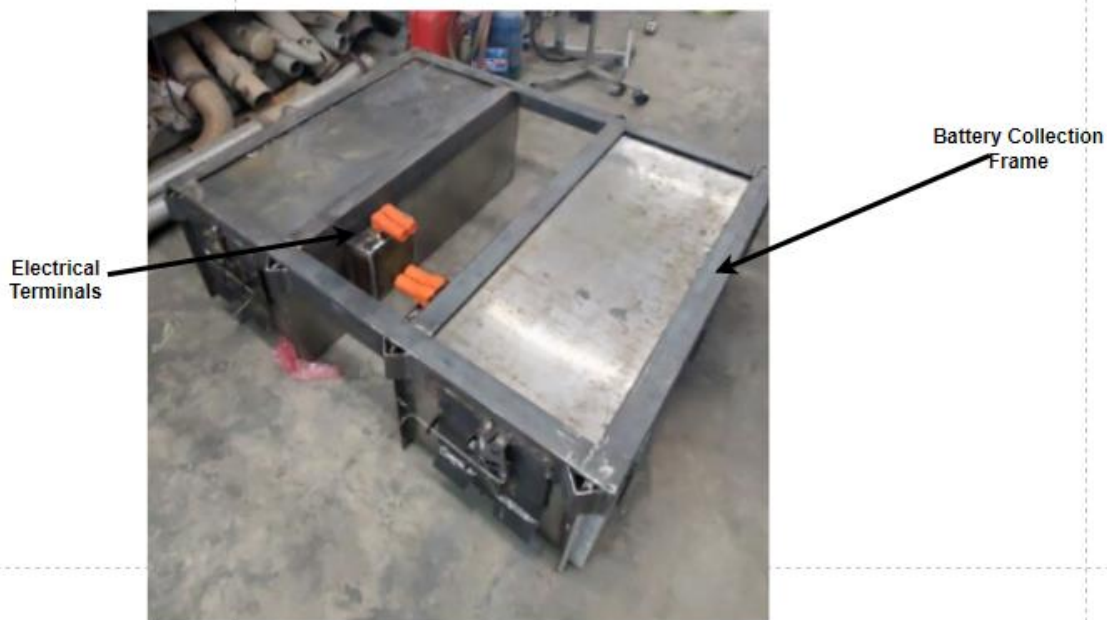


Figure 4.5. Two UBPs embedded inside of a battery collection frame.

4.1. Battery Cooling Systems

Battery energy management and thermal design is a primary factor with regards to performance and life cycle of an EV battery [54]. Li-ion batteries should ideally operate between 25 °C and 40 °C for optimal life and performance. Using air as a heat transfer medium, as in the validation prototype build described in Figure 4.4, is a cheap and simple method for battery cooling; however, it is sometimes inefficient in comparison to liquid cooling. Some of the limiting factors of air cooling in EVs are limited flow rate of cooling air, noise, inhomogeneous temperature distribution within batteries, flow rate of cooling air, and dependence on vehicle cabin air temperature. Due to the strict temperature operational range of Li-ion battery packs, Li-ion batteries in EV applications are typically liquid cooled, however these systems are more costly and complex to implement. The thermal management responsible for cooling of an EV battery pack

typically consists of a refrigerant system, a radiator, heater, pump, coolant reservoir, cold plates, coolant hoses and valves, temperature sensors and a controller. Figures 4.6 and 4.7 are block diagrams of a typical EV battery pack and all of its subcomponents modeled in MATLAB/Simulink.

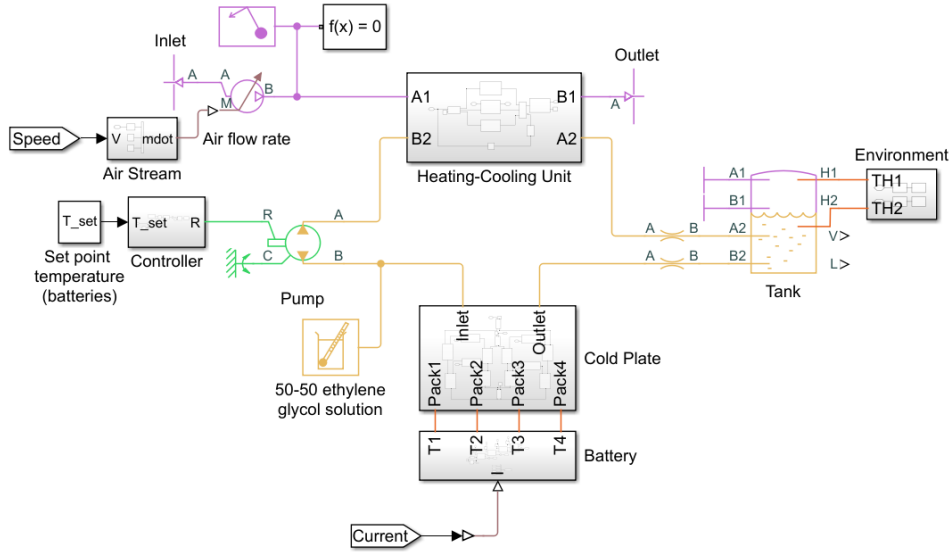


Figure 4.6. Battery cooling system overview.

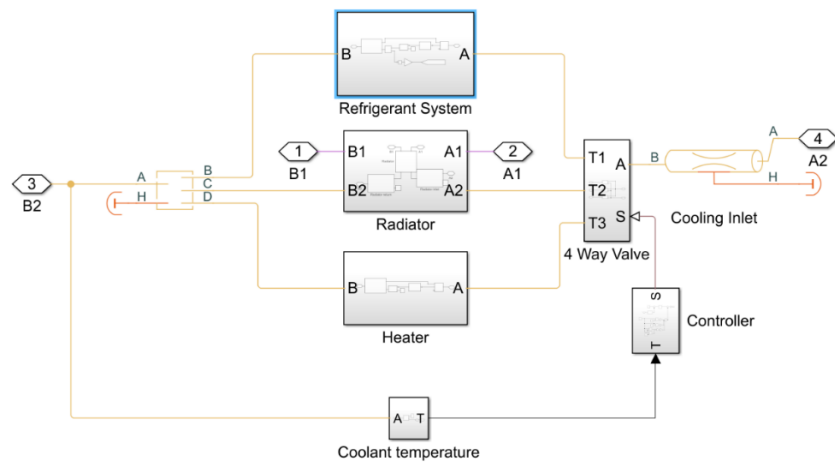


Figure 4.7. Heating and cooling unit subsystem detail.

The temperature sensors, control system, and cooling plates are typically embedded within the battery pack itself while the heating/cooling unit which consists of the refrigerant system, radiator and heater are typically outside of the battery pack and on-board the vehicle due to packaging complexity and the need for other systems within the vehicle to share some of the components such as cabin heating and cooling, motor and power electronics heating and cooling.

In battery swapping and Vehicle-to-Grid (V2G) applications however, it is desirable for all of the cooling components, needed to keep the battery pack within its optimal temperature, to be on-board the battery pack itself. This reduces the complexity of dealing with coolant connections and spillage and improves the standardization and flexibility of the battery packs. Therefore, a novel battery pack design is proposed which integrates a coolant pump, radiator, fans, coolant hose and valves with controller and cold plates all within the battery pack as illustrated in Figure 4.8.

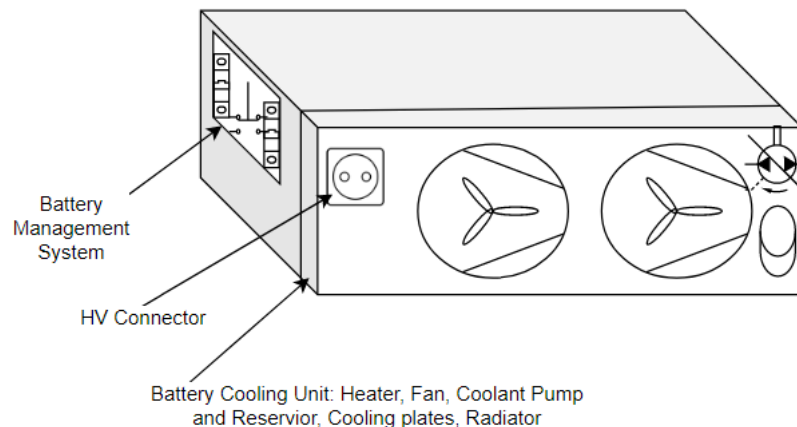


Figure 4.8. Closed loop Cooled Battery Pack.

The battery pack described can function in certain environments and with certain chemistries that have a wider range of temperature operations when a refrigerant system is not needed. For heating the battery in extreme cold weather or during a cold start, a thermoelectric heater or heat pump may be used inside the battery cooling unit. These batteries can be relied on in areas with modest weather and temperature or with chemistries such LiFePo or Lithium Titanate Oxide which have a wider temperature operating range.

4.2. Onboard Bidirectional Charger

An onboard bidirectional charger within a battery pack can be very useful in V2G applications of EVs both on-board and off-board the vehicle. The bidirectional charger on-board the vehicle can assist in providing vehicle to grid when the vehicle is plugged in at a Level 1 or 2 charger, when the battery pack is used in standalone stationary applications, or when the battery is used out in the field at mobile battery swapping stations that are not equipped with chargers or in remote locations for battery to battery (B2B) or vehicle to vehicle charging (V2X). These ranges of bidirectional applications call for a modular battery charger that is embedded within a battery pack itself. Figure 4.9 is a block diagram of the on-board bidirectional charger and operation.

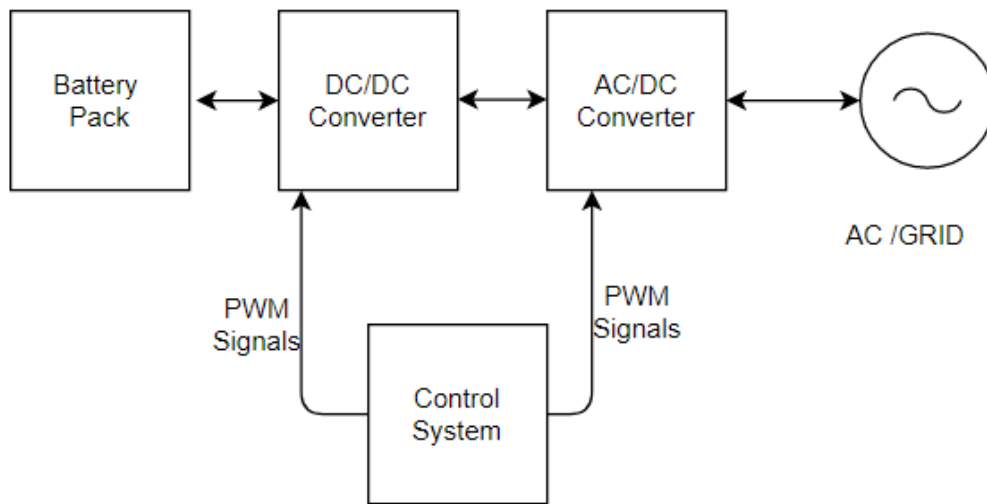


Figure 4.9. Onboard Bidirectional Charger Block Diagram.

The on-board bidirectional charger within a battery pack consists of a bidirectional DC/DC converter, isolating transformer between the DC converter and AC converter, a full-bridge AC/DC converter which consists of power semiconductor switching devices such as wide band gap switching devices made of SiC or GaN material, an EMI filter composed of an inductor and capacitor. It also contains a control system responsible for measurements of battery voltage, current, bus voltage, power grid voltage and current, and gate drivers for PWM switching of the power electronics components. The DC/DC converter is controlled through a duty cycle phase shift while the AC/DC converter is controlled through pulse width modulation (PWM) switching. The use of wide band gap components allows for high power density and efficiency, reducing the physical footprint of the charger within the battery pack and allowing for reduced weight and cooling requirements of the charger.

4.3. Swappable Electric Vehicle Chassis.

A modular swappable EV chassis is described in Figure 4.11. The swappable chassis allows for a variety of vehicle body platforms to be combined with the same EV chassis. The swappable EV chassis features the electric powertrain, battery collection frame and modular battery pack described thus far. It also incorporates a steering rack motor that can be controlled wirelessly through a steering wheel sensor, a wireless embedded controller for controlling the electric motor and braking system through wireless signals from the throttle and brake pedal on board the interchangeable vehicle body. Finally, the swappable EV chassis described allows for wireless selection of drive modes and gears from a wireless gear selector aboard an interchangeable vehicle body. The swappable chassis opens up the opportunity for different class and utilities as described in Figure 4.10 to be used in conjunction with the same vehicle body.

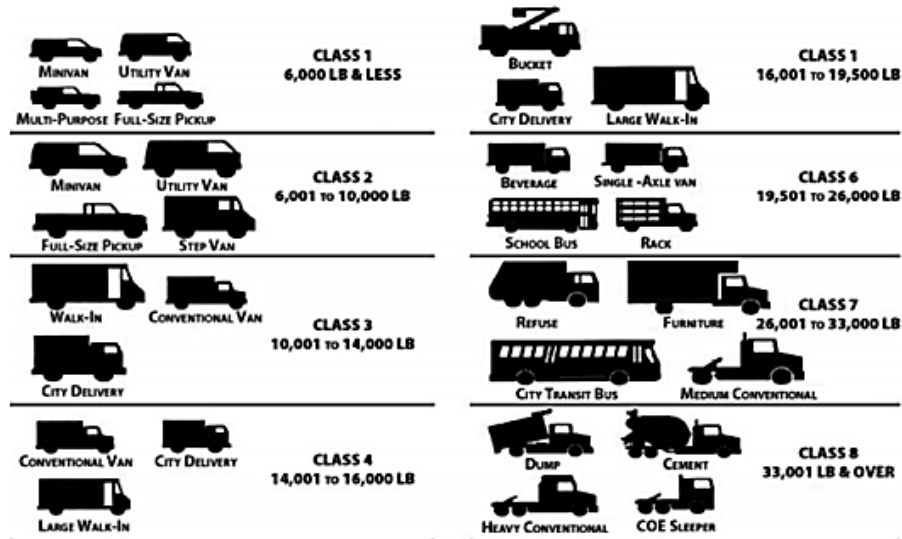


Figure 4.10. Vehicle Body styles and classes for swappable chassis

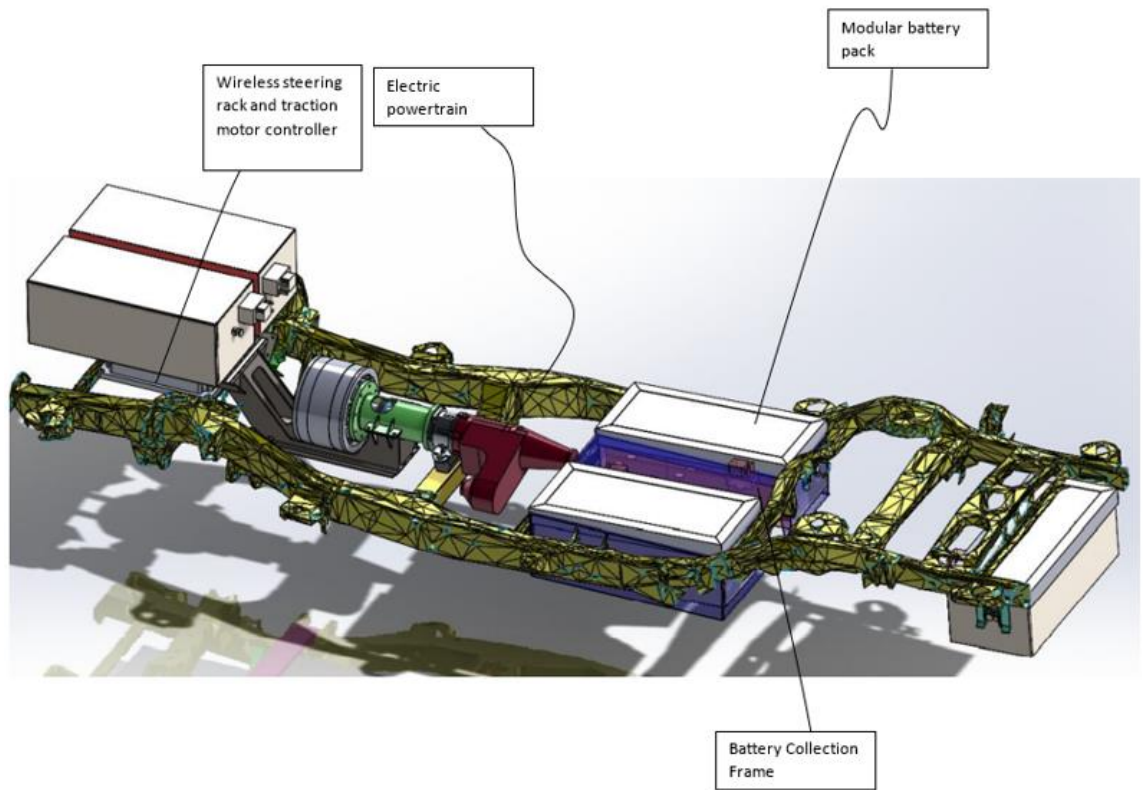


Figure 4.11. Swappable Electric vehicle chassis.

4.4. Battery Swapping Network and V2G System

The battery swapping station is an integral part of the battery swapping network and consists of mechanical, structural, and electrical components. Figure 4.12 is a conceptual high-level description of the BSS.

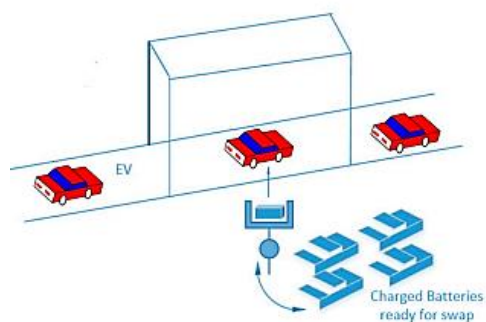


Figure 4.12. Conceptual design of a Battery Swapping Station.

The structural components of a mobile BSS include a vehicle platform, battery and/or vehicle lift, vehicle alignment guides, electrical alignment guides, battery conveyor mechanisms, battery storage racks and battery rails for retrieval of charged batteries and addition of depleted batteries. Figure 4.13 highlights the components inside of a battery swapping station built to operate battery swapping for the vehicle architectures discussed in the previous chapters.

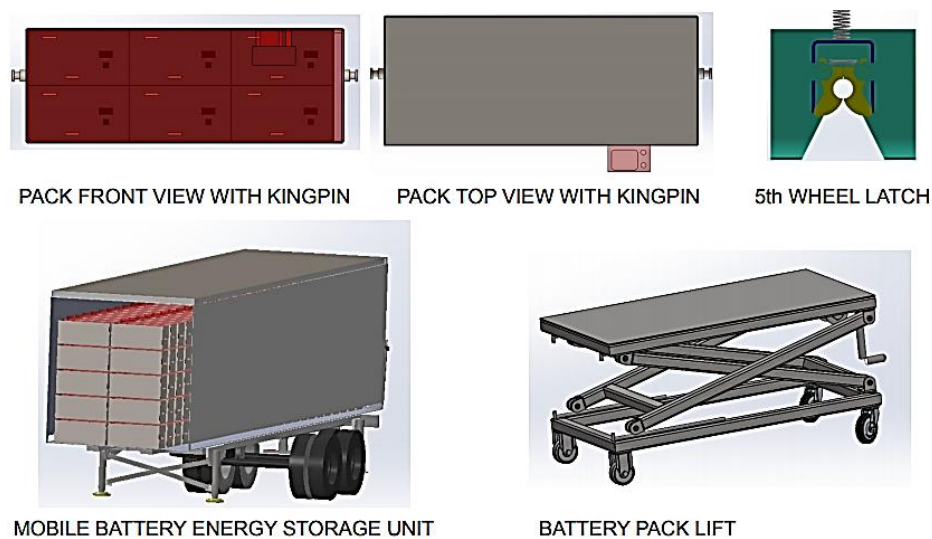


Figure 4.13. Mobile Battery Swapping Station Components.

When a vehicle arrives at a swapping station for a swap, the vehicle climbs onto a ramp, the depleted battery pack is removed from the vehicle by placing the battery pack lift underneath the vehicle, raising the height of the lift until it meets the guides on the vehicle, releasing the spring loaded latch so that the weight of the pack is now supported by the lift, then lowering the lift, and inserting the depleted pack inside an empty slot on the battery storage unit. Following the removal, a charged battery pack is rolled out of the battery storage unit and placed on the battery pack lift, the battery is then slid underneath the vehicle with the battery pack lift and guided into the vehicle again through the guides

on the vehicle, finally the battery is raised upwards until the battery pack is latched securely onto the vehicle.

4.5. Electrical Design of BSS and V2G Implementation

In today's implementation, the BSS is heavily dependent on the distribution grid and represents new high-power consumption loads for the distribution system operators. The electrical components of the BSS are mainly composed of a distribution transformer, AC/DC chargers, battery packs, and a battery energy control module (BECM). Figure 4.14 is a block diagram of the electrical relationship between the components of the BSS. The distribution grid provides the AC power at the distribution voltage level, and because of the high-power demand of the BSS [55], this voltage level will be between 33 kV and 11 kV. Charging power levels for EV battery packs range from Level 1 charging at 120 V/15 A single-phase; Level 2 Charging at 240 V (up to 80 A, 19.2 kW); and Level 3 Charging at 50 kW and up [56]. Depending on the size of the BSS and the voltage level available at the distribution grid, different charging modes can be implemented [57].

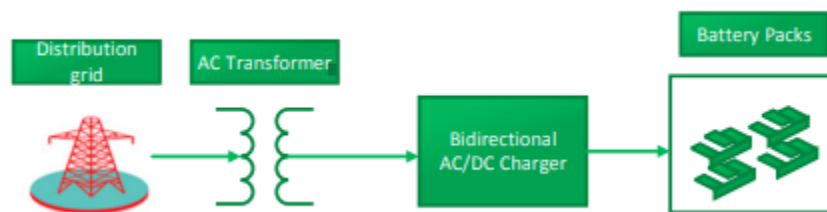


Figure 4.14. Electrical Design of BSS.

The current state-of-the-art implementation of BSS possesses several technical and economic challenges. Such challenges are the nonstandard battery interface across

EV manufacturers and consumer acceptance of not owning their battery or their original battery being tampered with and replaced with a lower performance battery during a swap. Another critical challenge is the heavy dependency of the BSS on the distribution grid, and the high-power demand of the BSS, which could have a negative impact on the grid during peak loading periods. In this work, a new design of the EV battery architecture has been proposed to achieve a common standardized modular battery interface across EV manufacturers. In addition, a renewable energy generation and a bidirectional AC/DC charging interface are introduced, which allows the BSS to become a service utility that supports the grid in terms of distributed generation and storage. A PV system is integrated with the BSS. In addition, a bidirectional AC/DC converter topology discussed in [56] is implemented allowing the battery packs in the BSS to provide V2G services to the smart grid. Figure 4.15 is a block diagram description of the system structure of the proposed BSS. The BSS is also a part of a network of BSS, referred to as a Battery Sharing Network (BSN), linked together through the IoT and telecommunication interfaces, communicating to optimize the cost of charging, reduces the waiting time for battery swaps by forecasting battery swaps and share the UBPs amongst each other through participating EVs and EV customers. The EV owners can participate in the BSN and transport battery packs from the BSS where they are located to the BSS where they are needed for incentives such as free battery swaps or payment. The UBPs are transported from BSS to BSS through the embedded UBP slot on optimized routes convenient for EV owners. This reduces, or eliminates, the need for dedicated vehicles for transportation of EV battery packs from station to station. Figure 4.16 is a conceptual illustration of the BSN. The BSN consists of several functional subsystems;

the communication between these systems is handled by the BSN Management System. This system coordinates the bidirectional flow of power between the BSS and the smart grid which is designed for distributed generation and bidirectional power flow. It also coordinates the optimized routing of boost packs in the BSN through the EVs that participate in the network. This complex system is achieved through a cloud-connected intelligent system of sensors across the BSN and an AI/ML framework running on the cloud to optimize the system. In addition, the BSN management system controls the scheduling of battery swaps as well as forecasting of future swaps and grid loading. The BSN management system in this proposed scheme becomes a grid utility, providing services to the grid, such as peak shaving and load balancing, and serves as a reserve for the grid during contingency situations.

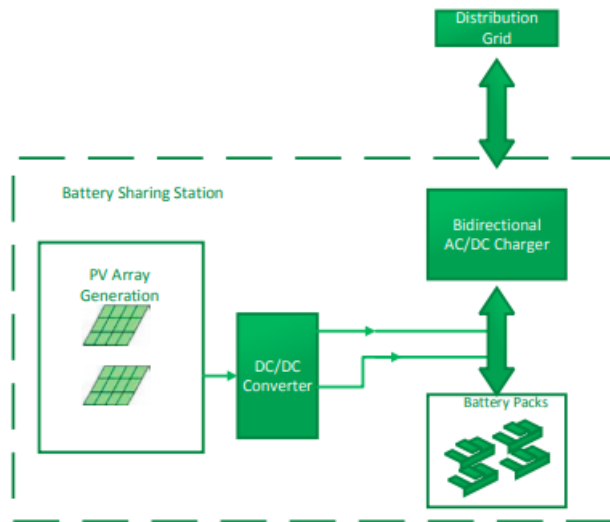


Figure 4.15. Battery Swapping Station with local renewable energy generation and bidirectional charger.

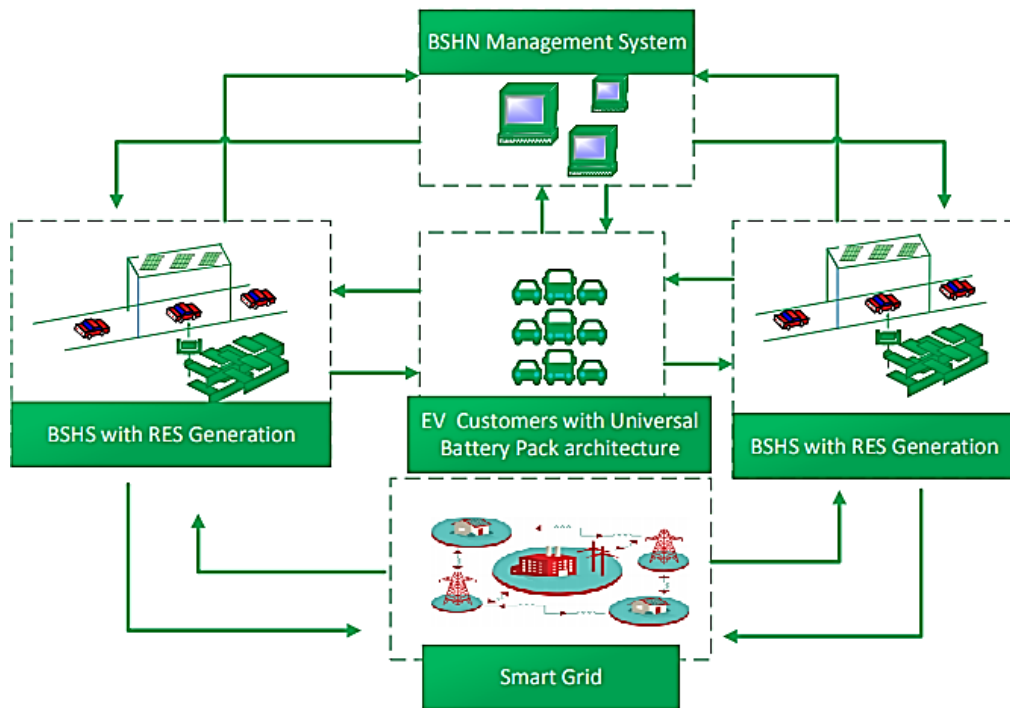


Figure 4.16. Battery Sharing Network (BSN) communication interface between Battery Sharing Station (BSS) and smart grid.

4.6. Battery Sharing Network Charge Management System

Coordination of logistics for mobile battery energy storage systems requires careful design and state of the art connectivity tools [58]. The cloud connected battery sharing network management platform sometimes referred to as the charge management system (CMS) is responsible for monitoring batteries, swappable EV chassis, swapping/charging infrastructure and the fleet of EV/AV across the network. It is divided up into several modules including the scheduling/routing module, charging/discharging module, billing and payments modules, control module, data acquisition and monitoring modules, data analytics modules and data storage module. It receives inputs such as vehicle/battery health, battery state of charge, battery location and size, vehicle telematics data,

electricity load and price forecasts, charging/discharging status, equipment alerts and many more. From the real-time inputs and analytical models deduced from the analytics modules, the management systems can make decisions on battery/vehicle chassis swap scheduling and routing, battery charging/discharging, mobile battery swapping station assignment and routing and many more optimization and control functions. Figure 4.17 is an architectural diagram of the cloud management system.

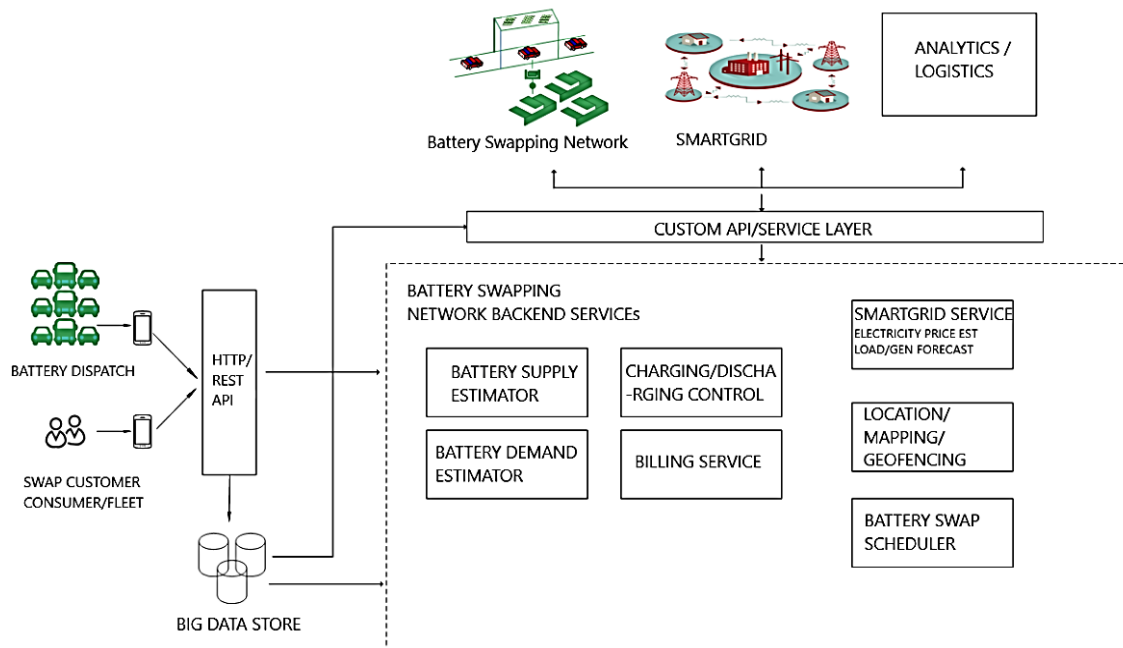


Figure 4.17 Architectural diagram of CMS.

CHAPTER FIVE

Conclusion and Future Work.

In this work, an EV modeling approach was described and simulated in MATLAB, followed by tuning and validation on an EV chassis dynamometer testbed. The design philosophy of EV OEMs with regards to vehicle efficiency drive cycle tests, mandated by the EPA, were briefly described. The results of the EV model were validated by comparing them to the results of vehicle performance tests of the specified EV on a chassis dynamometer. The energy efficiency results of the modeled high-performance EV compared to the real-world vehicle showed close correlation with a root-mean-square error (RMSE) value of 0.2. The vehicle speed and vehicle distance traveled of the models also resulted in negligible error values.

A high-fidelity electrical model with thermal dependence of an EV battery cells was parameterized and modeled in MATLAB using the Parameter Estimation Toolbox. The cell model was extended into a vehicle pack model and a corresponding BMS was modeled. The modeling results highlighted the thermal asymmetry among cells models within the battery pack and described how the BMS was able transition between different pack operation states with adequate precision.

This importance of EV modeling, simulation, and validation is critical due to the revolutionization of the transportation industry by electric mobility. The topics from this work demonstrate the methodologies for developing high performance EV models in a software simulation environment and validating the models with real-world hardware in a

repeatable and scalable fashion, thereby enabling the rapid development of EV testbeds. A brief review of EV modeling techniques and software toolsets were introduced. A summary of EV motion dynamics was described mathematically and an equation based EV model was implemented based on the mathematical models described. Future work will consider a physical modeling approach which enables the development of an advanced motor model such as data driven/map based motor models, and advanced motor controller schemes such as six-step control or space vector modulation (SVM) controls which should result in more detailed and accurate transient and dynamic responses compared to the real-world vehicle. A physical modeling approach would also include more advanced battery models that consider the thermal relationship between individual cells within a pack and ambient temperature conditions, as well as degradation mechanisms that affect state of power (SOP) and state of health (SOH) during drive cycles simulations.

An EV powertrain comprising of one motor that can produce rotational power to multiple axles and wheels of vehicle independent of each other was designed and implemented. Also described is a battery sharing network which is a distributed network and comprises of one or more battery swapping stations and electric or autonomous vehicles that participate in the network. A cloud connected battery sharing network management system is described, which is capable of monitoring, control, routing and dispatch of batteries, vehicles, chargers, EVs, autonomous vehicles, and other assets within the network.

A battery collection frame capable of attaching and detaching an EV battery of varied configuration, shape and size was designed and implemented, where a latch frame

assembly which forms a part of a battery collection frame, is designed to accept a battery pack with kingpins and align the battery pack and its connections to the vehicle chassis and secure the battery pack to a vehicle chassis during driving was also designed and implemented. A closed-loop cooled battery pack which could be comprised of a fan, pump, refrigerant cooling system, radiator and condenser, cooling plate, coolant hoses, coolant reservoir, heater core or heat pump all embedded within the battery pack without a need for external cooling inlet and outlet channels was also described in detail.

A connected battery management system capable of sensing, balancing, charge and discharge protection, state and parameter estimation and wireless communication of pack, module or cell states and parameters was modeled and simulated in MATLAB where a bidirectional charger topology was described for robust implementation of on-board modular battery pack. A system and method for rapid determination of battery state of health based on a single charge cycle was investigated with experimental results. Finally, a deep neural network-based model for training and determining the state of health of a battery cell was developed and validated.

A detailed analysis of battery SOH and battery degradation mechanisms was presented. A method for rapid determination of battery SOH based on a single charge cycle was investigated and experimental results were validated. A deep neural network-based model for training and determining the state of health of a battery cell based on previously observed data was developed and validated. The data analysis showed a correlation between gradient of the current curve during transition between the CC and CV region of charge and the charge-discharge cycle count. The resulting deep neural network training model loss maximum value was 0.06. Future work will investigate how

different charging modes affect the SOH estimation principles. Such charging modes include DC Fast Charging (DCFC), Constant Current (CC) and Step charging and other optimized charging methods. In addition, the effects of calendar aging on accuracy of this method SOH estimation need to be further investigated as well.

Future work on the EV prototype testbed developed in this work will include the performance and efficiency testing of the developed EV powertrain on a chassis dynamometer similar to the Chevrolet Bolt EV tests described in Chapter Two of this work. A wireless electric motor steering rack controller and wireless traction motor controller on-board the swappable EV chassis capable of wireless connection with the wireless throttle, brake and steering onboard an interchangeable vehicle body that can be attached to the swappable chassis described in Chapter Four of this work will also be a future topic worth investigating.

APPENDIX

APPENDIX A

A Deep Neural Network Model in Jupyter Notebook

Deep Neural Networks are Artificial Neural Networks with more than one layer between the inputs and the outputs of the network. This appendix includes the code blocks written in python scripting language inside of a Jupyter notebook (data science toolbox) for modeling a deep neural network of battery SOH, with an input of current gradient during the CCCV region and output of predicted capacity as a function of SOH.

```
In [2]: import h5py
import scipy.io
import matplotlib.pyplot as plt
import pickle
import warnings
from pprint import pprint
import numpy as np
from scipy.interpolate import interp1d
from scipy.signal import savgol_filter
from scipy.misc import derivative
```

```
In [3]: #Load matlab data file and convert to python data type
```

```
matFilename = '2018-04-12_batchdata_updated_struct_errorcorrect.mat'
f = h5py.File(matFilename)
```

```
<ipython-input-3-08facd5e4e14>:4: H5pyDeprecationWarning: The default file mode will change to 'r' (read-only) in h5py 3.0. To suppress this warning, pass the mode you need to h5py.File(), or set the global default h5.get_config().default_file_mode, or set the environment variable H5PY_DEFAULT_READONLY=1. Available modes are: 'r', 'r+', 'w', 'w-'/ 'x', 'a'. See the docs for details.
  f = h5py.File(matFilename)
```

```

In [4]: #Set Up Data as iterable dictionaries

keys = list(f.keys())
print(keys)
batch = f['batch']

num_cells = batch['summary'].shape[0]
bat_dict = {}
for i in range(num_cells):
    cl = f[batch['cycle_life']][i,0].value
    policy = f[batch['policy_readable']][i,0].value.tobytes()[::2].decode()
    summary_IR = np.hstack(f[batch['summary']][i,0]['IR'][0,:].tolist())
    summary_QC = np.hstack(f[batch['summary']][i,0]['QCharge'][0,:].tolist())
    summary_QD = np.hstack(f[batch['summary']][i,0]['QDischarge'][0,:].tolist()
    ())
    summary_TA = np.hstack(f[batch['summary']][i,0]['Tavg'][0,:].tolist())
    summary_TM = np.hstack(f[batch['summary']][i,0]['Tmin'][0,:].tolist())
    summary_TX = np.hstack(f[batch['summary']][i,0]['Tmax'][0,:].tolist())
    summary_CT = np.hstack(f[batch['summary']][i,0]['chargetime'][0,:].tolist()
    ())
    summary_CY = np.hstack(f[batch['summary']][i,0]['cycle'][0,:].tolist())
    summary = {'IR': summary_IR, 'QC': summary_QC, 'QD': summary_QD, 'Tavg':
    summary_TA, 'Tmin': summary_TM, 'Tmax': summary_TX, 'chargetime':
    summary_CT,
    'cycle': summary_CY}
    cycles = f[batch['cycles']][i,0]
    cycle_dict = {}
    for j in range(cycles['I'].shape[0]):
        I = np.hstack((f[cycles['I']][j,0].value))
        Qc = np.hstack((f[cycles['Qc']][j,0].value))
        Qd = np.hstack((f[cycles['Qd']][j,0].value))
        Qdlin = np.hstack((f[cycles['Qdlin']][j,0].value))
        T = np.hstack((f[cycles['T']][j,0].value))
        Tdlin = np.hstack((f[cycles['Tdlin']][j,0].value))
        V = np.hstack((f[cycles['V']][j,0].value))
        dQdV = np.hstack((f[cycles['discharge_dQdV']][j,0].value))
        t = np.hstack((f[cycles['t']][j,0].value))
        cd = {'I': I, 'Qc': Qc, 'Qd': Qd, 'Qdlin': Qdlin, 'T': T, 'Tdlin': Tdlin,
        'V': V, 'dQdV': dQdV, 't': t}
        cycle_dict[str(j)] = cd

    cell_dict = {'cycle_life': cl, 'charge_policy': policy, 'summary': summary,
    'cycles': cycle_dict}
    key = 'b1c' + str(i)
    bat_dict[key] = cell_dict

```

```
In [45]: #Plot over time at Constant Voltage Charging Condition first 100 Cycles
```

```
# X input to ANN model, Y output of ANN model for SOH estimation
x_dIdt = []
x_CV = []
Y = []
battery_cycle_SOH = {}
battery_cycle_SOH = dict.fromkeys(bat_dict.keys())

for key in bat_dict.keys():

    cycles = bat_dict[key]["cycles"]
    # fig, ax = plt.subplots(nrows=2, ncols=2, figsize=(30, 20))
    battery_cycle_SOH[key] = dict.fromkeys(cycles.keys())

    # b1c43_resampled = {}
    # cycle_dict = {}
    #Function for 3rd order polynomial fit of gradient curve

    def f(x):
        return c1*x**2 + c2*x + c3
    for cycle_ind,cycle in enumerate(cycles.values()):

        I = cycle["I"]
        Qc = cycle["Qc"]
        T = cycle["T"]
        V = cycle["V"]
        t = cycle["t"]

        cond1 = V >= 3.6 #Constant Voltage charging
        cond2 = I > 0 #Only positive current indicating charging
        cond3 = I < 1 #Only cells that make it to the 1C CV region
        cond4 = cond1 & cond2 & cond3 #Combine both conditions

        Icond = I[cond4]
        tcond = t[cond4]

        z = np.polyfit(tcond,Icond, 2)
        c1 = z[0]
        c2 = z[1]
        c3 = z[2]

        dt_CV = tcond[-1] - tcond[0] # Time of discharge

        dt = tcond[0] + 1

        dIdt = derivative(f,dt) #Gradient of the curve

        battery_cycle_SOH[key][str(cycle_ind)] = [dIdt,dt_CV,Qc[-1]]

        #battery_cycle_SOH[key][cycle_ind] = [dIdt,dt_CV,Qc[-1]]

        #Create variables for polyfit plot
    # poly = np.poly1d(z)
```

```

#         new_x = np.linspace(tcond[0],tcond[-1])
#         new_y = poly(new_x)

#         ax[0][1].plot(t[cond4], I[cond4])
#         ax[0][1].set_title("Current")

#         ax[0][0].plot(t, V)
#         ax[0][0].set_title("Voltage")

#         ax[1][0].plot(Qc[-1], dIdt, marker='o', markersize=3, color="red")
#         ax[1][0].set_title("Gradient Over Cycle Life")

#         ax[1][1].plot( t, Qc)
#         ax[1][1].set_title(" Polynomial Curve fit of current for CV region")

x_dIdt.append(dIdt)
x_CV.append(dt_CV)

#         X.append(x_prime)
#         Y.append(Qc[-1])

```

In [99]: battery_cycle_SOH.keys()

Out[99]: dict_keys(['b1c0', 'b1c1', 'b1c2', 'b1c3', 'b1c4', 'b1c5', 'b1c6', 'b1c7', 'b1c8', 'b1c9', 'b1c10', 'b1c11', 'b1c12', 'b1c13', 'b1c14', 'b1c15', 'b1c16', 'b1c17', 'b1c18', 'b1c19', 'b1c20', 'b1c21', 'b1c22', 'b1c23', 'b1c24', 'b1c25', 'b1c26', 'b1c27', 'b1c28', 'b1c29', 'b1c30', 'b1c31', 'b1c32', 'b1c33', 'b1c34', 'b1c35', 'b1c36', 'b1c37', 'b1c38', 'b1c39', 'b1c40', 'b1c41', 'b1c42', 'b1c43', 'b1c44', 'b1c45'])

```

In [100]: fig, ax = plt.subplots(nrows=2, ncols=2, figsize=(30, 20))

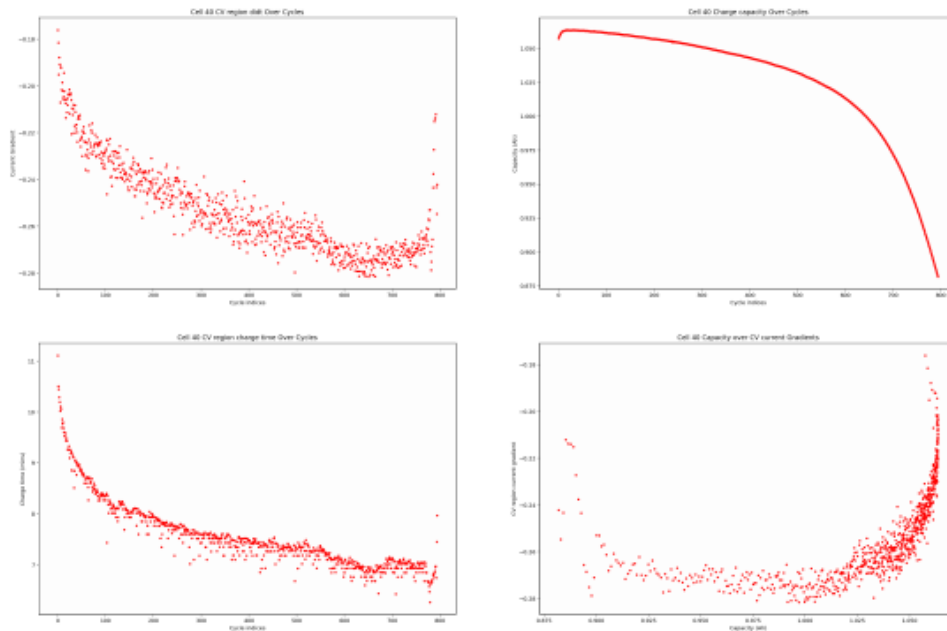
for indx, values in enumerate(battery_cycle_SoH['b1c40'].values()):
    # print(indx, values)
    if (values is not None):
        ax[0][1].plot(indx, values[2], marker='o', markersize=3, color="red")
        ax[0][1].set_title("Cell 40 Charge capacity Over Cycles")
        ax[0][1].set_xlabel("Cycle indices")
        ax[0][1].set_ylabel("Capacity (Ah)")

        ax[0][0].plot(indx, values[0], marker='o', markersize=3, color="red")
        ax[0][0].set_title("Cell 40 CV region didt Over Cycles")
        ax[0][0].set_xlabel("Cycle indices")
        ax[0][0].set_ylabel("Current Gradient")

        ax[1][0].plot(indx, values[1], marker='o', markersize=3, color="red")
        ax[1][0].set_title("Cell 40 CV region charge time Over Cycles")
        ax[1][0].set_xlabel("Cycle indices")
        ax[1][0].set_ylabel("Charge time (mins)")

        ax[1][1].plot(values[2], values[0], marker='o', markersize=3, color="red")
        ax[1][1].set_title("Cell 40 Capacity over CV current Gradients")
        ax[1][1].set_xlabel("Capacity (Ah)")
        ax[1][1].set_ylabel("CV region current gradient")

```



```

In [7]: #ANN Set Up for Softmax Regression
%matplotlib inline
%config InlineBackend.figure_format = 'retina'
import matplotlib.pyplot as plt
import pandas as pd

import numpy as np
import seaborn as sns
import warnings

warnings.filterwarnings('ignore')
pd.options.display.float_format = '{:,.2f}'.format
pd.set_option('display.max_rows', 100)
pd.set_option('display.max_columns', 200)

from __future__ import print_function
from datetime import datetime
from matplotlib.colors import ListedColormap
from sklearn.datasets import make_classification, make_moons, make_circles
from sklearn.metrics import confusion_matrix, classification_report, mean_squared_error, mean_absolute_error, r2_score
from sklearn.linear_model import LogisticRegression
from sklearn.utils import shuffle
from keras.models import Sequential
from keras.layers import Dense, Dropout, BatchNormalization, Activation
from keras.optimizers import Adam
from keras.callbacks import EarlyStopping
from keras.utils.np_utils import to_categorical
from sklearn.preprocessing import StandardScaler, LabelEncoder, OneHotEncoder, MinMaxScaler
from sklearn.model_selection import train_test_split, cross_val_score, StratifiedKFold, KFold
import keras.backend as K
from keras.wrappers.scikit_learn import KerasClassifier

```

```

In [55]: import tensorflow as tf

from tensorflow import keras
from tensorflow.keras import layers
from tensorflow.keras.layers.experimental import preprocessing

print(tf.__version__)

```

2.3.1

```

In [64]: #First Lets convert our data into a dataframe

data_lists = [x_dIdt,x_CV,Y]
df = pd.DataFrame(data_lists).transpose()
df.columns = ['Current_Gradients', 'CV_Time', 'Capacity']

```

```
In [65]: #View overall Statistics of data set
df.describe().transpose()
```

Out[65]:

	count	mean	std	min	25%	50%	75%	max
Current_Gradients	51,007.00	-0.26	0.04	-2.62	-0.29	-0.26	-0.24	0.10
CV_Time	51,007.00	6.30	1.28	0.62	5.34	6.29	7.27	40.13
Capacity	51,007.00	1.03	0.04	0.88	1.01	1.04	1.06	1.10

```
In [56]: # Make numpy printouts easier to read.
np.set_printoptions(precision=3, suppress=True)
```

```
In [66]: #Data cleanup to remove outliers and make gradients positive
df['Current_Gradients'] = df['Current_Gradients'] * -1
df = df[(df['Current_Gradients'] >= 0)]
df = df[(df['Current_Gradients'] < 1)]
df = df[(df['CV_Time'] < 10)]
df.describe().transpose()
```

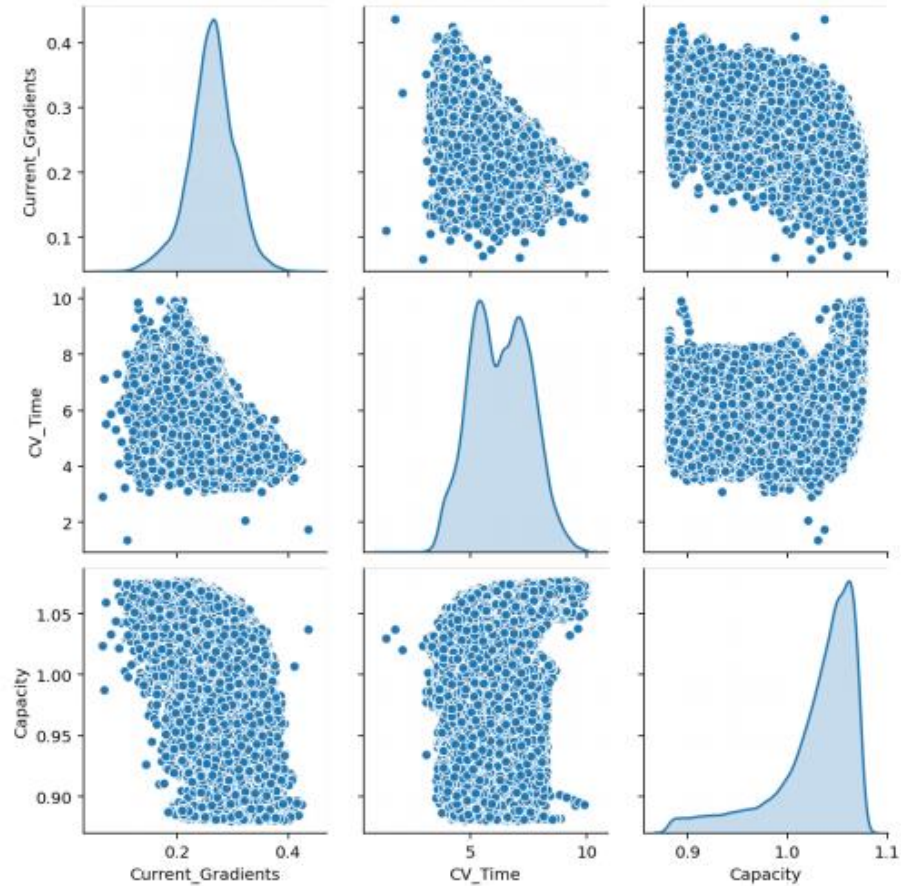
Out[66]:

	count	mean	std	min	25%	50%	75%	max
Current_Gradients	50,949.00	0.26	0.04	0.07	0.24	0.26	0.29	0.44
CV_Time	50,949.00	6.30	1.24	1.36	5.34	6.29	7.26	9.94
Capacity	50,949.00	1.03	0.04	0.88	1.01	1.04	1.06	1.08

```
In [67]: train_dataset = df.sample(frac=0.8, random_state=0)
test_dataset = df.drop(train_dataset.index)
```

```
In [70]: #Plot a description of the dataset
sns.pairplot(train_dataset[['Current_Gradients', 'CV_Time', 'Capacity']], diag_
_kind='kde')
```

Out[70]: <seaborn.axisgrid.PairGrid at 0x2247fb2b460>



```
In [71]: #Split the features from labels
train_features = train_dataset.copy()
test_features = test_dataset.copy()

train_labels = train_features.pop('Capacity')
test_labels = test_features.pop('Capacity')
```

```
In [72]: #Normalizing the data

normalizer = preprocessing.Normalization()
normalizer.adapt(np.array(train_features))
print(normalizer.mean.numpy())
```

[0.263 6.294]

```
In [73]: first = np.array(train_features[:1])

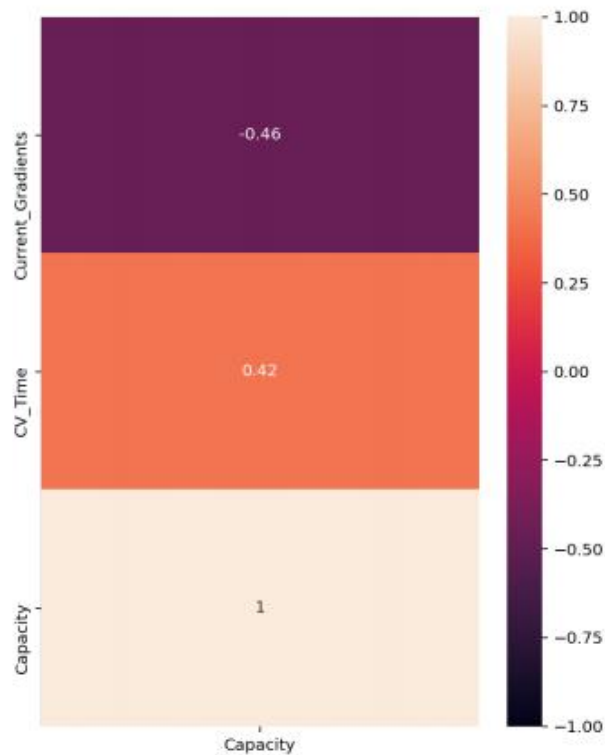
with np.printoptions(precision=2, suppress=True):
    print('First example:', first)
    print()
    print('Normalized:', normalizer(first).numpy())
```

First example: `[[0.25 7.79]]`

Normalized: `[[-0.36 1.21]]`

```
In [12]: #Correlation map
plt.figure(figsize=(6, 8))
sns.heatmap(df.corr()[['Capacity']], annot=True, vmin=-1, vmax=1)
```

Out[12]: `<matplotlib.axes._subplots.AxesSubplot at 0x2c87fd9cd60>`



```
In [75]: #Linear Regression Model
#Before building a DNN model we start with a simple regression model

#First we create the current gradients normalization Layer

current_gradient = np.array(train_features['Current_Gradients'])

current_gradient_normalizer = preprocessing.Normalization(input_shape=[1,])
current_gradient_normalizer.adapt(current_gradient)

#Then we build the sequential model

#This model will predict Capacity (Ah) based on current gradients
current_gradient_model = tf.keras.Sequential([
    current_gradient_normalizer,
    layers.Dense(units=1)
])

current_gradient_model.summary()
```

Model: "sequential"

Layer (type)	Output Shape	Param #
normalization_2 (Normalizati	(None, 1)	3
dense (Dense)	(None, 1)	2
Total params: 5		
Trainable params: 2		
Non-trainable params: 3		

```
In [76]: #Testing out the untrained model

current_gradient_model.predict(current_gradient[:10])
```

```
Out[76]: array([[ -0.261],
 [ 0.62 ],
 [-0.751],
 [-0.078],
 [ 1.793],
 [-0.311],
 [ 0.927],
 [ 0.537],
 [-0.245],
 [-1.034]], dtype=float32)
```

```

In [79]: #Once the model is built, we now compile the model
current_gradient_model.compile(
    optimizer=tf.optimizers.Adam(learning_rate=0.1),
    loss='mean_absolute_error')

#And then we fit the model to the expected output label

history = current_gradient_model.fit(
    train_features['Current_Gradients'], train_labels,
    epochs=100,
    # suppress logging
    verbose=0,
    # Calculate validation results on 20% of the training data
    validation_split = 0.2)

#We can visualize the models training progress using the stats stored in history
hist = pd.DataFrame(history.history)
hist['epoch'] = history.epoch
hist.tail()

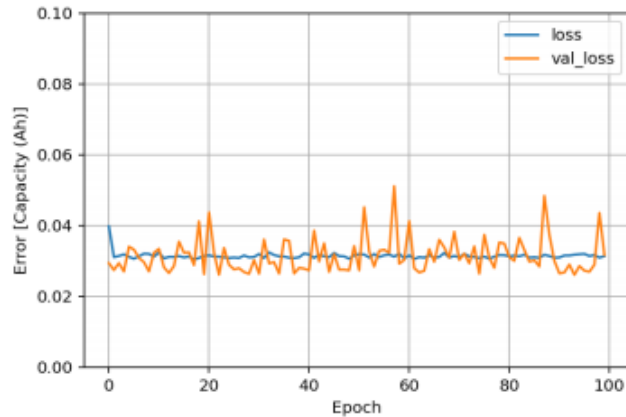
```

Out[79]:

	loss	val_loss	epoch
95	0.03	0.03	95
96	0.03	0.03	96
97	0.03	0.03	97
98	0.03	0.04	98
99	0.03	0.03	99

In [82]: *#Visualize the models performance*

```
def plot_loss(history):  
    plt.plot(history.history['loss'], label='loss')  
    plt.plot(history.history['val_loss'], label='val_loss')  
    plt.ylim([0, 0.1])  
    plt.xlabel('Epoch')  
    plt.ylabel('Error [Capacity (Ah)]')  
    plt.legend()  
    plt.grid(True)  
  
plot_loss(history)
```



In [83]: *#Store the results of the model for Later*

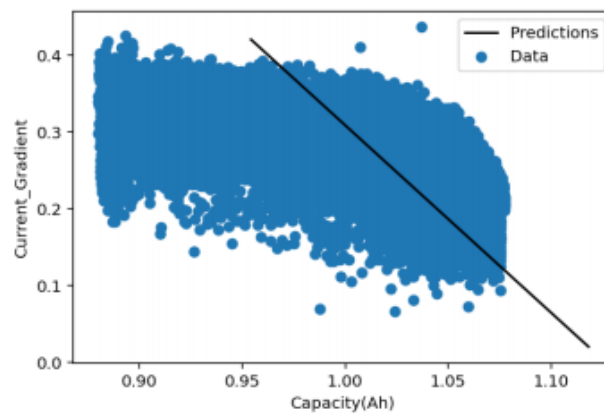
```
test_results = {}  
  
test_results['current_gradient_model'] = current_gradient_model.evaluate(  
    test_features['Current_Gradients'],  
    test_labels, verbose=0)
```

```
In [109]: #Test the Linear regression results

x = np.arange(0.02, 0.44, 0.04)
y = current_gradient_model.predict(x)

def plot_capacity(x,y):
    plt.scatter( train_labels, train_features['Current_Gradients'], label='Data')
    plt.plot(y,x, color='k', label='Predictions')
    plt.xlabel('Capacity(Ah)')
    plt.ylabel('Current_Gradient')
    plt.legend()

plot_capacity(x,y)
```



```
In [94]: #Let us develop a DNN model for the same dataset

#Here we use both input features of Current Gradients and CV Time

def build_and_compile_model(norm):
    model = keras.Sequential([
        norm,
        layers.Dense(64, activation='relu'),
        layers.Dense(64, activation='relu'),
        layers.Dense(1)
    ])

    model.compile(loss='mean_absolute_error',
                  optimizer=tf.keras.optimizers.Adam(0.001))
    return model

dnn_currentGradient_model = build_and_compile_model(current_gradient_normalize)
dnn_currentGradient_model.summary()
```

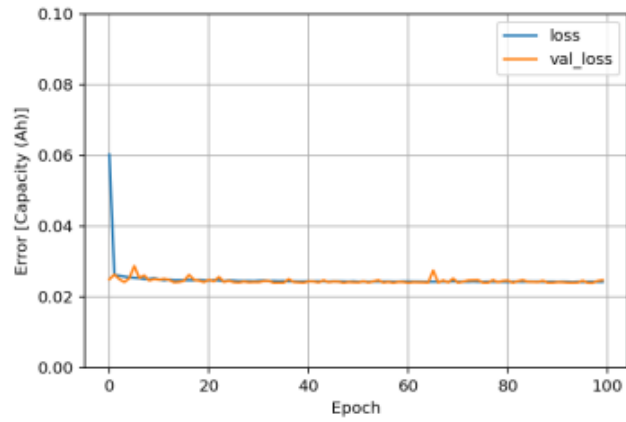
Model: "sequential_3"

Layer (type)	Output Shape	Param #
normalization_2 (Normalizati	(None, 1)	3
dense_7 (Dense)	(None, 64)	128
dense_8 (Dense)	(None, 64)	4160
dense_9 (Dense)	(None, 1)	65
Total params: 4,356		
Trainable params: 4,353		
Non-trainable params: 3		

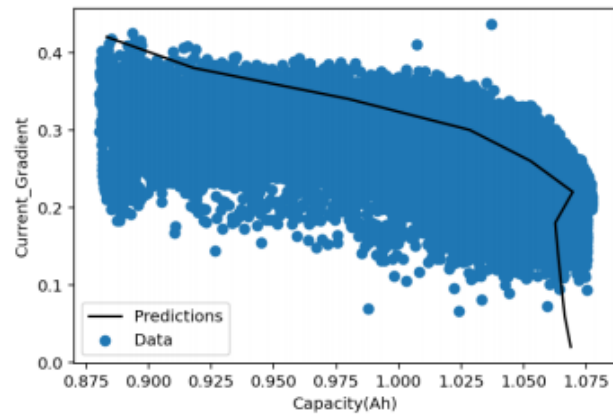
```
In [96]: #Fit data to DNN Model

history = dnn_currentGradient_model.fit(
    train_features['Current_Gradients'], train_labels,
    validation_split=0.2,
    verbose=0, epochs=100)
```

```
In [97]: #Plot Loss of the model
plot_loss(history)
```



```
In [110]: x = np.arange(0.02, 0.44, 0.04)
y = dnn_currentGradient_model.predict(x)
plot_capacity(x,y)
```



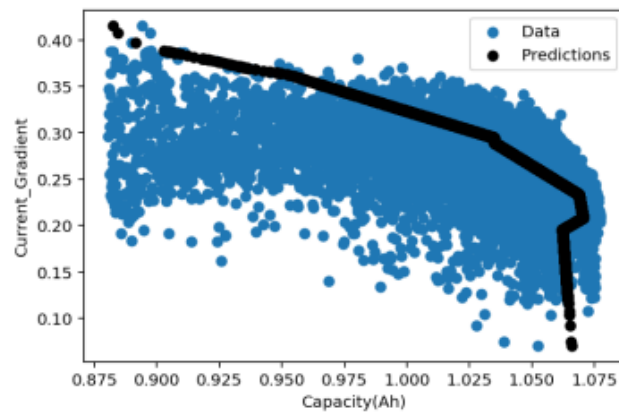
```

In [118]: x = test_features['Current_Gradients'][:10000]
          y = dnn_currentGradient_model.predict(x)

def plot_test_capacity(x,y):
    plt.scatter( test_labels[:10000], test_features['Current_Gradients'][:10000],label='Data')
    plt.scatter( y,x, color='k', label='Predictions')
    plt.xlabel('Capacity(Ah)')
    plt.ylabel('Current_Gradient')
    plt.legend()

plot_test_capacity(x,y)

```



BIBLIOGRAPHY

- [1] E. P. A. "Sources of Greenhouse Gas Emissions."
<https://www.epa.gov/ghgemissions/sources-greenhouse-gas-emissions>
- [2] Y. Miao, P. Hynan, A. von Jouanne, and A. Yokochi, "Current Li-Ion Battery Technologies in Electric Vehicles and Opportunities for Advancements," *Energies*, vol. 12, no. 6, 2019, doi: 10.3390/en12061074.
- [3] F. G. Dias, M. Mohanpurkar, A. Medam, D. Scoffield, and R. Hovsopian, "Impact of controlled and uncontrolled charging of electrical vehicles on a residential distribution grid," in *2018 IEEE International Conference on Probabilistic Methods Applied to Power Systems (PMAPS)*, 24-28 June 2018 2018, pp. 1-5, doi: 10.1109/PMAPS.2018.8440511.
- [4] H. S. Hayajneh and X. Zhang, "Logistics Design for Mobile Battery Energy Storage Systems," *Energies*, vol. 13, no. 5, 2020, doi: 10.3390/en13051157.
- [5] B. University, "Types of Lithium-ion batteries,"
- [6] J. Vetter *et al.*, "Ageing mechanisms in lithium-ion batteries," *Journal of Power Sources*, vol. 147, no. 1, pp. 269-281, 2005/09/09/ 2005, doi: <https://doi.org/10.1016/j.jpowsour.2005.01.006>.
- [7] X. Lei, X. Zhao, G. Wang, and W. Liu, "A Novel Temperature–Hysteresis Model for Power Battery of Electric Vehicles with an Adaptive Joint Estimator on State of Charge and Power," *Energies*, vol. 12, no. 19, 2019, doi: 10.3390/en12193621.
- [8] T. Huria, M. Ceraolo, J. Gazzarri, and R. Jackey, "High fidelity electrical model with thermal dependence for characterization and simulation of high power lithium battery cells," *Electric Vehicle Conference (IEVC), 2012 IEEE International*, 03/01 2012, doi: 10.1109/IEVC.2012.6183271.
- [9] C. Lin, A. Tang, and W. Wang, "A Review of SOH Estimation Methods in Lithium-ion Batteries for Electric Vehicle Applications," *Energy Procedia*, vol. 75, pp. 1920-1925, 2015/08/01/ 2015, doi: <https://doi.org/10.1016/j.egypro.2015.07.199>.

- [10] B. L. H. Saw, A. A. O. Tay, and L. Zhang, *Thermal Management of Lithium-ion Battery Pack with Liquid Cooling*. 2015.
- [11] B. Singh, B. N. Singh, A. Chandra, K. Al-Haddad, A. Pandey, and D. P. Kothari, "A review of three-phase improved power quality AC-DC converters," *IEEE Transactions on Industrial Electronics*, vol. 51, no. 3, pp. 641-660, 2004, doi: 10.1109/TIE.2004.825341.
- [12] G. Khalil, "Challenges of hybrid electric vehicles for military applications," in *2009 IEEE Vehicle Power and Propulsion Conference*, 7-10 Sept. 2009 2009, pp. 1-3, doi: 10.1109/VPPC.2009.5289878.
- [13] S. Rahman, "Mitigation of distribution level impact of electric vehicles," ed. *Proc. Rec. IEEE Power Energy Syst. Innovative Smart Grid Tech. Conf.*, 2012.
- [14] G. T. Heydt, "The Impact of Electric Vehicle Deployment on Load Management Strategies," *IEEE Transactions on Power Apparatus and Systems*, vol. PAS-102, no. 5, pp. 1253-1259, 1983, doi: 10.1109/TPAS.1983.318071.
- [15] X. Zhou, S. Lukic, S. Bhattacharya, and A. Huang, "Design and control of grid-connected converter in bi-directional battery charger for Plug-in hybrid electric vehicle application," in *2009 IEEE Vehicle Power and Propulsion Conference*, 7-10 Sept. 2009 2009, pp. 1716-1721, doi: 10.1109/VPPC.2009.5289691.
- [16] M. Yilmaz and P. T. Krein, "Review of the Impact of Vehicle-to-Grid Technologies on Distribution Systems and Utility Interfaces," *IEEE Transactions on Power Electronics*, vol. 28, no. 12, pp. 5673-5689, 2013, doi: 10.1109/TPEL.2012.2227500.
- [17] W. Kempton and J. Tomić, "Vehicle-to-grid power implementation: From stabilizing the grid to supporting large-scale renewable energy," *Journal of Power Sources*, vol. 144, no. 1, pp. 280-294, 2005/06/01/ 2005, doi: <https://doi.org/10.1016/j.jpowsour.2004.12.022>.
- [18] J. Zhang *et al.*, "Multi-objective planning of charging stations considering vehicle arrival hot map," in *2017 IEEE Conference on Energy Internet and Energy System Integration (EI2)*, 26-28 Nov. 2017 2017, pp. 1-6, doi: 10.1109/EI2.2017.8245374.

- [19] K. Schneider, C. Gerkenmeyer, M. Kintner-Meyer, and R. Fletcher, "Impact assessment of plug-in hybrid vehicles on pacific northwest distribution systems," in *2008 IEEE Power and Energy Society General Meeting - Conversion and Delivery of Electrical Energy in the 21st Century*, 20-24 July 2008 2008, pp. 1-6, doi: 10.1109/PES.2008.4596392.
- [20] A. Y. Saber and G. K. Venayagamoorthy, "Plug-in Vehicles and Renewable Energy Sources for Cost and Emission Reductions," *IEEE Transactions on Industrial Electronics*, vol. 58, no. 4, pp. 1229-1238, 2011, doi: 10.1109/TIE.2010.2047828.
- [21] A. Schuller, J. Ilg, and C. v. Dinther, "Benchmarking electric vehicle charging control strategies," in *2012 IEEE PES Innovative Smart Grid Technologies (ISGT)*, 16-20 Jan. 2012 2012, pp. 1-8, doi: 10.1109/ISGT.2012.6175732.
- [22] A. T. Al-Awami and E. Sortomme, "Coordinating Vehicle-to-Grid Services With Energy Trading," *IEEE Transactions on Smart Grid*, vol. 3, no. 1, pp. 453-462, 2012, doi: 10.1109/TSG.2011.2167992.
- [23] R. Doctors, "A systems approach to battery powered vehicles," in *Proceedings of the Tenth Annual Battery Conference on Applications and Advances*, 10-13 Jan. 1995 1995, pp. 117-122, doi: 10.1109/BCAA.1995.398497.
- [24] O. Worley and D. Klabjan, "Optimization of battery charging and purchasing at electric vehicle battery swap stations," in *2011 IEEE Vehicle Power and Propulsion Conference*, 6-9 Sept. 2011 2011, pp. 1-4, doi: 10.1109/VPPC.2011.6043182.
- [25] C. D. Waldron and P. Kobylarek, ""The reality of electric vehicles and the grid," vol. 89, 1, pp. 54-56, Jan./Feb. 2011.
- [26] A. Y. Saber and G. K. Venayagamoorthy, "Intelligent unit commitment with vehicle-to-grid —A cost-emission optimization," *Journal of Power Sources*, vol. 195, no. 3, pp. 898-911, 2010/02/01/ 2010, doi: <https://doi.org/10.1016/j.jpowsour.2009.08.035>.
- [27] T. Markel, M. Kuss, and P. Denholm, "Communication and control of electric drive vehicles supporting renewables," in *2009 IEEE Vehicle Power and Propulsion Conference*, 7-10 Sept. 2009 2009, pp. 27-34, doi: 10.1109/VPPC.2009.5289874.

- [28] D. Witzke, M. Wieland, and F. Alhaider, "Development of an Operational Strategy for Hybrid Power Plants Consisting of Battery Energy Storage System and Wind Farm to Enable Stacked Applications," in *NEIS 2020; Conference on Sustainable Energy Supply and Energy Storage Systems*, 14-15 Sept. 2020 2020, pp. 1-6.
- [29] C. A. Hill, M. C. Such, D. Chen, J. Gonzalez, and W. M. Grady, "Battery Energy Storage for Enabling Integration of Distributed Solar Power Generation," *IEEE Transactions on Smart Grid*, vol. 3, no. 2, pp. 850-857, 2012, doi: 10.1109/TSG.2012.2190113.
- [30] R. Ganter. and C. Berrisford. "Smart Mobility." UBS Chief Investment Office Americas, Wealth Management. <https://www.ubs.com/content/dam/WealthManagementAmericas/documents/smart-mobility.pdf> (accessed).
- [31] B. Nykvist and M. Nilsson, "Rapidly falling costs of battery packs for electric vehicles," *Nature Climate Change*, vol. 5, no. 4, pp. 329-332, 2015/04/01 2015, doi: 10.1038/nclimate2564.
- [32] H. Lee and A. Clark, "Charging the Future: Challenges and Opportunities for Electric Vehicle Adoption," ed: Havard Kennedy School, Faculty Research Working Paper Series, , Sep 2018.
- [33] F. Adegbohun, A. von Jouanne, and K. Y. Lee, "Autonomous Battery Swapping System and Methodologies of Electric Vehicles," *Energies*, vol. 12, no. 4, 2019, doi: 10.3390/en12040667.
- [34] R. Moghe, F. Kreikebaum, J. E. Hernandez, R. P. Kandula, and D. Divan, "Mitigating distribution transformer lifetime degradation caused by grid-enabled vehicle (GEV) charging," in *2011 IEEE Energy Conversion Congress and Exposition*, 17-22 Sept. 2011 2011, pp. 835-842, doi: 10.1109/ECCE.2011.6063857.
- [35] P. Venugopal and V. T, "State-of-Health Estimation of Li-ion Batteries in Electric Vehicle Using IndRNN under Variable Load Condition," *Energies*, vol. 12, no. 22, 2019, doi: 10.3390/en12224338.

- [36] T. Ikeya *et al.*, "Multi-step constant-current charging method for an electric vehicle nickel/metal hydride battery with high-energy efficiency and long cycle life," *Journal of Power Sources*, vol. 105, no. 1, pp. 6-12, 2002/03/05/ 2002, doi: [https://doi.org/10.1016/S0378-7753\(01\)00907-7](https://doi.org/10.1016/S0378-7753(01)00907-7).
- [37] L. Dung, C. Chen, and H. Yuan, "A robust, intelligent CC-CV fast charger for aging lithium batteries," in *2016 IEEE 25th International Symposium on Industrial Electronics (ISIE)*, 8-10 June 2016 2016, pp. 268-273, doi: 10.1109/ISIE.2016.7744901.
- [38] X. Wang, S. Li, L. Wang, Y. Sun, and Z. Wang, "Degradation and Dependence Analysis of a Lithium-Ion Battery Pack in the Unbalanced State," *Energies*, vol. 13, no. 22, 2020, doi: 10.3390/en13225934.
- [39] B. Balagopal and M. Chow, "The state of the art approaches to estimate the state of health (SOH) and state of function (SOF) of lithium Ion batteries," in *2015 IEEE 13th International Conference on Industrial Informatics (INDIN)*, 22-24 July 2015 2015, pp. 1302-1307, doi: 10.1109/INDIN.2015.7281923.
- [40] M. Hartmann and J. Kelly, "Thermal Runaway Prevention of Li-ion Batteries by Novel Thermal Management System," in *2018 IEEE Transportation Electrification Conference and Expo (ITEC)*, 13-15 June 2018 2018, pp. 477-481, doi: 10.1109/ITEC.2018.8450177.
- [41] M. S. A. Chowdhury, K. A. A. Mamun, and A. M. Rahman, "Modelling and simulation of power system of battery, solar and fuel cell powered Hybrid Electric vehicle," in *2016 3rd International Conference on Electrical Engineering and Information Communication Technology (ICEEICT)*, 22-24 Sept. 2016 2016, pp. 1-6, doi: 10.1109/CEEICT.2016.7873126.
- [42] M. Yaich, M. R. Hachicha, and M. Ghariani, "Modeling and simulation of electric and hybrid vehicles for recreational vehicle," in *2015 16th International Conference on Sciences and Techniques of Automatic Control and Computer Engineering (STA)*, 21-23 Dec. 2015 2015, pp. 181-187, doi: 10.1109/STA.2015.7505098.
- [43] Z. Jian, S. Xiangming, and L. Dong, "Modeling and simulation for electric vehicle powertrain controls," in *2014 IEEE Conference and Expo Transportation Electrification Asia-Pacific (ITEC Asia-Pacific)*, 31 Aug.-3 Sept. 2014 2014, pp. 1-4, doi: 10.1109/ITEC-AP.2014.6940824.

- [44] O. Tremblay, L. Dessaint, and A. Dekkiche, "A Generic Battery Model for the Dynamic Simulation of Hybrid Electric Vehicles," in *2007 IEEE Vehicle Power and Propulsion Conference*, 9-12 Sept. 2007 2007, pp. 284-289, doi: 10.1109/VPPC.2007.4544139.
- [45] J. Liu *et al.*, "Design of the Chevrolet Bolt EV Propulsion System," *SAE Int. J. Alt. Power.*, vol. 5, no. 1, pp. 79-86, 2016, doi: 10.4271/2016-01-1153.
- [46] G. Sieklucki, "An Investigation into the Induction Motor of Tesla Model S Vehicle," in *2018 International Symposium on Electrical Machines (SME)*, 10-13 June 2018 2018, pp. 1-6, doi: 10.1109/ISEM.2018.8442648.
- [47] J. d. Santiago *et al.*, "Electrical Motor Drivelines in Commercial All-Electric Vehicles: A Review," *IEEE Transactions on Vehicular Technology*, vol. 61, no. 2, pp. 475-484, 2012, doi: 10.1109/TVT.2011.2177873.
- [48] Y. Liu, Y. Chen, Z. Li, K. Zhao, and Z. Lin, "Multi-Objective Optimal Gearshift Control for Multispeed Transmission Electric Vehicles," *IEEE Access*, vol. 8, pp. 129785-129798, 2020, doi: 10.1109/ACCESS.2020.3009481.
- [49] A. v. Jouanne *et al.*, "Electric Vehicle (EV) Chassis Dynamometer Testing," in *2020 IEEE Energy Conversion Congress and Exposition (ECCE)*, 11-15 Oct. 2020 2020, pp. 897-904, doi: 10.1109/ECCE44975.2020.9236288.
- [50] R. Collin, Y. Miao, A. Yokochi, P. Enjeti, and A. von Jouanne, "Advanced Electric Vehicle Fast-Charging Technologies," *Energies*, vol. 12, no. 10, 2019, doi: 10.3390/en12101839.
- [51] D. Tracy. "An Extremely Detailed look at the Porsche Taycan's Engineering Designed to take on Tesla." <https://jalopnik.com/an-extremely-detailed-look-at-the-porsche-taycans-engin-1837802533> (accessed.)
- [52] "Tesla Model S AWD " <https://www.tesla.com/models/design#overview> (accessed.)
- [53] I. Husain, *Electric and Hybrid Vehicles : Design Fundamentals*, Second ed. Boca Roca: CRC Press LLC, 2010.
- [54] MATLAB and Simulink Racing Lounge. "MathWorks Student Competitions Team (2021) : Vehicle Modeling." (accessed.)

- [55] A. Palihawadana, D. Ranathunga, and L. Wickramaratne, "Design of the Propulsion System For an Electric Formula Car," 2017.
- [56] *SAE J1634. In Battery Electric Vehicle Energy Consumption and Range Test Procedure*, SAE, July, 2017.
- [57] UQM, "PP 220 UQM Manual ", ed.
- [58] T. Motors, "Thunderstruck EV VCU Manual ", ed.
- [59] K. A. Severson *et al.*, "Data-driven prediction of battery cycle life before capacity degradation," *Nature Energy*, vol. 4, no. 5, pp. 383-391, 2019/05/01 2019, doi: 10.1038/s41560-019-0356-8.
- [60] M. Kane. "Check Out This Official Tesla Model S/X Battery Capacity Degradation Chart." <https://insideevs.com/news/429818/tesla-model-s-x-battery-capacity-degradation/> (accessed).
- [61] BorgWarner, "BorgWarner HVH250-115 Electric Motor," ed.

